

# Connection between planetary He I $\lambda 10830$ Å absorption and extreme-ultraviolet emission of planet-host stars

J. Sanz-Forcada<sup>1</sup>, M. López-Puertas<sup>2</sup>, M. Lampón<sup>2</sup>, S. Czesla<sup>3</sup>, L. Nortmann<sup>4</sup>, J. A. Caballero<sup>1</sup>,  
M. R. Zapatero Osorio<sup>1</sup>, P. J. Amado<sup>2</sup>, F. Murgas<sup>5,6</sup>, J. Orell-Miquel<sup>5,6</sup>, E. Pallé<sup>5,6</sup>, A. Quirrenbach<sup>7</sup>, A. Reiners<sup>4</sup>,  
I. Ribas<sup>8,9</sup>, A. Sánchez-López<sup>2</sup>, and E. Solano<sup>1</sup>

<sup>1</sup> Centro de Astrobiología, CSIC-INTA, Camino bajo del Castillo s/n, E-28692 Villanueva de la Cañada, Madrid, Spain  
e-mail: jsanz@cab.inta-csic.es

<sup>2</sup> Instituto de Astrofísica de Andalucía (IAA-CSIC), Glorieta de la Astronomía s/n, E-18008 Granada, Spain

<sup>3</sup> Thüringer Landessternwarte Tautenburg, Sternwarte 5, D-07778 Tautenburg, Germany

<sup>4</sup> Institut für Astrophysik und Geophysik, George-August-Universität, Friedrich-Hund-Platz 1, D-37077 Göttingen, Germany

<sup>5</sup> Instituto de Astrofísica de Canarias (IAC), E-38205 La Laguna, Tenerife, Spain

<sup>6</sup> Departamento de Astrofísica, Universidad de La Laguna (ULL), E-38206 La Laguna, Tenerife, Spain

<sup>7</sup> Landessternwarte, Zentrum für Astronomie der Universität Heidelberg, Königstuhl 12, D-69117 Heidelberg, Germany

<sup>8</sup> Institut de Ciències de l'Espai (ICE, CSIC), Campus UAB, Can Magrans s/n, E-08193 Bellaterra, Barcelona, Spain

<sup>9</sup> Institut d'Estudis Espacials de Catalunya (IEEC), E-08860 Castelldefels, Barcelona, Spain

Received 26 July 2024 / Accepted 12 December 2024

## ABSTRACT

**Context.** The detection of the He I  $\lambda 10830$  Å triplet in exoplanet atmospheres has opened a new window for probing planetary properties, including atmospheric escape. Unlike Lyman  $\alpha$ , the triplet is significantly less affected by interstellar medium (ISM) absorption. Sufficient X-ray and extreme ultraviolet (XUV) stellar irradiation may trigger the formation of the He I triplet via photoionization and posterior recombination processes in the planet atmospheres. Only a weak trend between stellar XUV emission and the planetary He I strength has been observed so far.

**Aims.** We aim to confirm this mechanism for producing near-infrared He I absorption in exoplanetary atmospheres by examining a substantial sample of planetary systems.

**Methods.** We obtained homogeneous measurements of the planetary He I line equivalent width and consistently computed the stellar XUV ionizing irradiation. Our first step was to derive new coronal models for the planet-host stars. We used updated data from the X-exoplanets database, archival X-ray spectra of M-type stars (including AU Mic and Proxima Centauri), and new *XMM-Newton* X-ray data recently obtained for the CARMENES project. These data were complemented at longer wavelengths with publicly available HST, FUSE, and EUVE spectra. A total of 75 stars are carefully analyzed to obtain a new calibration between X-ray and extreme ultraviolet (EUV) emission.

**Results.** Two distinct relationships between stellar X-ray emission (5–100 Å) and EUV<sub>H</sub> (100–920 Å) or EUV<sub>He</sub> (100–504 Å) radiation are obtained to scale the emission from late-type (F to M) stellar coronae. A total of 48 systems with reported planetary He I  $\lambda 10830$  Å studies, including 21 positive detections and 27 upper limits, exhibit a robust relationship between the strength of the planetary He I feature and the ionizing XUV<sub>He</sub> received by the planet, corrected by stellar and planetary radii, as well as the planet's gravitational potential. Some outliers could be explained by a different atmospheric composition or the lack of planetary gaseous atmospheres. This relation may serve as a guide to predict the detectability of the He I  $\lambda 10830$  Å absorption in exoplanet atmospheres.

**Key words.** planetary systems – stars: coronae – X-rays: stars – planets and satellites: atmospheres

## 1. Introduction

The detection of atmospheric features in transiting exoplanets has become the best approach to understanding the composition and evolution of their atmospheres. The earliest detection reports were made for Na I (Charbonneau et al. 2002) and H I Lyman  $\alpha$  (Vidal-Madjar et al. 2003), both in HD 209458 b. A number of atomic and molecular species have been detected since then (e.g., Madhusudhan 2019, and references therein). It is remarkable that helium, the second most abundant element in stars and in Solar System planets such as Jupiter or Saturn, was not detected until 2018. Theoretical works (Seager & Sasselov 2000) have predicted the possibility to detect the He I infrared triplet at 10830 Å in the atmosphere of transiting exoplanets. An attempt to detect this feature was made by Sasselov & Sanz-Forcada

in 2000 and 2001, using the NASA Infrared Telescope Facility (IRTF), but no feature was detected due to bad weather conditions in both campaigns combined with insufficient instrument sensitivity. Moutou et al. (2003) used VLT/ISAAC to search for the same feature, but no detection was made either. During the following years the search for atmospheric features focused on other species. The idea of observing exoplanet atmospheres using the He I 10830 line was resurrected by Oklopčić & Hirata (2018). The line was soon detected independently by three different groups (Spake et al. 2018; Nortmann et al. 2018; Allart et al. 2018), and two more detections were reported in the same year (Mansfield et al. 2018; Salz et al. 2018). Nortmann et al. (2018) also identified, as proposed by Seager & Sasselov (2000), that in exoplanet atmospheres the line formation is directly re-

lated to the incoming stellar irradiation in the XUV band at  $\lambda \sim 5 - 504 \text{ \AA}$ , with  $504 \text{ \AA}$  being the wavelength corresponding to the first ionization energy of He.

The neutral helium atom possesses two types of configurations, namely, orthohelium, and parahelium, corresponding to different sets of energy levels. In orthohelium, the most conspicuous line is actually a triplet, at  $10830 \text{ \AA}$ <sup>1</sup>. This triplet is associated with a less intense optical triplet at  $5876 \text{ \AA}$ . The formation of these triplets has long been studied in both massive or low-mass stars. Two mechanisms have been proposed to explain the formation of the triplets: (i) collisional excitation from the singlet (parahelium) levels may populate the ground level of the triplet (orthohelium), allowing for the formation of the triplet lines at  $10830$  and  $5876 \text{ \AA}$ . A high temperature ( $\geq 20,000 \text{ K}$ ) is required for this mechanism to operate. Alternatively, in a colder environment, (ii) the He I atom can be radiatively ionized with EUV photons ( $\lambda < 504 \text{ \AA}$ ) that would soon recombine into neutral atoms, some of them populating the triplet lower levels in a de-excitation cascade (photoionization-recombination mechanism). Examples of the first mechanism are present in stellar winds observed in the G2 I supergiant  $\alpha \text{ Aqr}$  (Dupree et al. 1992). The second mechanism is thought to be responsible for the formation of the line in stellar chromospheres of late-type stars (e.g., Zarro & Zirin 1986), which receive EUV photons from their coronae. In this case, a balance of the two mechanisms could occur in dwarfs because of the high temperatures and density reached in their chromospheres (Andretta & Giampapa 1995; Sanz-Forcada & Dupree 2008).

In the case of planet atmospheres, the photoionization-recombination mechanism is likely responsible for producing this line, given their cold environment. Hence, we would expect to see a relation between the ionizing XUV irradiation of the planets and the observed He I triplet in their atmospheres. A small sample of five objects reported by Nortmann et al. (2018) seems to follow this trend, but a recent compilation of all published data on He I  $10830$  in exoplanets (Fossati et al. 2022) could not find such relation. Fossati et al. (2022) used the (H-ionizing) radiation in the range  $5-920 \text{ \AA}$  ( $XUV_H$ ) as a proxy of the He-ionizing radiation. Similar non-conclusive results were found by Kirk et al. (2022), Fossati et al. (2023), and Allart et al. (2023). A further study was carried out by Zhang et al. (2023a), using a relationship between planetary mass-loss rates estimated from observations and the theoretical energy-limited mass-loss rates. These authors were able to find a rather good correlation between the XUV flux in the same range and the observed He I triplet absorption.

In this paper, we attempt to probe the correlation between ionizing stellar  $XUV_{He}$  (in the range  $5-504 \text{ \AA}$ ) irradiation and the He I triplet in exoplanets. Since high-energy photons are easily absorbed by the interstellar medium (ISM), no direct observations of spectra in the range  $400-504 \text{ \AA}$  are available for stars other than the Sun and most stars do not have reliable data in the  $100-400 \text{ \AA}$  range either. A coronal model is needed to estimate the stellar spectral energy distribution (SED) in the range not covered by the actual data. It is thus necessary to calculate accurate coronal models of the exoplanet host stars and to calibrate a relation allowing us to easily calculate the broadband  $XUV_{He}$  stellar flux. Details of the X-ray and UV observations used to prepare these models, as well as on the method employed, are described in Sects. 2 and 3. The results obtained for the objects

in the sample are given in Sect. 4, together with a new scaling law to easily calculate the broadband EUV emission in the H- and He-ionizing ranges, provided that the X-ray flux is available. The different parametrizations to relate the  $XUV_{He}$  flux and the He I line are explored, too. In Sect. 5, we discuss the results as compared with actual He I detections observed in exoplanet atmospheres, along with the implications that they have for research on the planet atmospheres. The conclusions are given in Sect. 6. We then provide appendices to further discuss the comparison with other XUV scaling laws (Appendix A) and the relation between the He I  $10830$  equivalent width and the  $XUV_{He}$  flux (Appendix B). Tables with the observing logs and main results are found in Appendix C. In Appendix D we include the tables with X-rays and UV line fluxes, along with the figures and tables providing results of the coronal models.

## 2. Observations

We were granted *XMM-Newton* Director Discretionary Time (DDT, prop. IDs #101704 and #106917, PI Sanz-Forcada), and Guest Observer time (prop. ID #092312, PI Sanz-Forcada) to observe a sample of planet-hosting stars suitable for a search of the He I  $10830$  triplet with the Calar Alto high-Resolution search for M dwarfs with Exoearths with Near-infrared and optical Echelle Spectrographs (CARMENES Quirrenbach et al. 2014). *XMM-Newton* simultaneously operates two high-spectral resolution detectors (RGS,  $\lambda \sim 6-38 \text{ \AA}$ ,  $\lambda/\Delta\lambda \sim 100-500$ , den Herder et al. 2001) and three European Photon Imaging Camera (EPIC-PN and EPIC-MOS) detectors (sensitivity range  $0.1-15 \text{ keV}$  and  $0.2-10 \text{ keV}$ , respectively,  $E/\Delta E \sim 20-50$ , Turner et al. 2001; Strüder et al. 2001). *XMM-Newton* also includes an optical monitor (OM). We did not use the OM data in this work because the light in its UV filters is severely contaminated with stellar photospheric emission (Orell-Miquel et al. 2023). The data were reduced using the *XMM-Newton* Science Analysis Software (SAS) v20.0, and analyzed following standard procedures within the Interactive Spectral Interpretation System (ISIS, Houck & Denicola 2000) package. Most targets did not have enough statistics to use RGS, so EPIC data were used to obtain a discrete (one to three temperatures) fit to the spectra.

Some objects were also observed with the *Chandra* X-ray observatory (Weisskopf et al. 2002). The High Energy Transmission Grating Spectrograph (HETGS) contains two gratings, HEG (High Energy Grating,  $\lambda \sim 1.5-15 \text{ \AA}$ ,  $\lambda/\Delta\lambda \sim 120-1200$ ), and MEG (Medium Energy Grating  $\lambda \sim 3-30 \text{ \AA}$ ,  $\lambda/\Delta\lambda \sim 60-1200$ ), which operate simultaneously, permitting the further analysis of the data with different spectral resolutions. The Low Energy Transmission Grating Spectrograph (LETGS,  $\lambda \sim 3-175 \text{ \AA}$ ,  $\lambda/\Delta\lambda \sim 60-1000$ ) was used in combination with the High Resolution Camera (HRC-S). The positive and negative orders were summed for the flux measurements. Lines formed in the first dispersion order, but contaminated with contribution from higher dispersion orders, were not employed in the analysis. We also used the Advanced CCD Imaging Spectrometer (ACIS,  $E/\Delta E \sim 20-50$ ) with no grating. Standard reduction tasks present in the CIAO v4.14 package were employed in the reduction of data retrieved from the *Chandra* archive and the extraction of the HEG and MEG spectra. All objects observed in X-rays are listed in Table C.1. We complemented our sample with the objects in the database X-exoplanets<sup>2</sup> (Sanz-Forcada et al. 2011, hereafter SF11), which were reanalyzed for this work as

<sup>1</sup> Lines at  $10829.09$ ,  $10830.25$ ,  $10830.34 \text{ \AA}$  in the air, and  $10832.06$ ,  $10833.22$ ,  $10833.31 \text{ \AA}$  in vacuum.

<sup>2</sup> <http://sdc.cab.inta-csic.es/xexoplanets/jsp/homepage.jsp>

explained in Sect. 3. New *XMM-Newton* observations were included for a few targets of the X-exoplanets original sample (Table C.1): GJ 436, GJ 674, HD 27442, HD 75289, HD 108147, HD 189733, and HD 190360. In targets with more than one *XMM-Newton* observation, we combined all the data to improve the quality of the EPIC spectra used in the fitting. Two objects formerly detected only with ROSAT, or with lower quality *Chandra* spectra, have now *XMM-Newton* observations (GJ 832, and  $\nu$  And). In the case of  $\iota$  Hor we used the coronal model from Sanz-Forcada et al. (2019). A few more targets were added to the sample, either because they are interesting M stars hosting exoplanets (e.g., TRAPPIST-1) because they have been surveyed searching for the He I 10830 triplet or because they can be used to establish a better relation between X-rays and EUV, such as V1298 Tau (Maggio et al. 2023).

Five special cases of M dwarfs, Proxima Cen, AU Mic, AD Leo, Lalande 21185 (GJ 411, HD 95735), and GJ 674, were analyzed in detail using high-resolution X-ray spectra from the *XMM-Newton* or the *Chandra* archives. The use of information from individual spectral lines greatly improves the quality of the coronal models, as shown by Sanz-Forcada et al. (2003b). In these cases, we also included UV spectra (see below). Although the light curves of these targets indicate the possible presence of stellar flares, we preferred to use the combined data of quiescent and flaring states, as we understand that this reflects better the average activity of the star. In the case of Proxima Cen, it was necessary to correct for the radial velocity of the different datasets to co-add the RGS spectra<sup>3</sup>. Besides these five stars, a few targets for which we have only low-resolution *XMM-Newton*/EPIC or *Chandra*/ACIS spectra were analyzed including high-resolution UV spectra from: *Hubble* Space Telescope (HST) Space Telescope Imaging Spectrograph (STIS, Kimble et al. 1998)<sup>4</sup> or Cosmic Origins Spectrograph (COS, Osterman et al. 2011)<sup>5</sup>; Far Ultraviolet Spectroscopic Explorer (*FUSE*, 905–1187 Å,  $\lambda/\Delta\lambda \sim 15,000$ –20,000, Moos et al. 2000); and Extreme Ultraviolet Explorer (*EUVE*, 70–750 Å,  $\lambda/\Delta\lambda \sim 200$ –400, Haisch et al. 1993), as listed in Table C.2. Extracted spectra from HST and *FUSE* were obtained through the Mikulski Archive for Space Telescopes (MAST), while *EUVE* spectra were reduced from the raw data to improve data quality, using the Image Reduction and Analysis Facility (IRAF) EUV standard tools. We also add to this list the X-ray measurements from  $\tau$  Boo (Maggio et al. 2011), now complemented with HST/STIS line fluxes, to extend the coronal model to transition region temperatures (down to  $T \sim 10^4$  K).

The HD 209458 and HD 189733 data were reanalyzed since Sanz-Forcada et al. (2010) to improve the results. In both cases, all the available *XMM-Newton*/EPIC data are combined. In the case of HD 209458 the data analysis was limited to the spectral range 0.3–8 keV to improve the statistics of the spectral fitting, which is now characterized by S/N=3.2. The data of both stars were complemented with HST/COS, as detailed by Lampón et al. (2020, 2021). In the latter case, we also fixed a software bug that led us to overestimate the flux in the EUV range and fur-

ther made a more accurate analysis of the abundance pattern in the entire temperature range. New updated values of broadband EUV fluxes are made available in Table C.3. All these new fluxes supersede measurements formerly reported in CARMENES papers (e.g., Nortmann et al. 2018; Lampón et al. 2021; Lampón et al. 2023) or in Chadney et al. (2015) for the cases of AU Mic and AD Leo.

### 3. Methodology

We made use of coronal models to produce synthetic XUV spectra. To do so, we first calculated the volume emission measure ( $EM$ ) at different coronal temperatures using the X-ray spectra, with  $EM = \int N_e N_H dV$  as defined by Brickhouse & Dupree (1998), where  $N_e$  and  $N_H$  are electron and hydrogen densities, respectively. The ISIS package and the Astrophysics Plasma Emission Database (APED, Smith et al. 2001) were used to fit the low resolution spectra, and to measure spectral line fluxes in high resolution spectra. We reanalyzed all the X-ray spectra included in SF11 to account for the updated stellar distances provided by Gaia DR3 (Gaia Collaboration et al. 2023) and used ATOMDB v3.0.9 in the spectral fitting and further coronal modeling. The flux of the C III multiplet at  $\sim 1176$  Å is measured as one line, and its theoretical flux is evaluated using Raymond (1988) atomic data instead of ATOMDB<sup>6</sup>. The X-ray luminosity was calculated in the 0.12–2.48 keV band ( $\sim 5$ –100 Å), similar to the ROSAT/PSPC standard band, by global fitting of the *XMM-Newton*/EPIC or *Chandra*/ACIS low resolution spectra. The spectral fit was used to calculate a coronal model (Table D.1). The interstellar medium (ISM) hydrogen column density was fixed, using values from ISMTool<sup>7</sup> adapted to the stellar distances. The X-ray to bolometric luminosities ratio gives an indication of the activity level of the star (e.g., Pizzolato et al. 2003; Wright et al. 2011). The bolometric luminosity of the stars was calculated using the calibration by Pecaut & Mamajek (2013) based on  $G$  and  $K_s$  magnitudes<sup>8</sup>, for stars with spectral types earlier than K5. The calibration from Cifuentes et al. (2020) was used for later spectral types, based on the  $G$  and  $J$  magnitudes.

In cases with X-ray high-resolution spectra, individual line fluxes were measured considering the point spread function (PSF) of the instrument, as described by Sanz-Forcada et al. (2003b). The *EUVE* line fluxes were measured using standard IRAF software. The X-ray or EUV line fluxes were used to build the coronal model – namely, the emission measure distribution (EMD) – in the range of  $\log T(K) \sim 5.8$ –7.4, while the UV line fluxes are employed for the transition region range,  $\log T(K) \sim 4$ –5.7, including a few cases in which coronal lines were measured in the UV. The spectral line fluxes measured in the spectra and the observed-to-predicted line fluxes ratio with the resulting EMD are listed in Tables D.2–D.11. The EMDs are listed in Tables D.12 and D.13 and shown in Figs. 1–2 and D.1–D.8. In cases where no UV spectra are available, the coronal model is extended to the transition region assuming larger error bars for this temperature range, following SF11. The technique employed to build the EMD is described in detail by Sanz-Forcada et al. (2003b) and references therein. The basic idea is that an

<sup>3</sup> The *XMM-Newton* pointings were not always properly corrected for the proper motion of the star, resulting in small radial velocity shifts between different datasets.

<sup>4</sup> Sensitivity ranges and resolution of the gratings: E140M 1144–1710 Å,  $\lambda/\Delta\lambda = 45,800$ ; G140L 1150–1730 Å,  $\lambda/\Delta\lambda \sim 960$ –1440; G140M 1140–1740 Å,  $\lambda/\Delta\lambda \sim 11,400$ –17,400

<sup>5</sup> Sensitivity ranges and resolution in the gratings: G130M 900–1450 Å,  $\lambda/\Delta\lambda \sim 12,000$ –17,000; G160M 1360–1775 Å,  $\lambda/\Delta\lambda \sim 13,000$ –20,000

<sup>6</sup> The fluxes of this multiplet, calculated with current version of ATOMDB, do not match those of the observed counterparts

<sup>7</sup> <https://heasarc.gsfc.nasa.gov/cgi-bin/Tools/w3nh/w3nh.pl>

<sup>8</sup> [https://www.pas.rochester.edu/~emamajek/EEM\\_dwarf\\_UBVIJHK\\_colors\\_Teff.txt](https://www.pas.rochester.edu/~emamajek/EEM_dwarf_UBVIJHK_colors_Teff.txt) (accessed in March 2023)

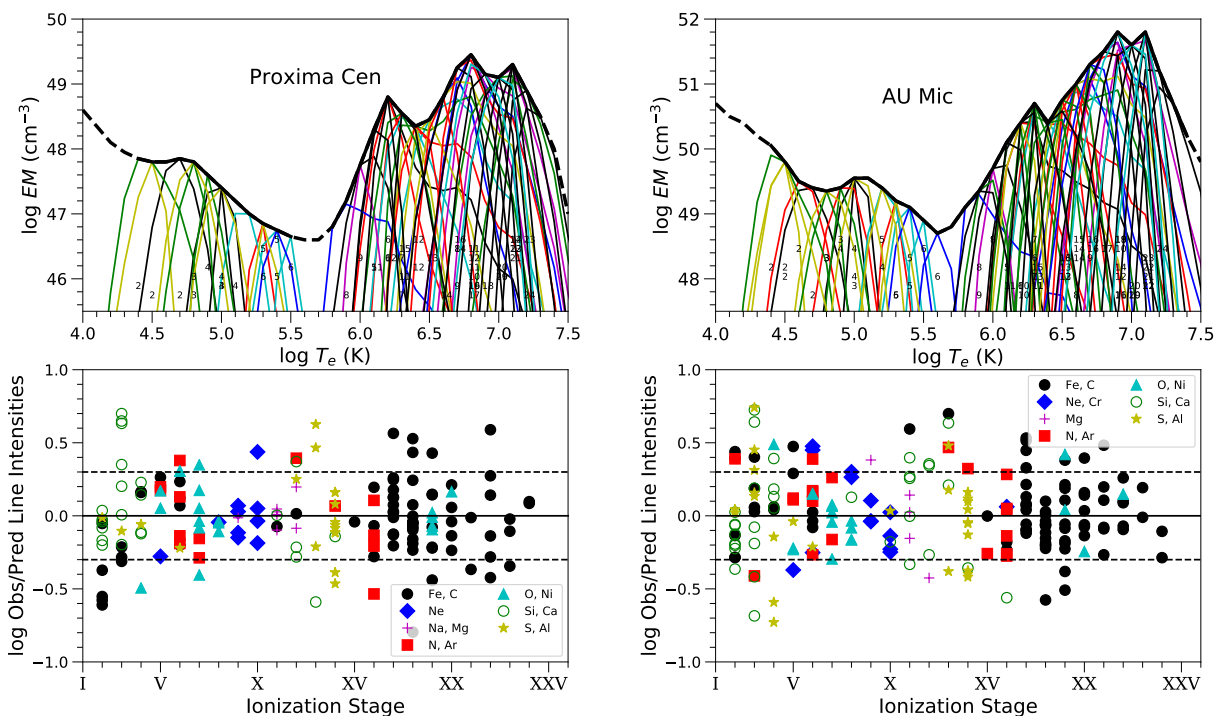


**Fig. 1.** Coronal models of Proxima Cen (*left*) and AU Mic (*right*), combining data from *XMM-Newton*, EUVE, HST/STIS, and FUSE. *Upper panels:* Emission measure distributions (EMDs, thick line). The thin lines represent the contribution function for each ion (the emissivity function multiplied by the EMD at each point). The small numbers indicate the ionization stages of the species. *Lower panels:* Observed-to-predicted line flux ratios for the ion stages in the upper panels. The dashed lines denote a factor of 2.

initial EMD is proposed, with emission measure values at each temperature in a grid of 0.1 dex in the  $\log T$  (K)  $\sim 4.0$ – $7.5$  range, and an initial set of atomic abundances; the EM is convolved with the emissivity function of each observed spectral line. The same operation is performed for any eventual blends that the observed line could have. The predicted line fluxes are then compared to the observed line fluxes and from this comparison, we changed the EMD to better match the observations in an iterative process. The abundances are calculated by doing this process for the lines of only one element (frequently, Fe) and incorporating the lines of other elements trying to partially overlap the temperature range covered by the new element and the former ones. The solution found through this process is then probed with a Monte Carlo method and modified when needed, to calculate the error bars associated with the EM at each temperature, letting the observed fluxes vary by up to  $1\sigma$  in a large number of iterations.

We considered stellar abundances in the corona and transition region in the preparation of the coronal models (Tables D.1, D.14, D.15). In stars with low statistics X-ray spectra, solar photospheric abundances were used by default, except for the stellar photospheric  $[\text{Fe}/\text{H}]$  when available. In the case of abundances obtained from the global fit and the EMD, we used Fe from the global fit, and the other elements from the EMD. The level of the EMD was then based on either C or Si. In the case of HD 189733, there is a Fe III line formed at transition region temperatures that could be used to fix the EMD level with coronal Fe abundance. As we were not confident in the quality of this line, instead we used the coronal abundances of Si, Ne, and O to fix the level of the EMD. Finally, we made use of coronal models to pro-

duce synthetic XUV SED, as detailed by SF11, using the ISIS software. These SEDs in the 1–2800 Å range are made available in the X-exoplanets database, and in Table 1 as described in Sect. 6. Although some individual line fluxes may not be correct given the actual level of accuracy of ATOMDB, we are confident on the overall correctness of these SEDs in the range covered; namely, 5–920 Å. The extension to longer wavelengths should be done with care because ATOMDB has not been sufficiently tested for some of the lines at these wavelengths (e.g., the multiplet of C III at 1176 Å). An additional difficulty may arise for stars with substantial photospheric contribution in the UV, which becomes more important for F and G stars. Emission from plasma with photospheric temperatures is not generally covered by ATOMDB.

## 4. Results

We calculated the broadband stellar luminosity in two different EUV bands, affecting the H ionization ( $\text{EUV}_\text{H}$ ,  $\sim 100$ – $920$  Å) and He ionization ( $\text{EUV}_\text{He}$ ,  $\sim 100$ – $504$  Å), as listed in Table C.3. The summed flux in the XUV bands; namely, X-rays (5–100 Å) as well as  $\text{EUV}_\text{H}$  and  $\text{EUV}_\text{He}$ , were calculated at the planet orbital separation. We also calculated as a reference the mass loss rates, multiplied by the planet density ( $\rho M_p$ ), assuming the energy-limited approach and ignoring effects related to the mass transfer through the Roche lobe:

$$\dot{M}_{\text{XUV}} \sim \frac{3 F_{\text{XUV,H}}}{4 G \rho_p}, \quad (1)$$

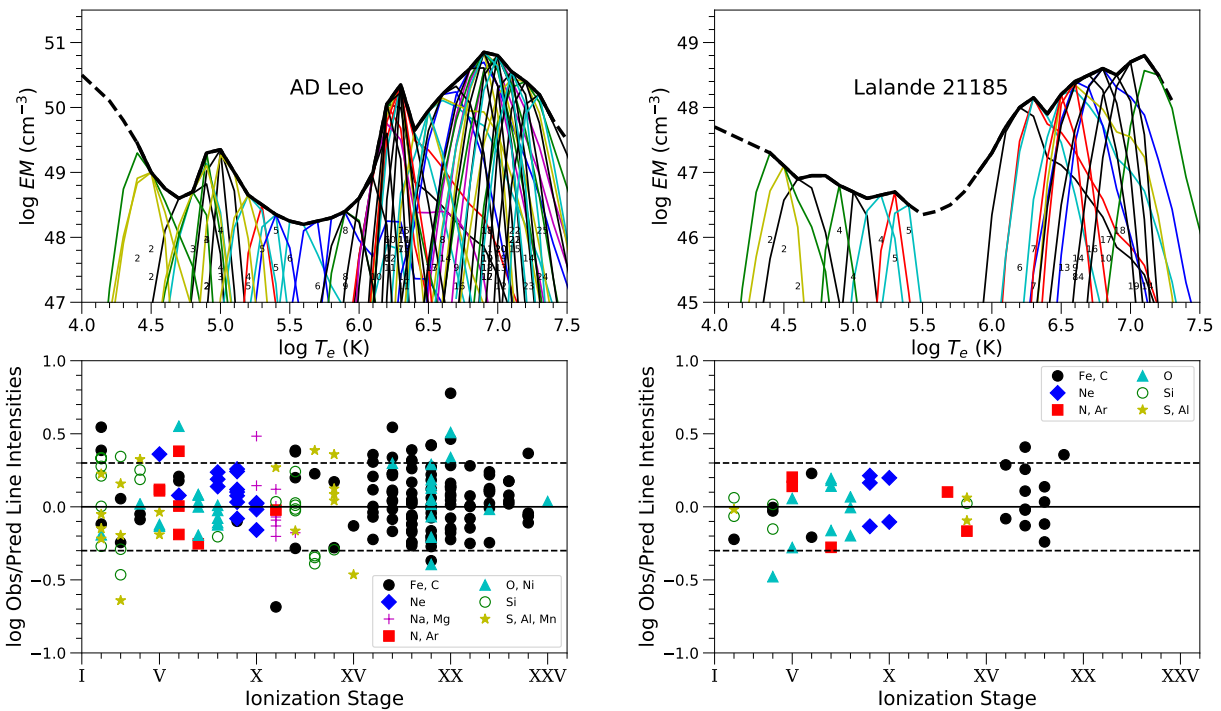


**Fig. 2.** Same as in Fig 1, but for AD Leo (GJ 388, *left*) and Lalande 21185 (*right*), combining data from *Chandra*, EUVE, and HST/STIS (AD Leo), and *XMM-Newton* and HST/STIS (Lalande 21185).

where  $F_{\text{XUV,H}}$  stands for the flux density in the 5–912 Å spectral range,  $G$  is the gravitational constant, and  $\rho_p$  is the planet bulk density, following SF11 and references therein. Table C.3 includes both the stars in the sample of Table C.1 and those available in X-exoplanets as listed by SF11. The latest were updated using new Gaia distances, as well as the new ATOMDB atomic models, as described above.

Details on some individual targets are provided, and the newly calibrated relation between X-rays and EUV flux is described next. We also explored the relation between XUV<sub>He</sub> stellar irradiation onto the planet atmosphere and the observation of the helium infrared triplet (see Sect. 4.4).

#### 4.1. Notes on individual targets

The sample studied in this work pays special attention to M dwarfs, the main focus of the CARMENES survey. We included some of the brightest M stars in X-rays, such as AU Mic, Proxima Cen, and AD Leo, to obtain the best possible coronal models, so that they can be widely employed in planet atmospheric modeling. The brightest objects have plenty of lines to perform an adequate coronal model and calculate the coronal abundances. Some targets are faint in X-rays and their coronal abundance analysis is more complicated, introducing some uncertainty in the balance between the EM at lower (transition region) and higher (coronal) temperatures. Some details to be considered in individual cases are discussed here. In a few stars (WASP-77, GJ 357, GJ 486, HD 149026, and TOI-836), due to the scarcity of bright spectral lines in the COS and STIS ranges, we had to include lines with  $S/N < 3$  to prepare the transition region model. We included the candidate planets AD Leo b and

Barnard’s star b (Tuomi et al. 2018; Ribas et al. 2018) in the sample, although their detection has been questioned afterwards (Carleo et al. 2020; Lubin et al. 2021; Kossakowski et al. 2022).

The Barnard’s star (GJ 699) coronal model, in its high temperature component, is based on the *Chandra*/ACIS spectral fit, rather than on the two coronal lines measured with HST/STIS. Ne and N abundances are uncertain because we could not disentangle them from the EM values within the temperature range of line formation. Also, no relative abundances relative to Fe were calculated. Thus, the actual level of the EM in the transition region could be different. However, the observed coronal Fe lines are in agreement with the  $1-T$  fit to the *Chandra* value, supporting an Fe abundance that should not deviate substantially from solar photospheric values. The problem of uncertain abundances affects also GJ 1214 in N and O, in a similar temperature range.

Some of the X-ray fluxes calculated in this paper differ from former publications (e.g., Loudén et al. 2017; King et al. 2018). Sometimes this is due to the assumption of a different ISM absorption or coronal metallicity. We also avoided the fit of X-ray spectra below 0.3 keV, used in the mentioned work, to avoid instrumental problems such as noise in the low-energy end of EPIC spectra. Our EMD results can also be compared with those by Duvvuri et al. (2021), based on a technique that uses smooth polynomials and solar photospheric abundances to fit a differential emission measure (DEM). Their results are discrepant with ours, as discussed in Appendix A. The use of global fits to get the DEM (or EMD) from high-resolution spectra was argued against the analysis of similar data from EUVE spectra (Bowyer et al. 2000; Favata & Micela 2003; Güdel 2004) because it tended to produce artificial features not supported by observed line fluxes or continuum (e.g., Fig. 13 of Schrijver et al. 1995). This is a

variant of the technique used by Duvvuri et al. (2021). A similar approach was adopted by Loudén et al. (2017). The use of smooth polynomials imposes constraints to the DEM shape, which may not correspond to the actual DEM of the star. Another discrepancy arises when the *XMM-Newton*/OM UV signal is used to scale the SED modeled at UV wavelengths (Zhang et al. 2023b): the UV filters of this instrument are contaminated by stellar photospheric emission from longer wavelengths. Therefore, they cannot be used to set the UV level of emission of late-type main sequence stars (King et al. 2018; Orell-Miquel et al. 2023).

#### 4.2. X-exoplanets 1.1: New calibration

Although it is generally advisable to calculate an individual coronal model for each stellar target, the use of scaling laws is being extensively used in the literature as a first order approach to the problem of planet photoevaporation. We thus consider it important to update the relation of X-exoplanets (SF11) with a better coverage of the different stellar activity regimes.

We calculated a new relation for the  $EUV_H$  and  $EUV_{He}$  against X-ray flux. This relation allows for a fast and reliable calculation of the flux in the EUV spectral ranges, where real data are not available. The first relation of this kind was provided by SF11, who fitted a linear relation between  $\log L_X$  and  $\log L_{EUV,H}$ , with some deviation from the linear fit at higher values. Such deviation is more evident for higher activity stars (Maggio et al. 2023). When applying a similar linear fit to our current sample, this behavior is confirmed, yielding some data dispersion. The resulting linear fits are:

$$\log L_{euVH} = (0.821 \pm 0.041) C_X + (28.16 \pm 0.05) \quad (2)$$

$$\log L_{euVHe} = (0.874 \pm 0.031) C_X + (27.74 \pm 0.04), \quad (3)$$

where  $C_X = \log L_X - 27.44$ , and they are valid in the range  $\log L_X \sim 25.5 - 30.5$ . These fits have a Pearson's correlation factor  $r = 0.920$  and  $0.957$ , and a standard deviation of the residuals (RMS) of  $0.406$  and  $0.309$ , respectively.

The X-ray or EUV luminosities depend on the stellar activity, as well as on the stellar size. To remove the latter dependence, we may use the stellar surface flux, with the associated uncertainties of the stellar radius (Appendix A). Instead, we fit a relation between  $\log L_X/L_{bol}$  and  $\log L_{EUV}/L_{bol}$  (Fig. 3). The use of  $L_{bol}$  removes the effect of the stellar size. Linear fits to these data have  $r = 0.923$  and  $0.960$ , and  $RMS=0.380$  and  $0.281$ , respectively. A substantial bremsstrahlung continuum contribution has an increasing importance with stellar activity, and this continuum is more relevant in X-rays than at EUV wavelengths. A linear fit does not account for the dependence of broadband fluxes on this continuum. Thus a better result is found when applying a quadratic fit:

$$\log \frac{L_{EUV,H}}{L_{bol}} = (-0.062 \pm 0.016) (U_X)^2 + (0.763 \pm 0.037) U_X + (-4.792 \pm 0.051), \quad (4)$$

$$\log \frac{L_{EUV,He}}{L_{bol}} = (-0.022 \pm 0.016) (U_X)^2 + (0.824 \pm 0.029) U_X + (-5.268 \pm 0.039), \quad (5)$$

where  $U_X = \log(L_X/L_{bol}) + 5.60$ . These results are valid for  $\log L_X/L_{bol} \sim -3.1$  to  $-8.8$ , although the application of the

equation for values lower than  $\sim -7.2$  should be done with caution. Although some dispersion still exists, this approach shows a better fit ( $RMS=0.359$  and  $0.277$ , respectively). The remaining data dispersion might be related to deficiencies in the coronal models, such as a lack of high-resolution spectral data or problems in the calculations of stellar abundances in the corona and transition region temperature range. These problems can be mitigated by using only stars with good high-resolution spectra, both in the X-ray and UV bands. This will be subject of a future work. An intrinsic problem is also the presence of coronal activity cycles, with an X-ray amplitude that can range from a factor of  $\sim 2$  to a factor of  $\sim 50$ , depending on stellar activity levels. The two extreme cases observed to date are:  $\iota$  Hor ( $\log L_X/L_{bol} \sim -4.9$ ; Sanz-Forcada et al. 2019) and the solar cycle ( $\log L_X/L_{bol} \sim -5.9$  to  $-7.6$ ; Orlando et al. 2001). The problem of stellar cycles can only be solved by using the average value of an already known cycle, which is the case in very few stars. The problem is also mitigated if the UV data are taken contemporaneously to the X-ray data.

#### 4.3. Equivalent widths of the He I 10830 detections

To carry out a homogeneous analysis, we needed to revise some of the equivalent widths (*EWs*) of the previously published He detected planets with CARMENES. However, these changes were marginal. The *EWs* of planets HD 209458 b, HD 189733 b, GJ 3470 b, GJ 1214 b, WASP-69 b, and HAT-P-32 b were not changed and, thus, they were taken from Table 3 of Lampón et al. (2023). The *EWs* were integrated in the range  $10831.0-10834.5 \text{ \AA}$  (wavelengths in vacuum). For the *EW* of WASP-76 b, the upper limit of  $21.3 \text{ m\AA}$  reported by Casasayas-Barris et al. (2021) was adopted instead of the value of  $12.4 \text{ m\AA}$  reported by Lampón et al. (2023). The latter value was obtained by integrating in a wider range,  $10831.0-10835.5 \text{ \AA}$ , as the signal of this planet was significantly broadened and red-shifted. Except as noted, the same procedure was used for the planets with detected signal.

For WASP-52 b, the *EW* was calculated from the model fit to the data performed by Kirk et al. (2022). That fit shows an offset of  $0.1\%$ , which was subtracted. Kirk et al. (2022) also detected a small and rather noisy signal of WASP-177 b and used it to fit their model. The *EW* for the measured spectrum integrated in their spectral range is  $5.8 \text{ m\AA}$ , while that for the model is  $7.5 \text{ m\AA}$ . We took the mean value of  $6.65 \text{ m\AA}$ . For HAT-P-18 b, the *EW* was obtained from the absorption depth of  $0.46\%$  reported by Paragas et al. (2021) integrated over their bandpass of  $6.35 \text{ \AA}$ . The *EW* of HD 235088 b (TOI-1430 b) was reported by Orell-Miquel et al. (2023) with a value of  $9.5 \pm 1.1 \text{ m\AA}$ , while our value obtained by integrating over the usual  $10831.0-10834.5 \text{ \AA}$  spectral range is slightly larger,  $11.1 \text{ m\AA}$ . Zhang et al. (2023b) reported a value of  $6.6 \pm 0.5 \text{ m\AA}$  in a different observation.

Zhang et al. (2022a) reported a value for the *EW* of  $8.6 \pm 0.6 \text{ m\AA}$  in HD 73583 b (TOI 560 b). From their figures, by integrating over the spectral range described above, we obtained  $7.43 \text{ m\AA}$ . In the case of TOI-1268 b, we faced a similar problem. The *EW* by Orell-Miquel et al. (2024) is  $19.1 \text{ m\AA}$ . The value obtained with the method described above is  $17.7 \text{ m\AA}$ . We note that in this case the upper limit of the integration was slightly smaller,  $10834.2 \text{ \AA}$ , due to a lack of data. The same remarks apply to TOI-2018 b, where we calculated  $6.8 \text{ m\AA}$  instead of the value of  $7.8 \text{ m\AA}$  from Orell-Miquel et al. (2024).

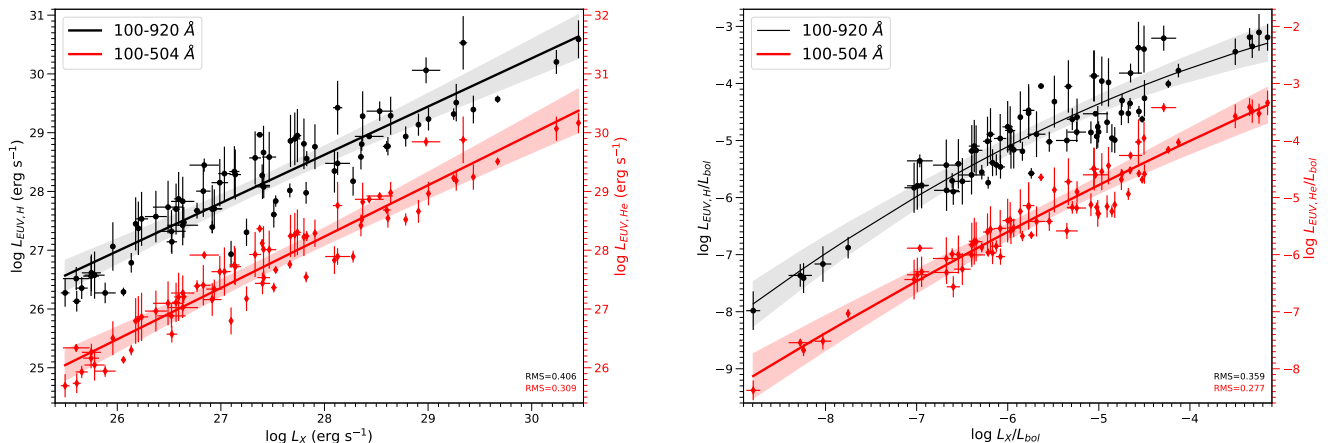


**Fig. 3.** EUV vs X-ray luminosities in two different EUV ranges for the H (100–920 Å) and He ionization (100–504 Å). There are different scales for the two EUV luminosity ranges. *Left:* Linear fit over EUV against X-ray luminosity. *Right:* Quadratic fit over the luminosity ratios with the bolometric luminosity.

HAT-P-67 b seems to show a rather variable He( $2^3\text{S}$ ) absorption (see, e.g., Bello-Arufe et al. 2023 and Gully-Santiago et al. 2024). The CARMENES measurement, reported by Bello-Arufe et al. (2023) in their Fig. 6b, seems to have a problem as the absorption profile shows an unrealistic emission-like feature at wavelengths shorter than 10832.5 Å. That feature was likely caused by their lack of a realistic out-of-transit baseline, which prevented them from making an appropriate normalization. That is, it could be due to an increased He I absorption at bluer wavelengths towards the end of the transit. This planet was observed with a longer baseline by Gully-Santiago et al. 2024. Hence, we decided to include these measurements in our analysis. By using our method for calculating the EW, we derived from their measurements shown in Fig. 13 (the in-transit mean taken in the visit of May 2020) a value of 147 mÅ. In this case, we consider the larger value of 25 mÅ that covers the significant variability shown by the planet as “error” of the EW and not the real measured uncertainty (see the mid-transit values in Fig. 9 of the work cited above). It is worth noting that Gully-Santiago et al. 2024 measured a rather large EW of  $\sim 330$  mÅ at the mid transit, as well as a significant pre-transit absorption of  $\sim 200$  mÅ (see their Fig. 9). They stated, however, that “only a small fraction of the He I excess signal would be expected to trace the planet’s motion.” Here we focus on the absorption of the He( $2^3\text{S}$ ) that is being ejected from the atmosphere, not in the He( $2^3\text{S}$ ) that has already been ejected and forms the cloud around the planet. Then, we can estimate this absorption by taking the difference of the EW at the mid transit, from that of the material already expelled (pre-transit). This results in an absorption of  $\sim 130$  mÅ, which is very close to the adopted value of 147 mÅ for the mid-transit measured in May 2020.

For HAT-P-26 b, the *EW* was obtained from the absorption depth of 0.31% reported by Vissapragada et al. (2022) integrated over their full width half maximum (FWHM) bandpass of 6.35 Å. We obtained a value of  $19.7 \pm 6.4$  mÅ. The warm super-puffy TOI-1420 b planet was observed by Vissapragada et al. (2024), who obtained a high ( $8.5\sigma$ ) He triplet signal, with an absorption depth of  $0.671\% \pm 0.079\%$ . With those values and taking the bandwidth of their filter of 6.4 Å, we obtained an *EW* of  $42.9 \pm 5.1$  mÅ.

#### 4.4. The relation between He I 10830 and XUV ionizing irradiation

It is expected that the formation of the He I 10830 triplet in an exoplanet atmosphere is related to the stellar irradiation on the planet by photons capable of ionizing the neutral helium atoms; namely, those with  $\lambda \lesssim 504$  Å. The actual process of formation of these lines requires also that electrons are available in the plasma for the recombination of He atoms after the radiative ionization, and the main origin of these electrons is the radiative ionization of H atoms by photons with  $\lambda \lesssim 912$  Å (we used 920 Å as ionization edge in our model to cover a slightly wider range). Furthermore, the stellar irradiation in this wavelength range also affects the He triplet concentration through the total density. As that radiation is responsible for the ionization of the H atmosphere, it changes the mean molecular weight and, hence, through the hydrodynamic equations, it affects the density. The stellar irradiation also affects the state of the upper atmosphere through the cooling and heating processes, which, in turn, affect the temperature and hence the hydrodynamic and the density. In addition, a third variable must be considered: the ionization of the ground level of orthohelium atoms, which takes place for  $\lambda \lesssim 2600$  Å (Kramida et al. 2023) and thus depends on the photospheric emission of the star. Although a combination of these three stellar fluxes should be considered, the right balance between the effects of the fluxes in the three bands is difficult to establish in a general way for all stars. Thus, we took the flux in the XUV range up to 504 Å ( $XUV_{\text{He}}$ ) as a proxy of these three processes, as it is expected to be the dominant term and, in a large number of stars, this flux is well correlated with  $XUV_{\text{H}}$ . Some attempts to derive such dependence have been undertaken<sup>9</sup>.

To further test this hypothesis, we collected information on the detections of the He I 10830 triplet reported to date (see below) to compare them with the  $XUV_{\text{He}}$  flux (Table C.4). However, not all the targets in the list have a complete coronal model to calculate the XUV contribution. For those cases we calculated the flux by indirect means. The quality of the  $XUV_{\text{He}}$  fluxes calculated decreases in this order (as noted in Fig. 4): (1) cases with both X-ray and UV spectra, resulting in a complete coronal model; (2) targets with X-ray spectra, but no UV spectra (the

<sup>9</sup> <https://zenodo.org/records/13986513>

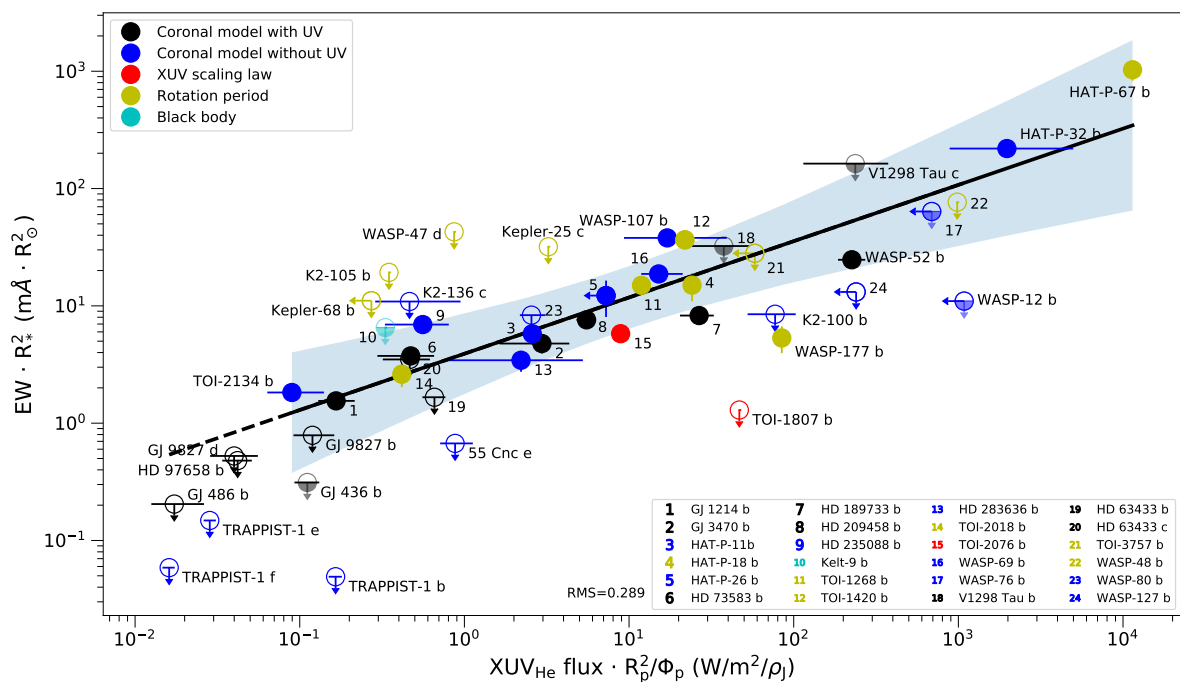


**Fig. 4.** He I 10830 triplet equivalent width, multiplied by the stellar area, plotted against  $F_{\text{XUV,He}}$ , weighted by  $\phi_p/R_p^2$ , i.e., by the planet density. The  $1\sigma$  error bands to the fit, calculated only with positive detections (filled symbols), are displayed in light blue. Different colors indicate the method used to calculate the XUV flux in the 5–504 Å range (see Sect. 4.4). Half-filled symbols are used for the equivalent width upper limits calculated by our team, while those calculated by other authors are shown in open symbols.

coronal model with lower temperature section is extrapolated); (3) X-ray bulk flux available, such as ROSAT fluxes, and the  $\text{XUV}_{\text{He}}$  flux is calculated using the scaling law in Eq. 5; (4) X-ray flux determined from the rotation period and the X-ray vs. rotation relation by Wright et al. (2011), with subsequent calculation of  $\text{XUV}_{\text{He}}$  flux; and (5) calculation of the  $\text{XUV}_{\text{He}}$  flux based on blackbody emission of the stellar photosphere, for a star with unlikely or negligible coronal emission (KELT-9)<sup>10</sup>. We also included upper limits for both the He detection and XUV flux. In case (2) the low temperature part of the coronal model is extrapolated from the high temperature section (SF11); upper and lower boundaries are considered during this extrapolation; thus, the XUV upper limits are based on the upper boundary coronal model, rather than on the central value used to evaluate the SED in different contexts, such as the case of WASP-12 of Czesla et al. (2024). The separate fits for the positive detections in the groups (1), (2), and (4) show consistency within the error bars with the general fit. In addition to the expected dependence of the He absorption on the stellar XUV irradiation as discussed above, we also empirically evaluated its dependence on other star-planet system parameters. The detailed discussion is found in Appendix B. Here, we include a summary of that formulation and the results.

The first point is that we choose as a proxy of the He( $2^3\text{S}$ ) absorption the  $EW$  of the absorption profile, instead of the depth (peak) of such profile, as chosen in some previous studies. The reason is that we are interested in relating the bulk He( $2^3\text{S}$ ) ab-

sorption by the planet atmosphere, and the  $EW$  is a better proxy since it is independent of the width of the absorption profile; namely, it is independent of its potential broadening by Doppler temperature and by the radial outflows of the escaping atmosphere.

The second aspect is the star’s surface. The transmission (or, equivalently, the  $EW$ ) is measured as a ratio of the equivalent He( $2^3\text{S}$ ) absorbing area of the planet atmosphere (usually expressed as the surface of a ring) and the area of the stellar disk ( $R_*^2$ ). If we are interested in the properties of the He( $2^3\text{S}$ ) absorption of a given planet atmosphere independently of the size of its host star, it seems reasonable to de-scale the measured  $EW$  by the stellar disk area; that is, to consider  $EW \cdot R_*^2$  instead of just  $EW$ .

An additional parameter that we considered is the planet gravitational potential,  $\Phi_p$ , as suggested by, for instance, the theoretical model of Salz et al. (2016) and the analysis of the He( $2^3\text{S}$ ) absorption in diverse planets carried out by Lampón et al. (2023). According to those studies the  $EW$  is expected to be inversely proportional to the gravitational field because for a planet with a weaker gravitational potential, the atmosphere is escaping more easily, leading to a more extended atmosphere and, hence, a larger absorption.

A further parameter that we considered is a geometric factor related to the planet size (see Appendix B), included in a general way with  $R_p^\gamma$ , where  $\gamma$  is likely to vary between 1 and 3 depending on the star-planet system. For planets with very compressed atmospheres as, for example, the case of HD 189733 b (Salz et al. 2018; Lampón et al. 2023), the  $EW$  is expected to be proportional to  $R_p$  ( $\gamma=1$ ). However, for those with very extended and flat He( $2^3\text{S}$ ) distributions, for instance, GJ 1214 b (Lampón et al.

<sup>10</sup> We are more confident on our calculation assuming a blackbody emission than on the X-ray flux upper limit provided in Table C.3. The  $\text{XUV}_{\text{H}}$  flux in this star is more than four orders of magnitude higher than  $\text{XUV}_{\text{He}}$  flux if we assume a blackbody emission.



2023), the exponent  $\gamma$  could be larger than 2. Thus, the relationship that we considered generally takes the form (see Eq. B.13):

$$EW \cdot R_{\star}^2 \approx \frac{F_{\text{XUV}} R_{\text{p}}^{\gamma}}{\Phi_{\text{p}}}. \quad (6)$$

We performed several tests for different relationships between  $EW$  and XUV fluxes, as well as for Eq. 6, using different values of the exponent  $\gamma$  of  $R_{\text{p}}^{\gamma}$  (Table B.1). The  $EW$  values collected for all planets with detected He( $2^3\text{S}$ ) signal and the  $\text{XUV}_{\text{He}}$  fluxes and other parameters listed in Table C.4 were used. The stellar spectral type is also listed in the Table to alert for the possible photospheric contribution at wavelengths below  $2600 \text{ \AA}$ .

The results for the simple relationship between  $EW$  and  $F_{\text{XUV}}$  (see Fig. B.2) yields a decent Pearson's correlation coefficient of  $r = 0.579$ , but clearly inferior to other tests described below. The correlation coefficient of the fit largely improves to a value of  $r = 0.782$  when scaling the  $EW$  by the area of the star's disk (see Fig. B.3). A further test was performed by using Eq. 6 with a value of  $\gamma = 1$ , namely,  $EW$  proportional to  $R_{\text{p}}$  (see Fig. B.3). The correlation coefficient obtained in this case is even better, reaching the value of  $r = 0.891$ . A subsequent test was performed by considering  $\gamma = 2$ , namely,  $EW$  proportional to  $R_{\text{p}}^2$  (see Fig. 4), yielding a slightly better correlation than in the previous case,  $r = 0.898$ . We then proceeded to use the latter fit, which resulted in an empirical equation, excluding upper limits, of

$$\log(EW \cdot R_{\star}^2) = \alpha \cdot \left( \log \left( \frac{F_{\text{XUV,He}} \cdot R_{\text{p}}^2}{\phi_{\text{p}}} \right) - 0.96 \right) + \beta, \quad (7)$$

where  $\alpha = 0.480 \pm 0.054$  and  $\beta = 1.052 \pm 0.066$ . The  $EW$  is given in  $\text{m\AA}$ , the stellar radius,  $R_{\star}$ , in  $R_{\odot}$  units,  $F_{\text{XUV,He}}$  in  $\text{W/m}^2$ , and  $R_{\text{p}}^2/\Phi_{\text{p}}$ , which is equivalent to the inverse planet density,  $\rho_{\text{p}}^{-1}$ , in Jovian units. Error bars include the uncertainties in all of these quantities.

## 5. Discussion

The effects of high-energy stellar irradiation on the exoplanet atmospheres has been subject of increasing interest in recent years. The effects on the planet atmospheres are not limited to the formation of lines such as the He I 10830 triplet, but they also affect large scale phenomena such as atmospheric mass loss (atmospheric escape). The actual mass loss rate of a planet depends also on other variables different from stellar irradiation, such as atmospheric composition, stellar winds, or presence of planetary magnetic fields, and it requires an individualized approach to every case (e.g., Kubyshkina et al. 2018). However Eq. 1 is widely used to roughly compare the expected planet evolution of different cases. Since atmospheric photoevaporation should lead to atmospheric instability, a planet with a current high mass loss rate is unlikely to be habitable. The approach in Eq. 1 assumes that the atmosphere is based mainly on H, which can be appropriate for Jovian-like planets, but it may not be applicable in the case of rocky planets such as Teegarden's star b or TRAPPIST-1 b. In any case, modeling or analyzing planet atmospheres requires (as accurate as possible) knowledge of XUV stellar irradiation. With this work, we are providing new XUV synthetic SEDs for planet-hosting stars, which represents an improvement with respect to the X-exoplanets first release (SF11) by updating the stellar coronal models and the atomic data used to model the

emission from corona and transition region. However, the number of planets hosting stars that have accurate X-ray spectra is quite limited. For those cases that do not, we include new XUV scaling laws that can be easily applied even in absence of an X-ray detection (e.g., by using the rotation period of the star, as explained in Sect. 4). For more in-depth studies, we advise users to select a star with a similar stellar spectral type and  $\log L_{\text{X}}/L_{\text{bol}}$  as a proxy. A more detailed work providing a grid of models of this kind will be released in the near future.

### 5.1. XUV scaling laws

Early works dealing with the planet photoevaporation problem assumed that the XUV emission from exoplanet host stars would be similar to the solar spectrum, scaled by the size of the star (Lecavelier Des Etangs 2007). Alternatively, they have made use of the UV flux from the Sun and a young star for their calculations (Murray-Clay et al. 2009). A slight variation was applied by Linsky et al. (2014), France et al. (2016), and Sreejith et al. (2020), who used the solar EUV SED scaled by the overall emission in X-rays and UV of the stars. Their models were subsequently used, for instance, in Vissapragada et al. (2022), but their XUV fluxes are discrepant with ours by up to a factor of six. This approach is deficient, given that EUV spectra of active stars can be very different from those of quiet stars like the Sun (e.g., Sanz-Forcada et al. 2003a). Namekata et al. (2023) used the stellar magnetic flux and the solar spectra to extrapolate the XUV flux in active solar-like stars. The relation is calibrated mainly based on solar data, with some data coming from more active stars, along with additional uncertainties as the stellar magnetic flux is required.

A different approach was introduced by SF11, including coronal models built with X-rays and UV data to create synthetic SEDs in the non-observed EUV spectral range. A relation between the transition region and the corona was calibrated using coronal models based on EUVE and International Ultraviolet Explorer (IUE) data, then used to complement the coronal models of stars with no UV data available. One of the results of this approach was a scaling law between X-rays and EUV luminosity that could be applied for cases where only a broadband X-ray flux is known. Chadney et al. (2015) tried to apply a more physical relation between X-rays and EUV emission by considering the activity level of the star (using the surface stellar flux,  $F_{\text{X}}$  and  $F_{\text{EUV}}$ ) in six stars, one of them based on actual solar data. King et al. (2018) followed a similar approach (without defining the  $F_{\text{X}}$  used) using the same stellar data from three stars, along with solar data with some corrections applied with respect to Chadney et al. (2015). In both cases the sample was small, with most information taken from the Sun and a few very active stars. In addition, the use of stellar radius introduces further uncertainties to the problem. Johnstone et al. (2021) calibrated a relation between X-rays ( $5\text{--}124 \text{ \AA}$ ) and the EUV surface flux in the range  $100\text{--}360 \text{ \AA}$  in a sample dominated by active stars, where a new set of solar data was included. The stellar data in this case came from EUVE spectra, but with some spectra having a low quality above  $180 \text{ \AA}$  (Sanz-Forcada et al. 2003a), and being usually contaminated by geocoronal emission around the He II  $\lambda 304 \text{ \AA}$  line. As in the other cases, this calibration also propagates the uncertainties of the stellar radii. For the rest of the EUV range,  $360\text{--}920 \text{ \AA}$ , Johnstone et al. (2021) extrapolated the ratio between these two EUV bands in the Sun to the entire range of stellar activity. While plasma in X-rays and in the EUV  $100\text{--}360 \text{ \AA}$  range is mainly made of spectral lines (and contin-

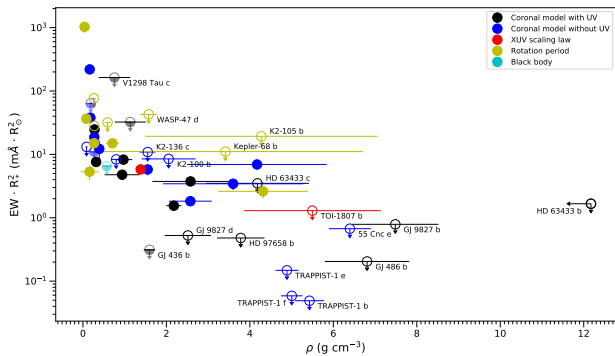


**Fig. 5.** He I 10830 triplet equivalent width, multiplied by the stellar area, plotted against planet density  $1\sigma$  error bars are indicated. Same colors and symbols to Fig. 4 apply for an easier identification. Labels are included for some planets detected as upper limits (see Sect. 5.2).

uum) formed above  $10^6$  K, the  $360\text{--}920$  Å flux has a substantial contribution of lines formed at lower temperatures. Thus, it is not evident that the solar spectrum paradigm can be used for the active stars. The range of activity levels explored by Johnstone et al. (2021) included only a few low-activity stars, which are, nonetheless, still more active than some of our stars. Further comparison with these three relations is shown in Appendix A. More recently Krishnamurthy & Cowan (2024) made use of the relation between age and X-ray luminosity applied by SF11 to calculate the accumulated XUV flux over time on a planet atmosphere. While the X-ray luminosity can be used, in general terms, to estimate an approximate stellar age, the opposite is not advisable. Obtaining an accurate measurement of a stellar age is a difficult task in astrophysics; thus, using a poorly determined stellar age to calculate the X-ray and EUV fluxes may end up accumulating large uncertainties. We prefer to calculate the X-rays flux from stellar rotation if no actual measurement is available.

The new scaling law that we provide in Eq. 4 and Fig. 3 solves the limitations of past works by using coronal models for the calibration of the relation. It also uses variables that also depend on the stellar activity level to sample better the different ranges of activity. This new relation overcomes the observed problems with high activity stars (Maggio et al. 2023) and covers a wide range of activity levels. We also calculated a new relation in the range that affects the neutral helium ionization, namely,  $\lambda < 504$  Å (Eq. 5). This allows us to better estimate the impact of the stellar high-energy irradiation on the line formation of the planetary He I 10830 triplet. Further comparisons with other recent works in the literature are provided in Appendix A.

## 5.2. The empirical relation between XUV and He I 10830

Earlier attempts to find an empirical relation between He I 10830 equivalent width and XUV (either at the H or the He ionization edges) have only indicated a trend, but not a clear relation (Nortmann et al. 2018; Fossati et al. 2022; Kirk et al. 2022; Allart et al. 2023). To evaluate the relation, these authors used  $\delta R_p/H_{\text{eq}}$ , which is the amplitude of excess helium absorption observed, in units of the planets’ atmospheric scale heights, against the XUV stellar flux at the planet. A further study by Zhang et al. (2023a) used a different approach. They did not use the atmospheric scale height, which strictly speaking, corresponds to hydrostatic but not to hydrodynamic conditions. Instead, they plotted the mass-loss rate estimated from observations versus the

theoretical energy-limited mass-loss rate (i.e., assuming a heating efficiency of 1), where the former were assumed proportional to  $R_{\text{star}} \cdot EW$  and the latter to  $F_{\text{XUV,H}}/\rho_{\text{XUV}}$ , where  $\rho_{\text{XUV}}$  is the density of the planet calculated with the planet radius of XUV absorption ( $R_{\text{XUV}}$ ). In that way, they reached a rather good correlation.

To reduce the data dispersion in those relationships, we sought alternative parametrizations. The He I 10830 equivalent width and the XUV<sub>He</sub> irradiation cannot directly be related with each other, as this relation neglects the impact of the stellar radius on the depth of any absorption signals measured, and the impact of the planet radius on the irradiation energy received by the planet. We therefore used the  $EW$  multiplied by stellar area, and the XUV<sub>He</sub> flux multiplied by the planetary disk area and divided by the planetary gravitational potential (equivalent to a division by the planet density; see Sect. 4.4, Fig. 4, and Table C.4).

Although the observed empirical trend is clear, some dispersion is still present in the data. One reason could be the contribution of photospheric flux with  $\lambda < 2600$  Å, which ionizes the ground level of the He triplet, diminishing the expected absorption of the line. However, no deviation related to the spectral type is evident. Other relevant factors are likely related to the atmospheric composition, whether there is a primordial atmosphere, mainly composed of H and He, or the current He content is lower. Some outliers (the TRAPPIST-1 planets, 55 Cnc e, TOI-1807 b, GJ 486 b, GJ 9827 b) lie below the He level that would be expected for their XUV irradiation: because of their Earth- and super-Earth size and high densities (Fig. 5, Table C.4), they may be fully rocky without an atmosphere or they may have an atmosphere that is rather tenuous; otherwise, it may be thick, but with a high mean molecular weight. Some upper limits correspond to sub-Neptunian planets (GJ 9827 d, GJ 436 b, HD 97658 b, K2-100 b), which might have atmospheric conditions and chemical compositions that complicate the helium detection with current instrumentation. From Figs. 4 and 5, we identify that among planets with density lower than  $2 \text{ g cm}^{-3}$ , 15 out of 28 planets were detected ( $54 \pm 4\%$ ). Yet another physical reason that could explain the dispersion observed is stellar variability. The ionization levels of He I depend on the stellar XUV emission, which is highly variable, especially during flares. However, the XUV level is based on X-ray observations that are not simultaneous to the He I 10830 observations. An issue that is more related to the data acquisition and analysis is the difficulties in the measurements of exoplanets orbiting distant (i.e., faint) stars. In the particular case of WASP-177 b, Kirk et al. (2022) had some problems with systematics in the measurement of the He triplet. Another source of dispersion could be the actual dependence on the planet radius or surface, as explained in Appendix B.

## 6. Conclusions

Planet atmospheric photoevaporation takes place due to XUV ( $\lambda \lesssim 920$  Å) stellar irradiation. The He I 10830 Å triplet is used to study this phenomenon. The formation of the line in a planet atmospheric environment follows a process of ionization by photons with  $\lambda < 504$  Å, followed by a recombination with electrons that are mainly the result of hydrogen ionization (by photons with  $\lambda < 912$  Å). The main problem to evaluate the stellar flux at those wavelengths is the absorption of these photons by the ISM. To overcome this problem, we constructed coronal (and transition region) models of the star. We then calculated a synthetic SED in the whole XUV range ( $\lambda \sim 5 - 920$  Å).

We analyzed new *XMM-Newton*, *Chandra*, and EUV spectra of 50 stars, either from proprietary or archival observations. We also used high-resolution spectra to measure individual lines formed at these temperatures in 5 stars. In the case of 26 stars, we extended the analysis to the transition region temperatures by measuring UV lines in high-resolution spectra from HST and FUSE. We built detailed emission measure distributions (EMDs) for this group. We also updated the analysis of the spectra in X-exoplanets (SF11) using the latest Gaia distances, and the latest version of ATOMDB. The overall sample includes 100 stars hosting 163 planets, of which 75 stars have  $S/N > 3$ , and the rest are considered upper limits. The whole sample, excluding upper limits, was then used to calculate new scaling laws for an easier calculation of the broadband fluxes that matter for the He and H ionization. A new approach to the problem was introduced by using the X-ray and EUV luminosity weighted by the bolometric luminosity. This allows us to remove effects related to stellar size, while closely considering the behavior of the scaling laws with the stellar activity. Future improvements will include more coronal high quality EMDs to reduce the dispersion observed in the data when the low-resolution X-ray spectra alone are used to model the coronae.

The newly calculated scaling laws are then used to evaluate the stellar He-ionizing irradiation in 48 exoplanets for which the He I  $10830$  Å triplet has been measured, including upper limits. In the cases with no X-rays measurements, we used an X-ray luminosity based on the stellar rotation period. We then checked the expected trend of the formation of this line in exoplanet atmospheres with the  $XUV_{\text{He}}$  stellar irradiation. A clear relation is observed, once the planet gravitational potential, along with the stellar and planetary surface are included. The remaining dispersion observed in the data can be attributed to the He content in the planet atmospheres. Some outliers, such as the TRAPPIST-1 b, e, and f planets, as well as 55 Cnc e, could be explained by the lack of planetary gaseous atmospheres. The stellar variability and the difficulties to measure the He I  $10830$  Å triplet in the transmission spectrum of the planet also contribute to the data dispersion. The observed relation can be used to predict the detectability of the He I  $10830$  Å triplet in a transiting planet.

## Data availability

The SEDs modeled are listed in Table 1, only available in electronic form at the CDS via anonymous ftp to [cdsarc.u-strasbg.fr](http://cdsarc.u-strasbg.fr) (130.79.128.5) or via <http://cdsweb.u-strasbg.fr/cgi-bin/qcat?J/A+A/>.

**Acknowledgements.** We thank the anonymous referee for the useful comments that helped improve the manuscript. We acknowledge financial support from the Agencia Estatal de Investigación (AEI/10.13039/501100011033) of the Ministerio de Ciencia e Innovación and the ERDF “A way of making Europe” through projects PID2022-137241NB-C41[1:4], PID2022-141216NB-I00, PID2021-125627OB-C31, and the Centre of Excellence “Severo Ochoa” and “María de Maeztu” awards to the Instituto de Astrofísica de Canarias (CEX2019-000920-S), Instituto de Astrofísica de Andalucía (CEX2021-001131-S) and Institut de Ciències de l’Espai (CEX2020-001058-M). We also acknowledge the support of the DFG priority program SPP 1992 “Exploring the Diversity of Extrasolar Planets” (CZ 222/5-1). We acknowledge Norbert Scharfel for the observations granted as *XMM-Newton* Director Discretionary Time (DDT). This research has made use of the NASA’s High Energy Astrophysics Science Archive Research Center (HEASARC), and it is based on observations made with HST, FUSE, EUVE, *XMM-Newton* and *Chandra*, and obtained from the MAST data archive at the Space Telescope Science Institute, and the public archives of *XMM-Newton* and *Chandra*. CARMENES is an instrument at the Centro Astronómico Hispano en Andalucía (CAHA) at Calar Alto (Almería, Spain), operated jointly by the Junta de Andalucía and the Instituto de Astrofísica de Andalucía (CSIC). CARMENES was funded by the Max-Planck-Gesellschaft (MPG), the Consejo Superior de Investigaciones Científicas (CSIC), the Min-

isterio de Economía y Competitividad (MINECO) and the European Regional Development Fund (ERDF) through projects FICTS-2011-02, ICTS-2017-07-CAHA-4, and CAHA16-CE-3978, and the members of the CARMENES Consortium (Max-Planck-Institut für Astronomie, Instituto de Astrofísica de Andalucía, Landessternwarte Königstuhl, Institut de Ciències de l’Espai, Institut für Astrophysik Göttingen, Universidad Complutense de Madrid, Thüringer Landessternwarte Tautenburg, Instituto de Astrofísica de Canarias, Hamburger Sternwarte, Centro de Astrobiología and Centro Astronómico Hispano-Alemán), with additional contributions by the MINECO, the Deutsche Forschungsgemeinschaft (DFG) through the Major Research Instrumentation Programme and Research Unit FOR2544 “Blue Planets around Red Stars”, the Klaus Tschira Stiftung, the states of Baden-Württemberg and Niedersachsen, and by the Junta de Andalucía.

## References

- Agol, E., Dorn, C., Grimm, S. L., et al. 2021, *PSJ*, 2, 1  
 Allart, R., Bourrier, V., Lovis, C., et al. 2019, *A&A*, 623, A58  
 Allart, R., Bourrier, V., Lovis, C., et al. 2018, *Science*, 362, 1384  
 Allart, R., Lemée-Joliecoeur, P. B., Jaziri, A. Y., et al. 2023, *A&A*, 677, A164  
 Alonso-Floriano, F. J., Snellen, I. A. G., Czesla, S., et al. 2019, *A&A*, 629, A110  
 Anders, E. & Grevesse, N. 1989, *Geochim. Cosmochim. Acta*, 53, 197  
 Anderson, D. R., Collier Cameron, A., Delrez, L., et al. 2014, *MNRAS*, 445, 1114  
 Anderson, D. R., Collier Cameron, A., Delrez, L., et al. 2017, *A&A*, 604, A110  
 Andretta, V. & Giampapa, M. S. 1995, *ApJ*, 439, 405  
 Barragán, O., Aigrain, S., Kubyskhina, D., et al. 2019, *MNRAS*, 490, 698  
 Barragán, O., Armstrong, D. J., Gandolfi, D., et al. 2022, *MNRAS*, 514, 1606  
 Bello-Arufe, A., Knutson, H. A., Mendonça, J. M., et al. 2023, *AJ*, 166, 69  
 Bennett, K. A., Redfield, S., Oklopčić, A., et al. 2023, *AJ*, 165, 264  
 Bonomo, A. S., Desidera, S., Benatti, S., et al. 2017, *A&A*, 602, A107  
 Borsa, F., Rainer, M., Bonomo, A. S., et al. 2019, *A&A*, 631, A34  
 Bowyer, S., Drake, J. J., & Vennes, S. 2000, *ARA&A*, 38, 231  
 Brickhouse, N. S. & Dupree, A. K. 1998, *ApJ*, 502, 918  
 Caballero, J. A., González-Álvarez, E., Brady, M., et al. 2022, *A&A*, 665, A120  
 Carleo, I., Malavolta, L., Lanza, A. F., et al. 2020, *A&A*, 638, A5  
 Carleo, I., Youngblood, A., Redfield, S., et al. 2021, *AJ*, 161, 136  
 Casasayas-Barris, N., Orell-Miquel, J., Stangret, M., et al. 2021, *A&A*, 654, A163  
 Chadney, J. M., Galand, M., Unruh, Y. C., Koskinen, T. T., & Sanz-Forcada, J. 2015, *Icarus*, 250, 357  
 Charbonneau, D., Brown, T. M., Noyes, R. W., & Gilliland, R. L. 2002, *ApJ*, 568, 377  
 Cifuentes, C., Caballero, J. A., Cortés-Contreras, M., et al. 2020, *A&A*, 642, A115  
 Cloutier, R., Charbonneau, D., Deming, D., Bonfils, X., & Astudillo-Defru, N. 2021, *AJ*, 162, 174  
 Crida, A., Ligi, R., Dorn, C., & Lebreton, Y. 2018, *ApJ*, 860, 122  
 Czesla, S., Lampón, M., Cont, D., et al. 2024, *A&A*, 683, A67  
 Czesla, S., Lampón, M., Sanz-Forcada, J., et al. 2022, *A&A*, 657, A6  
 Dai, F., Schlaufman, K. C., Reggiani, H., et al. 2023, *AJ*, 166, 49  
 Del Zanna, G., Landini, M., & Mason, H. E. 2002, *A&A*, 385, 968  
 den Herder, J. W., Brinkman, A. C., Kahn, S. M., et al. 2001, *A&A*, 365, L7  
 dos Santos, L. A., Ehrenreich, D., Bourrier, V., et al. 2020, *A&A*, 640, A29  
 Dupree, A. K., Sasselov, D. D., & Lester, J. B. 1992, *ApJ*, 387, L85  
 Duvvuri, G. M., Sebastian Pineda, J., Berta-Thompson, Z. K., et al. 2021, *ApJ*, 913, 40  
 Enoch, B., Anderson, D. R., Barros, S. C. C., et al. 2011, *AJ*, 142, 86  
 Favata, F. & Micela, G. 2003, *Space Sci. Rev.*, 108, 577  
 Fossati, L., Guilluy, G., Shaikhislamov, I. F., et al. 2022, *A&A*, 658, A136  
 Fossati, L., Pillitteri, I., Shaikhislamov, I. F., et al. 2023, *A&A*, 673, A37  
 France, K., Loyd, R. O. P., Youngblood, A., et al. 2016, *ApJ*, 820, 89  
 France, K., Stocke, J. T., Yang, H., et al. 2010, *ApJ*, 712, 1277  
 Gaia Collaboration, Vallenari, A., Brown, A. G. A., et al. 2023, *A&A*, 674, A1  
 Gaidos, E., Hirano, T., Mann, A. W., et al. 2020, *MNRAS*, 495, 650  
 Gaidos, E., Hirano, T., Omiya, M., et al. 2021, *Research Notes of the AAS*, 5, 238  
 Güdel, M. 2004, *A&A Rev.*, 12, 71  
 Gully-Santiago, M., Morley, C. V., Luna, J., et al. 2024, *AJ*, 167, 142  
 Haisch, B., Bowyer, S., & Malina, R. F. 1993, *Journal of the British Interplanetary Society*, 46, 331  
 Hartman, J. D., Bakos, G. Á., Kipping, D. M., et al. 2011, *ApJ*, 728, 138  
 Hébrard, G., Collier Cameron, A., Brown, D. J. A., et al. 2013, *A&A*, 549, A134  
 Hedges, C., Hughes, A., Zhou, G., et al. 2021, *AJ*, 162, 54  
 Houck, J. C. & Demicola, L. A. 2000, in *ASP Conf. Series*, Vol. 216, *Astronomical Data Analysis Software and Systems IX*, ed. N. Manset, C. Veillet, & D. Crabtree, 591  
 Johnstone, C. P., Bartel, M., & Güdel, M. 2021, *A&A*, 649, A96

- Kanodia, S., Libby-Roberts, J., Cañas, C. I., et al. 2022, *AJ*, 164, 81
- Kasper, D., Bean, J. L., Oklopčić, A., et al. 2020, *AJ*, 160, 258
- Kimble, R. A., Woodgate, B. E., Bowers, C. W., et al. 1998, *ApJ*, 492, L83
- King, G. W., Wheatley, P. J., Salz, M., et al. 2018, *MNRAS*, 478, 1193
- Kirk, J., Dos Santos, L. A., López-Morales, M., et al. 2022, *AJ*, 164, 24
- Knutson, H. A., Fulton, B. J., Montet, B. T., et al. 2014, *ApJ*, 785, 126
- Kosiarek, M. R., Berardo, D. A., Crossfield, I. J. M., et al. 2021, *AJ*, 161, 47
- Kosiarek, M. R., Crossfield, I. J. M., Hardegree-Ullman, K. K., et al. 2019, *AJ*, 157, 97
- Kossakowski, D., Kürster, M., Henning, T., et al. 2022, *A&A*, 666, A143
- Kramida, A., Yu. Ralchenko, Reader, J., & and NIST ASD Team. 2023, NIST Atomic Spectra Database (ver. 5.11), [Online]. Available: <https://physics.nist.gov/asd> [2023, December 21]. National Institute of Standards and Technology, Gaithersburg, MD.
- Krishnamurthy, V. & Cowan, N. B. 2024, *AJ*, 168, 30
- Krishnamurthy, V., Hirano, T., Stefánsson, G., et al. 2021, *AJ*, 162, 82
- Kubyskhina, D., Fossati, L., Erkaev, N. V., et al. 2018, *ApJ*, 866, L18
- Lam, K. W. F., Faedi, F., Brown, D. J. A., et al. 2017, *A&A*, 599, A3
- Lampón, M., López-Puertas, M., Lara, L. M., et al. 2020, *A&A*, 636, A13
- Lampón, M., López-Puertas, M., Sanz-Forcada, J., et al. 2023, *A&A*, 673, A140
- Lampón, M., López-Puertas, M., Sanz-Forcada, J., et al. 2021, *A&A*, 647, A129
- Lecavelier Des Etangs, A. 2007, *A&A*, 461, 1185
- Linsky, J. L., Fontenla, J., & France, K. 2014, *ApJ*, 780, 61
- Louden, T., Wheatley, P. J., & Briggs, K. 2017, *MNRAS*, 464, 2396
- Lubin, J., Robertson, P., Stefánsson, G., et al. 2021, *AJ*, 162, 61
- Madhusudhan, N. 2019, *ARA&A*, 57, 617
- Maggio, A., Pillitteri, I., Argiroffi, C., et al. 2023, *ApJ*, 951, 18
- Maggio, A., Sanz-Forcada, J., & Scelsi, L. 2011, *A&A*, 527, A144
- Mallorquín, M., Béjar, V. J. S., Lodieu, N., et al. 2023, *A&A*, 671, A163
- Mann, A. W., Vanderburg, A., Rizzuto, A. C., et al. 2018, *AJ*, 155, 4
- Mansfield, M., Bean, J. L., Oklopčić, A., et al. 2018, *ApJ*, 868, L34
- Masson, A., Vinatier, S., Bézard, B., et al. 2024, *A&A*, 688, A179
- Mills, S. M., Howard, A. W., Weiss, L. M., et al. 2019, *AJ*, 157, 145
- Moos, H. W., Cash, W. C., Cowie, L. L., et al. 2000, *ApJ*, 538, L1
- Moutou, C., Coustenis, A., Schneider, J., Queloz, D., & Mayor, M. 2003, *A&A*, 405, 341
- Murray-Clay, R. A., Chiang, E. I., & Murray, N. 2009, *ApJ*, 693, 23
- Namekata, K., Toriumi, S., Airapetian, V. S., et al. 2023, *ApJ*, 945, 147
- Nardiello, D., Malavolta, L., Desidera, S., et al. 2022, *A&A*, 664, A163
- Narita, N., Hirano, T., Fukui, A., et al. 2017, *PASJ*, 69, 29
- Nortmann, L., Pallé, E., Salz, M., et al. 2018, *Science*, 362, 1388
- Oklopčić, A. & Hirata, C. M. 2018, *ApJ*, 855, L11
- Orell-Miquel, J., Lampón, M., López-Puertas, M., et al. 2023, *A&A*, 677, A56
- Orell-Miquel, J., Murgas, F., Pallé, E., et al. 2022, *A&A*, 659, A55
- Orell-Miquel, J., Murgas, F., Pallé, E., et al. 2024, *A&A*, 689, A179
- Orlando, S., Peres, G., & Reale, F. 2001, *ApJ*, 560, 499
- Osterman, S., Green, J., Froning, C., et al. 2011, *Ap&SS*, 335, 257
- Palle, E., Nortmann, L., Casasayas-Barris, N., et al. 2020, *A&A*, 638, A61
- Paragas, K., Vissapragada, S., Knutson, H. A., et al. 2021, *ApJ*, 909, L10
- Paredes, L. A., Henry, T. J., Quinn, S. N., et al. 2021, *AJ*, 162, 176
- Pecaut, M. J. & Mamajek, E. E. 2013, *ApJS*, 208, 9
- Pizzolato, N., Maggio, A., Micela, G., Sciortino, S., & Ventura, P. 2003, *A&A*, 397, 147
- Poppenhaeger, K. 2022, *MNRAS*, 512, 1751
- Quirrenbach, A., Amado, P. J., Caballero, J. A., et al. 2014, in *Society of Photo-Optical Instrumentation Engineers (SPIE) Conference Series*, Vol. 9147, Society of Photo-Optical Instrumentation Engineers (SPIE) Conference Series
- Raymond, J. C. 1988, in *NATO ASIC Proc. 249: Hot Thin Plasmas in Astrophysics*, ed. R. Pallavicini, 3
- Rescigno, F., Hébrard, G., Vanderburg, A., et al. 2024, *MNRAS*, 527, 5385
- Ribas, I., Tuomi, M., Reiners, A., et al. 2018, *Nature*, 563, 365
- Salz, M., Czesla, S., Schneider, P. C., et al. 2018, *A&A*, 620, A97
- Salz, M., Czesla, S., Schneider, P. C., & Schmitt, J. H. M. M. 2016, *A&A*, 586, A75
- Sanz-Forcada, J., Brickhouse, N. S., & Dupree, A. K. 2003a, *ApJS*, 145, 147
- Sanz-Forcada, J. & Dupree, A. K. 2008, *A&A*, 488, 715
- Sanz-Forcada, J., Maggio, A., & Micela, G. 2003b, *A&A*, 408, 1087
- Sanz-Forcada, J. & Micela, G. 2002, *A&A*, 394, 653
- Sanz-Forcada, J., Micela, G., Ribas, I., et al. 2011, *A&A*, 532, A6
- Sanz-Forcada, J., Ribas, I., Micela, G., et al. 2010, *A&A*, 511, L8
- Sanz-Forcada, J., Stelzer, B., Coffaro, M., Raetz, S., & Alvarado-Gómez, J. D. 2019, *A&A*, 631, A45
- Schrijver, C. J., Mewe, R., van den Oord, G. H. J., & Kaastra, J. S. 1995, *A&A*, 302, 438
- Seager, S. & Sasselov, D. D. 2000, *ApJ*, 537, 916
- Sikora, J., Rowe, J., Barat, S., et al. 2023, *AJ*, 165, 250
- Smith, R. K., Brickhouse, N. S., Liedahl, D. A., & Raymond, J. C. 2001, *ApJ*, 556, L91
- Spake, J. J., Sing, D. K., Evans, T. M., et al. 2018, *Nature*, 557, 68
- Sreejith, A. G., Fossati, L., Youngblood, A., France, K., & Ambily, S. 2020, *A&A*, 644, A67
- Strüder, L., Briel, U., Dennerl, K., et al. 2001, *A&A*, 365, L18
- Suárez Mascareño, A., Damasso, M., Lodieu, N., et al. 2021, *Nature Astronomy*, 6, 232
- Triaud, A. H. M. J., Anderson, D. R., Collier Cameron, A., et al. 2013, *A&A*, 551, A80
- Trifonov, T., Kürster, M., Zechmeister, M., et al. 2018, *A&A*, 609, A117
- Tuomi, M., Jones, H. R. A., Barnes, J. R., et al. 2018, *AJ*, 155, 192
- Turner, J. D., Ridden-Harper, A., & Jayawardhana, R. 2021, *AJ*, 161, 72
- Turner, M. J. L., Abbey, A., Arnaud, M., et al. 2001, *A&A*, 365, L27
- Turner, O. D., Anderson, D. R., Barkaoui, K., et al. 2019, *MNRAS*, 485, 5790
- Van Grootel, V., Gillon, M., Valencia, D., et al. 2014, *ApJ*, 786, 2
- Vanderburg, A., Becker, J. C., Buchhave, L. A., et al. 2017, *AJ*, 154, 237
- Vidal-Madjar, A., Lecavelier des Etangs, A., Désert, J.-M., et al. 2003, *Nature*, 422, 143
- Vissapragada, S., Greklek-McKeon, M., Linssen, D., et al. 2024, *AJ*, 167, 199
- Vissapragada, S., Knutson, H. A., Greklek-McKeon, M., et al. 2022, *AJ*, 164, 234
- Šubjak, J., Endl, M., Chaturvedi, P., et al. 2022, *A&A*, 662, A107
- Wang, J. & Ford, E. B. 2011, *MNRAS*, 418, 1822
- Weisskopf, M. C., Brinkman, B., Canizares, C., et al. 2002, *PASP*, 114, 1
- West, R. G., Hellier, C., Almenara, J. M., et al. 2016, *A&A*, 585, A126
- Wright, N. J., Drake, J. J., Mamajek, E. E., & Henry, G. W. 2011, *ApJ*, 743, 48
- Yee, S. W., Petigura, E. A., Fulton, B. J., et al. 2018, *AJ*, 155, 255
- Yoshida, S., Vissapragada, S., Latham, D. W., et al. 2023, *AJ*, 166, 181
- Zarro, D. M. & Zirin, H. 1986, *ApJ*, 304, 365
- Zhang, M., Dai, F., Bean, J. L., Knutson, H. A., & Rescigno, F. 2023a, *ApJ*, 953, L25
- Zhang, M., Knutson, H. A., Dai, F., et al. 2023b, *AJ*, 165, 62
- Zhang, M., Knutson, H. A., Wang, L., Dai, F., & Barragán, O. 2022a, *AJ*, 163, 67
- Zhang, M., Knutson, H. A., Wang, L., et al. 2022b, *AJ*, 163, 68
- Zhang, M., Knutson, H. A., Wang, L., et al. 2021, *AJ*, 161, 181

## Appendix A: Comparison with other XUV determination approaches

In this section, we show further comparisons between our XUV modeling approach and others employed in the literature, as outlined in Sect. 4. Here, we also discuss in more detail the use of DEM polynomial fits as an alternative technique to our EMD. The results from our scaling laws are also compared against other works in the literature.

### A.1. Comparison with polynomial fits of the differential emission measure

Some recent publications have developed a technique to calculate the DEM of a star by fitting smooth polynomial functions (Louden et al. 2017; Duvvuri et al. 2021, hereafter LOU17 and DUV21 respectively). Here we compare our results with those of LOU17 and DUV21. G. Duvvuri kindly provided the DEM solutions for three targets in common with ours: AU Mic, Barnard’s Star, and Trappist-1. A similar approach was applied by LOU17 to determine the DEM of HD 209458. To transform their DEM into volume DEM at the distances ( $d'$ ) used in our work, we corrected by the stellar radius ( $R$ ) and distance ( $d$ ) used by them. Although the basic concept of DEM and EMD are similar, there are differences in the way they relate to the temperature. Therefore we needed to transform the DEM into EMD. The definition of the DEM and EMD and formulae needed to transform them were given by, e.g., Bowyer et al. (2000), and Del Zanna et al. (2002) and references therein. We use the definition of the volume emission measure, evaluated in a temperature interval  $2\delta$  around  $T_a$  as in Brickhouse & Dupree (1998), namely,  $EM = \int_{T_a-\delta}^{T_a+\delta} N_e N_H dV$ . The DEM is defined as  $DEM = N_e N_H \frac{dV}{dT}$ . We included another term to account for the temperature grid in a log  $T$  scale:  $\frac{d(\log T)}{dT} = \frac{1}{\ln(10) T}$ . We integrated the DEM in a temperature interval  $\Delta(\log T)$  around a temperature  $T_a$ , assuming that the emission measure is constant in that interval. Then the emission measure (in the EMD definition) relates to DEM as

$$EM = DEM \cdot 4\pi \left(\frac{Rd'}{d}\right)^2 \cdot T_a \cdot \ln 10 \cdot \Delta(\log T), \quad (\text{A.1})$$

where  $\Delta(\log T)$  (K) = 0.1 is the temperature resolution of the ATOMDB models used in our work. Once the DEMs were transformed into EMDs (Fig. A.1), we calculated the predicted line fluxes using the solar coronal abundances assumed in LO17 and DUV21 to test how good are the models provided by those authors. The results of this comparison are shown in Fig. A.2.

The smooth shape imposed by polynomial fits yields large differences with our results, in special in the temperature ranges with fewer spectral lines, such as the regions with  $\log T$ (K) < 4.5, and  $\sim 5.2$ –6.0. DUV21 used solar coronal abundances in all cases, which might explain some of the discrepancies, as acknowledged by DUV21. While this assumption could be a good approximation for a solar-like quiet corona, like that of HD 209458, it is inadequate for a very active star like AU Mic<sup>11</sup>, as shown in Fig. A.2 (see e.g., Sanz-Forcada et al. 2003b). In the case of Barnard’s star, DUV21 made a different DEM for flaring and quiescent stages, while we used only one overall EMD. However none of the DUV21 functions match the minimum of the EMD as sampled by us. Finally, TRAPPIST-1 model also over-interprets the information available in the X-rays spectra by providing a continuous DEM along the high temperature range.

<sup>11</sup> DUV21 DEM was based on a different dataset from ours.

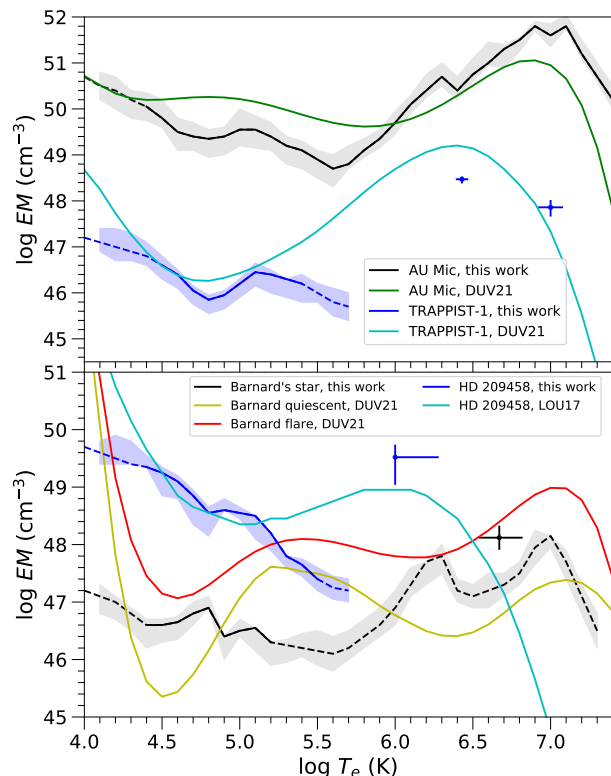


**Fig. A.1.** EMD calculated in our work, with shaded  $1\sigma$  error bands, as compared with those of LOU17 and DUV21. Dashed lines indicate an uncertain EMD despite formal error bands. The results from our global fit to the X-ray spectra are indicated with error bars.

**Table A.1.** Comparison of modeled EUV broadband luminosities<sup>a</sup>.

Reference	AU Mic	TRAPPIST-1	Barnard’s Star (quiescence)	Barnard’s Star (flare)	HD 209458
DUV21, LOU17	28.93	27.33	25.71	26.61	28.20
This work	29.39	26.29		26.13	28.45

**Notes.** <sup>(a)</sup>  $\log L_{\text{EUV,H}}$  ( $\text{erg s}^{-1}$ ) in the 100–912 Å range as reported by DUV21 and LOU17, and compared with our model.

In all cases, there are obvious discrepancies, of up to three orders of magnitude, between predicted and observed line fluxes when the EMDs of DUV21 and LOU17 are employed. Their EUV broadband fluxes differ by up to  $\sim 1$  dex from ours (Table A.1).

### A.2. Comparison with other scaling laws

In this section, we compare the results from our scaling law described in Sect. 4.2 and other works in the literature. Our X-ray vs. EUV<sub>H</sub> luminosity linear fit has an RMS=0.406. Figure A.3 includes a comparison with the SF11 linear fit (RMS=0.411 with the current dataset) to  $L_X$  and  $L_{\text{EUV,H}}$ . The addition of UV high-spectral resolution data and values with larger X-ray luminosity seems to lower the EUV modeled luminosity, but both fits are consistent.

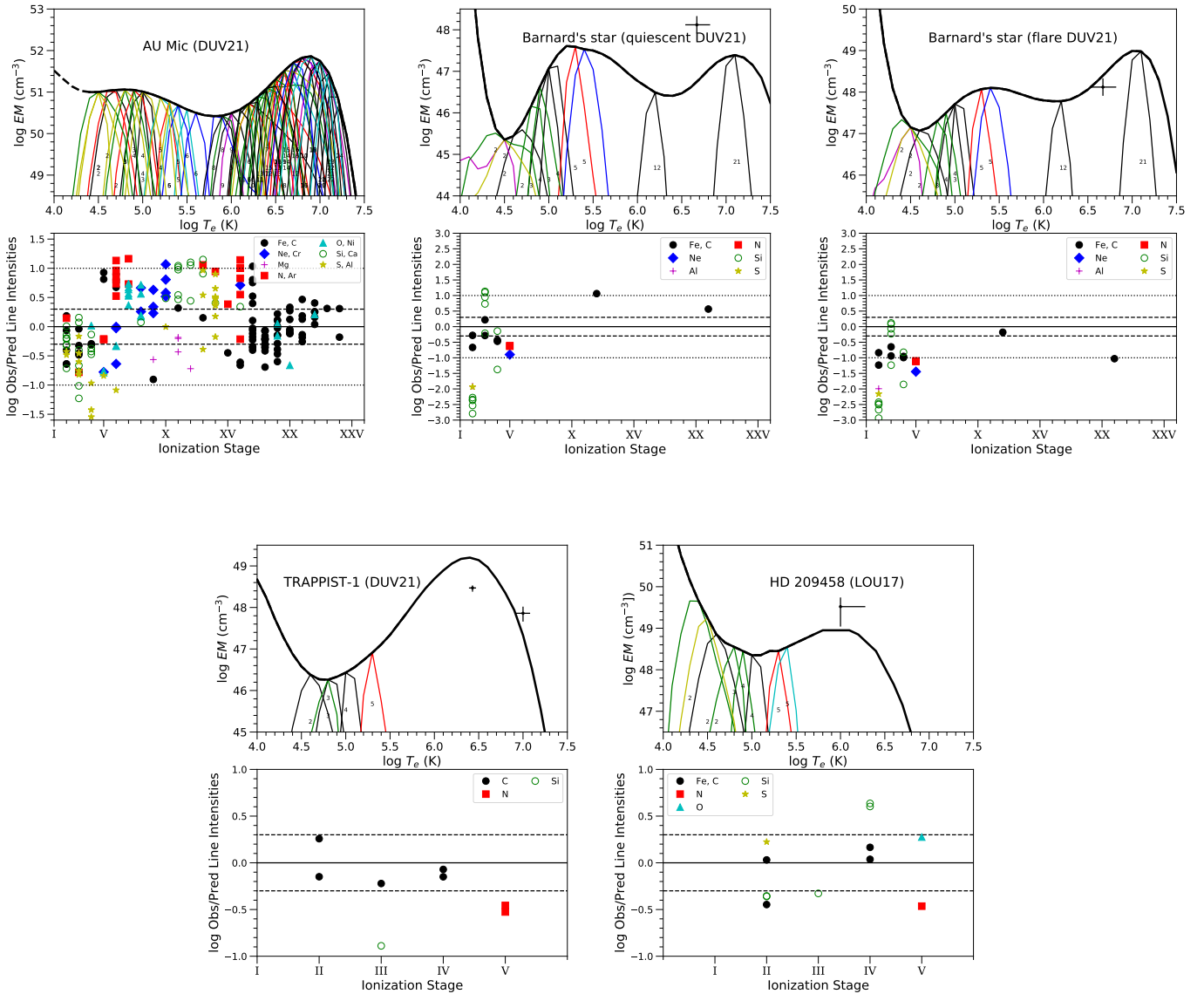


**Fig. A.2.** EMDs calculated from the DEM published in LOU17 and DUV21, using our line fluxes measurements to test the quality of the fit. Symbols and lines as in Fig. 1. In the lower panels the axis range has been adapted to show all available line fluxes ratios. An offset of one order of magnitude is indicated with dotted lines.

Scaling laws based on the surface stellar flux are shown in Fig. A.4 together with our own fit to the data. Our fit is

$$\log F_{\text{EUV,H}} = (0.784 \pm 0.044) C_X + (5.54 \pm 0.05), \quad (\text{A.2})$$

where  $C_X = \log F_X - 4.88$ , all in c.g.s units. The plot includes only the stars of our sample with a stellar radius available in the Extrasolar Planet Encyclopaedia<sup>12</sup> database, 65 stars. Our linear fit to the data shows a Pearson's correlation factor  $r = 0.911$ , and an RMS of 0.386. The Johnstone et al. (2021) relation has an RMS of 0.405 with this dataset, Chadney et al. (2015) an RMS=0.445, and King et al. (2018) an RMS=0.462. The literature fits have a worse RMS than our linear fit between  $\log L_X$  and  $\log L_{\text{EUV,H}}$  (Fig. 3). They also have a dependence on the stellar radius, introducing a new source of uncertainty. We display the literature fits extrapolated to cover our range of values. Although

<sup>12</sup> <https://exoplanet.eu>

all of the fits are roughly consistent with ours, discrepancies arise for the most active stars, and especially for the least active stars.

Poppenhaeger (2022) calculated the EUV flux in the range 200–504 Å based on EUVE observations in a number of targets. This is a spectral range severely affected by ISM absorption (see, e.g., Sanz-Forcada et al. 2003a) and the spectra are contaminated by geocoronal emission around the He II 304 Å line, as those in Johnstone et al. (2021). Since Poppenhaeger (2022) calculated the absorption based on two lines that are absent in most of the spectra, there may be systematic under- or over-estimation in this calculation. Moreover, most lines above ~370 Å are absent in EUVE spectra, and some of the observed lines are actually the second order of stronger bluewards lines. An example is the EUVE spectrum of AD Leo (Sanz-Forcada & Micela 2002), a star at only ~5 pc from us. The low quality spectrum of AD Leo shown in Fig. 9 of Poppenhaeger (2022) came from an auto-

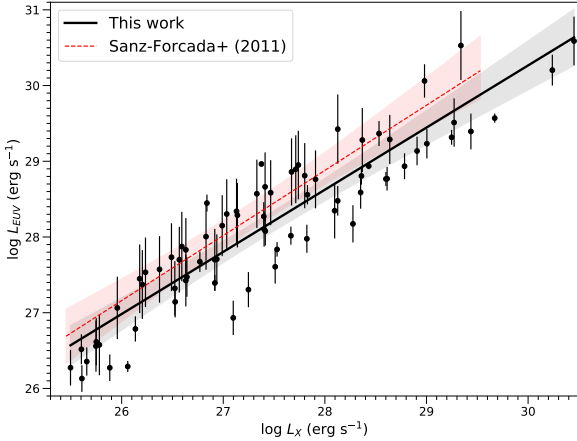


**Fig. A.3.** EUV vs. X-ray flux with our data and the fit by SF11.  $1\sigma$  error bands to both fits, and their original datasets, are displayed in light gray and red respectively.

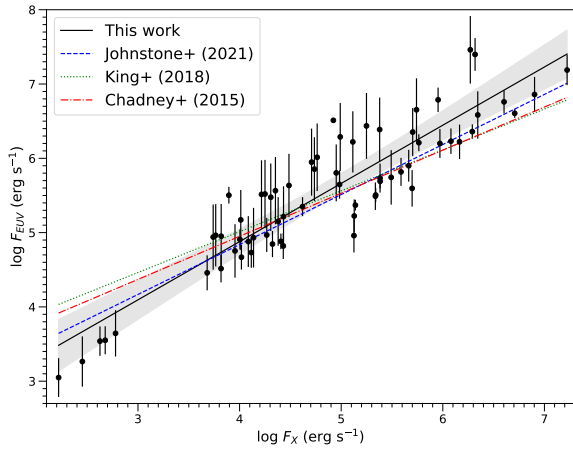


**Fig. A.4.** EUV vs. X-ray surface flux with our data and some literature fits.  $1\sigma$  error bands to our fit is displayed in light gray.

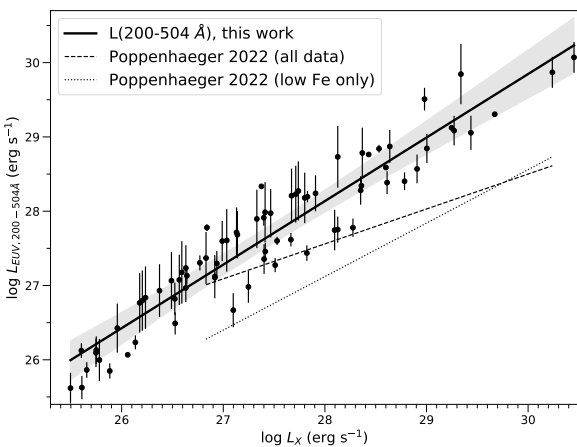


**Fig. A.5.** X-ray vs. EUV (in the range 200–504  $\text{\AA}$ ) luminosity with our data and the fits calculated by Poppenhaeger (2022).  $1\sigma$  error bands to our fit are displayed in light gray.

matic reduction available in HEASARC, quite below the quality level that can be achieved by a customized data reduction, which would anyway be insufficient to accurately calculate the flux in the 200–504  $\text{\AA}$  spectral range. In Fig. A.5 we show the fit that we did to our calculated EUV fluxes in this range, as compared with the Poppenhaeger (2022) fits (their relation was also applied by Fossati et al. 2023). They are obviously discrepant. Our linear fit is

$$\log L_{\text{EUV},200-504\text{\AA}} = (0.855 \pm 0.033) C_X + (27.66 \pm 0.04), \quad (\text{A.3})$$

where  $C_X = \log L_X - 27.44$  in c.g.s. units. This is valid in the range  $\log L_X \sim 25.5 - 30.5$ . This fit has a Pearson’s correlation factor  $r = 0.951$  and an  $\text{RMS} = 0.326$ . The spectral range used to calculate  $L_X$  by Poppenhaeger (2022) was 0.2–5 keV, instead of our 0.12–2.4 keV range. We tested the impact of this difference by measuring the flux in an active (AD Leo) star and a more quiet (GJ 357) star. The flux in the 0.2–5 keV range is  $\sim 4\%$  lower for AD Leo, and  $\sim 0.3$  dex lower for GJ 357, thus increasing the differences between the two relations.

## Appendix B: Relations between He I $\lambda 10830 \text{ \AA}$ equivalent width and XUV flux

In this section, we seek an empirical relationship between the stellar XUV irradiation, measured in the 5–504  $\text{\AA}$  range, and the equivalent width ( $EW$ ) of the He I  $\lambda 10830 \text{ \AA}$  line in the planet atmosphere. The equivalent width,  $EW$ , of an absorbing line over the frequency interval  $\Delta\nu$  in a planetary atmosphere during the primary transit is given by

$$EW \simeq \frac{\int_{\Delta\nu} \mathcal{A}_\nu d\nu}{\pi R_\star^2}, \quad (\text{B.1})$$

where  $\nu$  is the frequency,  $\mathcal{A}_\nu$  is the absorption of the entire planetary atmosphere,  $R_\star$  is the stellar radius, and we assume that  $R_\star^2 \gg R_p^2$ . The absorption  $\mathcal{A}_\nu$  is obtained by integrating the partial absorption of the areas covered by infinitesimal spherical rings over all impact parameter  $b$  values (see, e.g., Sect. 3.3 in Lampón et al. 2020 and Fig. B.1) as:

$$\mathcal{A}_\nu = 2\pi \int_{R_p}^{R_\star} b [1 - \mathcal{T}_\nu(b)] db, \quad (\text{B.2})$$

where we assume spherical symmetry,  $R_p$  is the radius of the planet, TOA is the top of the atmosphere in front of the star, and the transmission  $\mathcal{T}_\nu$  is given by

$$\mathcal{T}_\nu(b) = \exp \left[ - \int_{-\text{TOA}}^{\text{TOA}} k_\nu(x) n(x) dx \right], \quad (\text{B.3})$$

where  $k_\nu$  is the absorption coefficient (also denoted by  $\sigma_\nu(x)$ , the absorption cross section) of the He( $2^3\text{S}$ ) lines and  $n(x)$  is the He( $2^3\text{S}$ ) concentration.

To estimate the dependence of  $EW$  on the different parameters, we considered the two extreme conditions of (a) optically thick, where the transmission near the line center,  $\mathcal{T}_{\nu=\text{He I}}(b)$ , is close to zero, and (b) optically thin, where  $\mathcal{T}_{\nu=\text{He I}}(b)$  is close to unity. This approach in two extreme situations seems reasonable as we know that most gas giant atmospheres have, in general, a narrow (compressed) region at low altitudes with large He( $2^3\text{S}$ ) concentrations, and an extended and slowly decreasing He( $2^3\text{S}$ ) concentration at medium to larger radii (see, e.g., Fig. A.1 in Lampón et al. 2023). The first region can be considered in optically thick conditions while the latter in the optically thin regime.

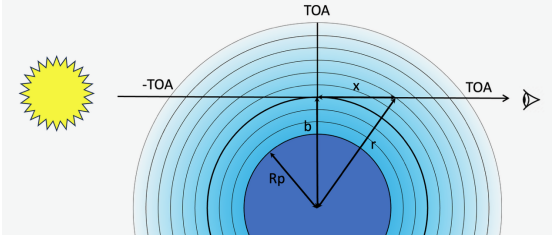


**Fig. B.1.** He( $2^3S$ ) column along the line of sight,  $x$ , at the impact parameter,  $b$ , and distance from the center of the planet,  $r$ .

### B.1. Optically thick

In this case,  $\mathcal{T}(b) \simeq 0$ , the  $EW$  is given by that produced by an opaque ring of height  $H_{\text{He},0}$ . From Eqs. B.1 and B.2, with  $\mathcal{T}(b) \simeq 0$ , we obtain

$$EW_{\text{thick}} \propto \frac{2 R_p H_{\text{He},0}}{R_\star^2}. \quad (\text{B.4})$$

To estimate the extension of the opaque region,  $H_{\text{He},0}$ , it is reasonable to assume that it is proportional to the irradiating XUV flux  $F_{\text{XUV}}$ , as this flux controls the He( $2^3S$ ) concentration that enters into Eq. B.3. In fact, the planets with larger XUV fluxes have larger peaks of He( $2^3S$ ) concentrations (see Fig. A.1 in Lampón et al. 2023). In addition, for a planet with a stronger gravitational potential,  $\Phi_p$ , it is expected that its atmosphere (and the He( $2^3S$ ) concentration) is more compressed and hence  $H_{\text{He},0}$  should be smaller. It is then reasonable that in this optically thick limit we have

$$EW_{\text{thick}} \propto \frac{R_p F_{\text{XUV}}}{R_\star^2 \Phi_p}. \quad (\text{B.5})$$

### B.2. Optically thin

In this case the transmission over the interval  $\Delta\nu$  can be approximated by

$$\mathcal{T}(b) \simeq 1 - \int_{-\text{TOA}}^{\text{TOA}} k(x) n(x) dx = 1 - k m(b), \quad (\text{B.6})$$

where  $m(b) = \int_{-\text{TOA}}^{\text{TOA}} n(x) dx$  is the column density along the line of sight at impact parameter  $b$  (see Fig. B.1) and we have assumed that the absorption coefficient does not depend on  $x$ . Assuming spherical symmetry and changing the integration variable to  $r$ , the distance from the center of the planet, e.g.,  $x = \sqrt{r^2 - b^2}$  and  $dx = \frac{r}{\sqrt{r^2 - b^2}} dr$ , we obtain

$$m(b) = 2 \int_b^{\infty} \frac{n(r) r}{\sqrt{r^2 - b^2}} dr. \quad (\text{B.7})$$

To further evaluate  $m(b)$  and the  $EW$  let us make some assumptions on  $n(r)$ . The He( $2^3S$ ) concentration can be well approximated by

$$n(r) = n_0 (r_0/r)^p, \quad (\text{B.8})$$

where the exponent  $p$  usually takes values between 2 and 5 and  $n_0$  is the He( $2^3S$ ) concentration at  $r_0$  (see, e.g., Fig. A.1(c) in Lampón et al. 2023). Note that the He( $2^3S$ ) peak concentration,

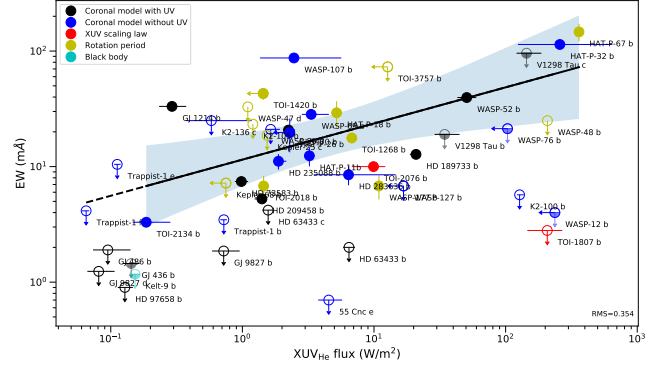


**Fig. B.2.** He I 10830 triplet equivalent width, plotted against  $F_{\text{XUV,He}}$ .  $1\sigma$  error bands to the fit are displayed in light blue. Colors and symbols as in Fig. 4. Pearson's coefficient is  $r = 0.579$

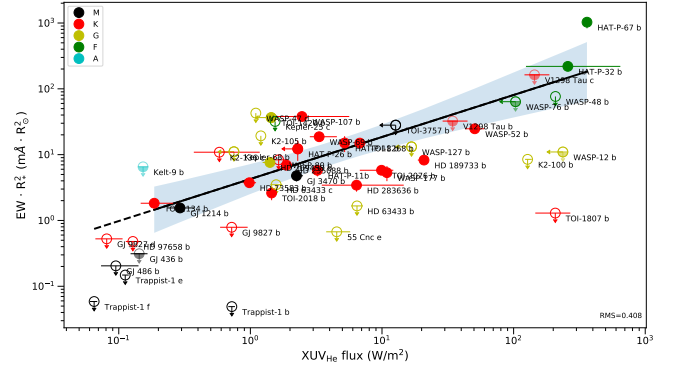


**Fig. B.3.** He I 10830 triplet equivalent width, multiplied by the stellar area, plotted against  $F_{\text{XUV,He}}$ . The color scheme indicates the stellar spectral types, with symbols as in Fig. 4. The fit gives  $r = 0.782$ .

$n_0$ , usually occurs very close to the lower boundary of the atmosphere; hence  $r_0 \simeq R_p$ . Then, we obtain

$$m(b) \simeq 2 n_0 R_p^p \int_b^{\infty} \frac{r^{1-p}}{\sqrt{r^2 - b^2}} dr, \quad (\text{B.9})$$

and, by performing the integral, we obtain

$$m(b) \simeq \sqrt{\pi} n_0 R_p^p \frac{\Gamma((p-1)/2)}{\Gamma(p/2)} b^{1-p}, \quad (\text{B.10})$$

valid for  $p > 1$ , which is amply met in our case.

Including this expression into Eq. B.6, and considering Eqs. B.1 and B.2, we obtain

$$EW \simeq 2 \sqrt{\pi} \frac{\Gamma((p-1)/2)}{\Gamma(p/2)} k n_0 \frac{R_p^p}{R_\star^2} \int_{R_p}^{R_*} b^{2-p} db. \quad (\text{B.11})$$

Performing the integral in Eq. B.11 and considering that  $R_* \gg R_p$ , we find that the integral is independent of  $R_p$  for  $1 < p < 3$ , it is proportional to  $\ln(R_*/R_p)$  for  $p = 3$ , and is proportional to  $R_p^{3-p}$  for  $p > 3$ . Hence, as the  $\Gamma$  functions are constants,

$$EW_{\text{thin}} \propto \frac{1}{R_\star^2} \frac{F_{\text{XUV}}}{\Phi_p} \times \begin{cases} R_p^p & \text{for } 1 < p < 3, \\ R_p^3 \ln(R_*/R_p) & \text{for } p=3, \text{ and} \\ R_p^3 & \text{for } p > 3, \end{cases} \quad (\text{B.12})$$





**Table C.2.** UV observations of stars in the sample<sup>a</sup>.

Star name	Date	Instrument
55 Cnc	2016-04-04–2017-02-14	COS/G130M
AD Leo	2000-03-10, 2002-06-01	STIS/E140M
AD Leo	1993–2000	EUVE <sup>a</sup>
AU Mic	1998-09-06, 2020-07-02	STIS/E140M
AU Mic	2000-08-26, 2001-10-10	FUSE
AU Mic	1993–1996	EUVE
Barnard's star	2019-03-04	COS/G130M+STIS/G140L <sup>b</sup>
GJ 357	2021-04-21	COS/G130M+G160M
GJ 436	2012-06-23, 2015-06-25	COS/G130M+G160M
GJ 486	2022-03-15	STIS/G140L+G140M
GJ 674	2018-04-02	COS/G130M+STIS/G140L
GJ 1214	2012-08-04, 2015-08-20	COS/G130M+G160M
GJ 3470	2017-12-27–2018-12-23	COS/G130M
GJ 9827	2018-08-23–2020-10-10	STIS/G140M
HD 63443	2020-10-29–2022-02-17	STIS/G140M
HD 73583	2021-12-24–2023-03-02	STIS/G140M
HD 97658	2015-02-13	COS/G130M+G160M
HD 149026	2021-07-26, 2022-10-05	STIS/G140L
HD 189733	2009-0916–2017-07-03	COS/G130M <sup>c</sup>
HD 209458	2009-09-15	COS/G130M+G160M <sup>d</sup>
Lalande 21185	2020-01-14	STIS/E140M
Proxima Cen	2019-04-28–2019-07-01	STIS/E140M
Proxima Cen	2003-04-05	FUSE
Proxima Cen	1993-05-21	EUVE
$\tau$ Boo	1999-06-09, 1999-06-26	STIS/G140M
TOI-836	2022-07-28	STIS/G140M+G140L
TRAPPIST-1	2016-09-26–2019-06-07	COS/G130M+G160M
$\nu$ And	2011-11-09	STIS/E140M
WASP-13	2015-04-21	COS/G140L
WASP-52	2021-10-05, 2021-10-07	STIS/G140M+G140L
WASP-77A	2022-02-02	STIS/G140L

**Notes.** <sup>(a)</sup> Fluxes from Sanz-Forcada & Micela (2002). <sup>(b)</sup> STIS fluxes were corrected to match the level of the mean of the fluxes of the C III 1176 Å, Si III 1206 Å, and C II 1335 lines in the COS spectrum. <sup>(c)</sup> Summed spectrum from HSLA (*Hubble* Spectroscopic Legacy Archive), available at [https://archive.stsci.edu/hst/spectral\\_legacy/](https://archive.stsci.edu/hst/spectral_legacy/). <sup>(d)</sup> Fluxes from France et al. (2010).

**Table C.3.** X-ray (5–100 Å), EUV<sub>H</sub> (100–920 Å), and EUV<sub>He</sub> (100–504 Å) luminosities of stars in the sample<sup>a</sup>.

Planet name	SpT	Stellar distance (pc)	$\log L_{\text{bol}}$ (erg s <sup>-1</sup> )	$\log L_X$ (erg s <sup>-1</sup> )	$\log L_{\text{EUV,H}}$ (erg s <sup>-1</sup> )	$\log L_{\text{EUV,He}}$ (erg s <sup>-1</sup> )	$M_p \sin i$ (M <sub>J</sub> )	$a_p$ (au)	$\log F_{\text{XUV,H}}$ (erg s <sup>-1</sup> cm <sup>-2</sup> )	$\log F_{\text{XUV,He}}$ (erg s <sup>-1</sup> cm <sup>-2</sup> )	$\rho \dot{M}_p$ (g <sup>2</sup> s <sup>-1</sup> cm <sup>-3</sup> ) <sup>b</sup>
14 Her b	K0V	17.899±0.010	33.41	26.92	27.70 <sup>+0.44</sup> <sub>-0.38</sub>	27.16 <sup>+0.33</sup> <sub>-0.22</sub>	5.215	2.820	-0.58	-0.99	2.9e+06
14 Her c							7.031	27.000	-2.55	-2.96	3.2e+04
16 Cyg B b	G2V	21.128±0.009	33.68	<26.78	<27.98	<27.45	1.640	1.680	<0.11	<-0.36	(1.4e+07)
2M1207 A b	M8V	64.68±0.50	31.08	<26.16	<27.36	<26.83	5.500	42.000	<-3.29	<-3.78	(5.8e+03)
30 Ari B b <sup>f</sup>	F6V	44.924±0.061	34.20	29.67	29.57 <sup>+0.09</sup> <sub>-0.03</sub>	29.51 <sup>+0.03</sup> <sub>-0.01</sub>	9.880	0.995	2.47	2.45	3.3e+09
47 Uma b	G0V	13.887±0.019	33.78	25.75	26.62 <sup>+0.37</sup> <sub>-0.26</sub>	26.26 <sup>+0.20</sup> <sub>-0.10</sub>	2.530	2.100	-1.42	-1.71	4.2e+05
47 Uma c							0.540	3.600	-1.89	-2.18	1.4e+05
47 Uma d							1.640	11.600	-2.91	-3.20	1.4e+04
51 Peg b	G2IV	15.528±0.019	33.79	<26.66	<27.86	<27.33	0.460	0.052	<3.01	<2.54	(1.1e+10)
55 Cnc b	G8V	12.587±0.006	33.38	26.77	27.67 <sup>+0.15</sup> <sub>-0.12</sub>	27.39 <sup>+0.11</sup> <sub>-0.09</sub>	0.840	0.113	2.17	1.92	1.6e+09
55 Cnc c							0.178	0.237	1.52	1.28	3.8e+08
55 Cnc d							3.840	5.446	-1.20	-1.44	7.1e+05
55 Cnc e							0.027	0.015	3.90	3.66	8.9e+10
55 Cnc f							0.148	0.773	0.50	0.26	3.5e+07
AD Leo b <sup>f</sup>	M3.0V	4.965±0.001	31.96	28.61	28.77 <sup>+0.16</sup> <sub>-0.15</sub>	28.54 <sup>+0.17</sup> <sub>-0.15</sub>	0.073	0.025	4.75	4.64	6.4e+11
AU Mic b	M1.5V	9.714±0.002	32.58	29.44	29.39 <sup>+0.26</sup> <sub>-0.21</sub>	29.25 <sup>+0.26</sup> <sub>-0.18</sub>	0.028	0.070	4.58	4.51	4.2e+11
AU Mic c							0.0456	0.149	4.12	4.05	1.5e+11
AU Mic d							0.0032	0.085	4.41	4.35	2.9e+11
Barnard's star b	M3.5V	1.828±0.0001	31.15	25.61	26.13 <sup>+0.16</sup> <sub>-0.20</sub>	25.74 <sup>+0.19</sup> <sub>-0.15</sub>	0.0012	0.0229	2.07	1.81	1.3e+09
CoRoT-7 b	K0V	159.49±0.25	33.27	28.98	30.06 <sup>+0.28</sup> <sub>-0.16</sub>	29.84 <sup>+0.11</sup> <sub>-0.05</sub>	0.019	0.017	6.16	5.98	1.6e+13
CoRoT-7 c							0.042	0.046	5.30	5.13	2.3e+12
CoRoT-7 d							17.142	0.080	4.82	4.65	7.4e+11
GJ 12 b	M3.0V	12.167±0.004	31.46	25.78	26.58 <sup>+0.43</sup> <sub>-0.37</sub>	26.05 <sup>+0.32</sup> <sub>-0.21</sub>	0.0049	0.066	1.55	1.15	4.0e+08
GJ 86 b	K1V	10.761±0.006	33.18	<27.41	<28.13	<28.44	4.270	0.118	<3.10	<2.52	(1.4e+10)
GJ 317 b	M3V	15.179±0.009	31.93	26.59	27.87 <sup>+0.47</sup> <sub>-0.45</sub>	27.21 <sup>+0.44</sup> <sub>-0.39</sub>	1.753	1.151	0.32	-0.27	2.4e+07
GJ 317 c							1.644	5.230	-0.99	-1.59	1.1e+06
GJ 357 b	M2.5V	9.436±0.002	31.78	25.66	26.36 <sup>+0.12</sup> <sub>-0.25</sub>	25.93 <sup>+0.08</sup> <sub>-0.12</sub>	0.0066	0.033	1.95	1.63	1.0e+09
GJ 357 c							0.012	0.061	1.42	1.10	2.9e+08
GJ 357 d							0.023	0.204	0.37	0.05	2.6e+07
GJ 436 b	M2.5V	9.775±0.003	31.97	26.14	26.79 <sup>+0.14</sup> <sub>-0.20</sub>	26.30 <sup>+0.08</sup> <sub>-0.10</sub>	0.067	0.029	2.50	2.16	3.6e+09
GJ 486 b	M3.5V	8.079±0.002	31.66	25.50	26.27 <sup>+0.25</sup> <sub>-0.22</sub>	25.69 <sup>+0.23</sup> <sub>-0.16</sub>	0.0089	0.017	2.41	1.98	2.9e+09
GJ 674 b	M2.5V	4.553±0.001	31.79	27.67	28.02 <sup>+0.15</sup> <sub>-0.08</sub>	27.76 <sup>+0.10</sup> <sub>-0.03</sub>	0.040	0.039	3.55	3.39	3.9e+10
GJ 806 b	M1.5V	12.064±0.003	32.01	26.23	27.53 <sup>+0.47</sup> <sub>-0.45</sub>	26.87 <sup>+0.43</sup> <sub>-0.38</sub>	0.0060	0.014	3.81	3.21	7.2e+10
GJ 806 c							0.018	0.052	2.67	2.07	5.2e+09
GJ 832 b	M1.5V	4.9671±0.0006	32.04	26.18	27.45 <sup>+0.46</sup> <sub>-0.44</sub>	26.80 <sup>+0.42</sup> <sub>-0.36</sub>	0.740	3.600	-1.09	-1.67	9.1e+05
GJ 876 b	M4V	4.672±0.001	31.69	26.20	27.37 <sup>+0.47</sup> <sub>-0.44</sub>	26.83 <sup>+0.42</sup> <sub>-0.36</sub>	3.534	0.214	1.29	0.81	2.2e+08
GJ 876 c							0.698	0.134	1.70	1.22	5.6e+08
GJ 876 d							0.019	0.021	3.31	2.83	2.3e+10
GJ 876 e							0.042	0.345	0.88	0.39	8.5e+07
GJ 1214 b	M4.5V	14.641±0.015	31.13	25.88	26.27 <sup>+0.21</sup> <sub>-0.14</sub>	25.94 <sup>+0.12</sup> <sub>-0.08</sub>	0.026	0.014	2.67	2.47	5.3e+09
GJ 3470 b	M1.5V	29.394±0.026	32.19	27.53	27.84 <sup>+0.10</sup> <sub>-0.09</sub>	27.66 <sup>+0.06</sup> <sub>-0.04</sub>	0.040	0.036	3.46	3.35	3.2e+10
GJ 9827 b	K6V	29.656±0.018	32.61	26.53	27.14 <sup>+0.24</sup> <sub>-0.17</sub>	26.57 <sup>+0.17</sup> <sub>-0.11</sub>	0.015	0.019	3.25	2.86	2.0e+10
GJ 9827 c							0.0060	0.039	2.61	2.22	4.5e+09
GJ 9827 d							0.011	0.056	2.30	1.91	2.2e+09
GQ Lup b	K7V	154.08±0.71	33.69	30.45	30.59 <sup>+0.37</sup> <sub>-0.28</sub>	30.17 <sup>+0.22</sup> <sub>-0.13</sub>	31.000	32.000	0.17	0.17	1.7e+07
HAT-P-1 b	G0V	160.26±0.26	33.79	<28.17	<29.34	<28.90	0.523	0.056	<4.40	<4.03	(2.8e+11)
HAT-P-11 b	K4V	37.836±0.014	33.01	27.38	28.96 <sup>+0.00</sup> <sub>-0.00</sub>	28.37 <sup>+0.00</sup> <sub>-0.00</sub>	0.074	0.053	4.08	3.51	1.3e+11
HAT-P-11 c							1.595	4.130	0.29	-0.27	2.2e+07
HAT-P-12 b	K4V	142.05±0.20	32.88	<27.95	<29.16	<28.62	0.210	0.038	<4.56	<4.09	(4.1e+11)
HAT-P-32 b	F8V	286.5±1.6	33.90	29.34	30.53 <sup>+0.47</sup> <sub>-0.45</sub>	29.88 <sup>+0.43</sup> <sub>-0.37</sub>	0.750	0.034	6.02	5.47	1.2e+13
HD 4308 b	G5V	22.046±0.010	33.59	<26.15	<27.35	<26.82	0.041	0.118	<1.78	<1.31	(6.8e+08)
HD 20367 b	G0V	26.055±0.020	33.77	29.27	29.51 <sup>+0.38</sup> <sub>-0.26</sub>	29.18 <sup>+0.22</sup> <sub>-0.11</sub>	1.070	1.250	2.06	1.89	1.3e+09
HD 27442 A b	K2IV	18.440±0.034	34.88	26.64	27.47 <sup>+0.32</sup> <sub>-0.20</sub>	27.21 <sup>+0.15</sup> <sub>-0.06</sub>	1.350	1.160	-0.05	-0.26	1.0e+07
HD 46375 A b	K1IV	29.516±0.017	33.40	27.03	28.30 <sup>+0.47</sup> <sub>-0.45</sub>	27.64 <sup>+0.44</sup> <sub>-0.39</sub>	0.230	0.041	3.65	3.06	5.0e+10
HD 49674 b	G5V	42.882±0.037	33.55	27.47	28.58 <sup>+0.45</sup> <sub>-0.41</sub>	28.01 <sup>+0.37</sup> <sub>-0.27</sub>	0.100	0.058	3.64	3.14	4.9e+10
HD 50554 b	F8V	31.066±0.019	33.74	<26.36	<27.54	<27.07	5.160	2.410	<-0.64	<-1.07	(2.6e+06)
HD 52265 b	G0V	29.922±0.018	33.94	26.99	28.15 <sup>+0.43</sup> <sub>-0.37</sub>	27.63 <sup>+0.32</sup> <sub>-0.21</sub>	1.210	0.520	1.30	0.84	2.2e+08
HD 63433 b	G5V	22.381±0.010	33.46	28.78	28.93 <sup>+0.14</sup> <sub>-0.21</sub>	28.52 <sup>+0.10</sup> <sub>-0.11</sub>	<0.068	0.072	4.00	3.81	1.1e+11
HD 63433 c							0.048	0.146	3.39	3.20	2.8e+10



Table C.3. Continued<sup>a</sup>.

Planet name	SpT	Stellar distance (pc)	$\log L_{\text{bol}}$ ( $\text{erg s}^{-1}$ )	$\log L_X$ ( $\text{erg s}^{-1}$ )	$\log L_{\text{EUV,H}}$ ( $\text{erg s}^{-1}$ )	$\log L_{\text{EUV,He}}$ ( $\text{erg s}^{-1}$ )	$M_p \sin i$ ( $M_J$ )	$a_p$ (au)	$\log F_{\text{XUV,H}}$ ( $\text{erg s}^{-1} \text{cm}^{-2}$ )	$\log F_{\text{XUV,He}}$ ( $\text{erg s}^{-1} \text{cm}^{-2}$ )	$\rho \dot{M}_p$ ( $\text{g}^2 \text{s}^{-1} \text{cm}^{-3}$ ) <sup>b</sup>
WASP-39 b	G9V	215.52±0.46	33.38	<28.26	<29.46	<28.95	0.280	0.049	< 4.65	< 4.21	(5.0e+11)
WASP-52 b	K2V	174.52±0.30	33.18	28.53	29.37 <sup>+0.13</sup> <sub>-0.20</sub>	28.92 <sup>+0.06</sup> <sub>-0.05</sub>	0.460	0.027	5.09	4.75	1.4e+12
WASP-69 b	K4V	50.277±0.051	33.11	28.10	28.35 <sup>+0.40</sup> <sub>-0.33</sub>	27.83 <sup>+0.29</sup> <sub>-0.18</sub>	0.260	0.045	3.78	3.52	6.8e+10
WASP-76 b	F7IV	189.0±2.9	34.20	<28.72	<29.88	<29.47	0.920	0.033	< 5.40	< 5.05	(2.8e+12)
WASP-77 A b	G8V	105.71±0.22	33.48	28.13	28.48 <sup>+0.14</sup> <sub>-0.25</sub>	27.89 <sup>+0.12</sup> <sub>-0.16</sub>	1.760	0.024	4.40	4.12	2.8e+11
WASP-80 b	K7V	49.727±0.049	32.53	27.51	27.61 <sup>+0.17</sup> <sub>-0.18</sub>	27.36 <sup>+0.11</sup> <sub>-0.05</sub>	0.554	0.035	3.33	3.22	2.4e+10
WASP-107 b	K7V	64.392±0.124	32.73	27.67	28.86 <sup>+0.46</sup> <sub>-0.43</sub>	28.24 <sup>+0.40</sup> <sub>-0.32</sub>	0.120	0.055	3.95	3.42	1.0e+11
WASP-107 c							0.360	1.829	0.91	0.37	9.1e+07
WASP-127 b	G5V	160.772±0.517	33.84	<28.37	<29.55	<29.08	0.180	0.052	< 4.68	< 4.27	(5.4e+11)
$\beta$ Pic b	A6V	19.635±0.058	34.54	25.75	26.56 <sup>+0.39</sup> <sub>-0.29</sub>	26.16 <sup>+0.23</sup> <sub>-0.12</sub>	11.898	9.930	-2.82	-3.14	1.7e+04
$\beta$ Pic c							8.500	2.680	-1.68	-2.00	2.3e+05
$\epsilon$ Eri b	K2V	3.220±0.001	33.10	28.35	28.59 <sup>+0.21</sup> <sub>-0.22</sub>	28.42 <sup>+0.16</sup> <sub>-0.21</sub>	0.770	3.530	0.24	0.14	2.0e+07
$\iota$ Hor b	G0V	17.358±0.012	33.82	28.91	29.14 <sup>+0.19</sup> <sub>-0.18</sub>	28.66 <sup>+0.23</sup> <sub>-0.16</sub>	2.260	0.925	1.95	1.72	1.0e+09
$\mu$ Ara b	G3IV	15.603±0.022	33.75	<26.22	<27.39	<26.94	1.676	1.500	< -0.38	< -0.79	(4.6e+06)
$\mu$ Ara c							0.033	0.091	< 2.05	< 1.65	(1.3e+09)
$\mu$ Ara d							0.522	0.921	< 0.04	< -0.36	(1.2e+07)
$\mu$ Ara e							1.814	5.235	< -1.47	< -1.87	(3.8e+05)
$\tau$ Boo A b	F7V	15.613±0.027	34.09	29.00	29.23 <sup>+0.14</sup> <sub>-0.25</sub>	28.96 <sup>+0.15</sup> <sub>-0.15</sub>	4.130	0.046	4.66	4.51	5.1e+11
$\nu$ And b	F8V	13.479±0.038	34.11	27.83	28.56 <sup>+0.15</sup> <sub>-0.13</sub>	28.24 <sup>+0.10</sup> <sub>-0.07</sub>	0.620	0.059	3.64	3.39	4.9e+10
$\nu$ And c							1.800	0.861	1.31	1.06	2.3e+08
$\nu$ And d							10.190	2.550	0.37	0.12	2.6e+07
$\nu$ And e							1.059	5.246	-0.26	-0.51	6.2e+06

**Notes.** <sup>(a)</sup> XUV (5–920 or 5–504 Å) fluxes at the planets’ orbits, and mass loss rates assuming the energy-limited approach. <sup>(b)</sup>  $1 M_J \text{Gyr}^{-1} = 6.02 \times 10^{13} \text{g s}^{-1}$ ,  $1 M_{\oplus} \text{Gyr}^{-1} = 1.89 \times 10^{11} \text{g s}^{-1}$ . Mass loss rates based on  $F_{\text{XUV,H}}$  upper limits are expressed in parenthesis. <sup>(c)</sup> Controversial or retracted planet detection.

**Table C.4.** He I 10830 Å triplet equivalent width and XUV (5–504 Å) flux at planet distance.

Planet name	SpT	$R_*$ ( $R_\odot$ )	EW <sup>(a)</sup> (mÅ)	$F_{\text{XUV,He}}$ ( $\text{W m}^{-2}$ )	Model <sup>(b)</sup>	$M_p$ ( $M_J$ )	$R_p$ ( $R_J$ )	$\rho_p$ ( $\text{g cm}^{-3}$ )	References (planet data and He observation)
GJ 436 b	M2.5V	0.464±0.011	<1.4	0.14±0.02	1	0.067±0.001	0.374±0.010	1.595±0.125	Trifonov et al. (2018); Nortmann et al. (2018)
GJ 1214 b	M4.5V	0.216±0.012	33.2±2.8	0.29 <sup>+0.08</sup> <sub>-0.06</sub>	1	0.026±0.001	0.245±0.005	2.179±0.170	Cloutier et al. (2021); Orell-Miquel et al. (2022)
GJ 3470 b	M1.5V	0.48±0.04	20.7±1.3	2.24 <sup>+0.25</sup> <sub>-0.17</sub>	1	0.040±0.004	0.374±0.053	0.940±0.408	Kosiarek et al. (2019); Palte et al. (2020)
HAT-P-11 b	K4V	0.683±0.009	12.4±2.4	3.23±0.02	2	0.074±0.005	0.389±0.005	1.551±0.118	Yee et al. (2018); Allart et al. (2018)
HAT-P-18 b	K2V	0.717±0.026	29.2±7.6	5.2:	4	0.183±0.034	0.947±0.044	0.267±0.062	Knutson et al. (2014); Paragas et al. (2021)
HAT-P-26 b	K1V	0.788±0.043	19.7±6.4	<2.3	2	0.059±0.007	0.570±0.010	0.392±0.052	Hartman et al. (2011); Vissapragada et al. (2022)
HAT-P-32 b	F8V	1.387±0.067	114.0±4.0	258.22 <sup>+383.18</sup> <sub>-133.02</sub>	2	0.750±0.130	1.789±0.025	0.162±0.029	Bonomo et al. (2017); Czesla et al. (2022)
HAT-P-67 b	F5IV	2.65±0.12	147±25	361.0:	4	0.320±0.180	2.164±0.010	0.039±0.022	Gully-Santiago et al. (2024)
HD 73583 b	K4V	0.71±0.02	7.4±0.6	0.98 <sup>+0.11</sup> <sub>-0.10</sub>	1	0.032±0.011	0.249±0.009	2.579±0.904	Barragán et al. (2022); Zhang et al. (2022a)
HD 189733 b	K2V	0.805±0.016	12.8±0.4	20.86 <sup>+1.20</sup> <sub>-1.98</sub>	1	1.154±0.025	1.138±0.077	0.971±0.198	Paredes et al. (2021); Salz et al. (2018)
HD 209458 b	G0V	1.203±0.061	5.3±0.5	1.41 <sup>+0.11</sup> <sub>-0.16</sub>	1	0.685±0.017	1.390±0.018	0.316±0.015	Wang & Ford (2011); Alonso-Floriano et al. (2019)
HD 235088 b	K2V	0.789±0.022	11.1±1.7	1.88 <sup>+0.26</sup> <sub>-0.13</sub>	2	0.022±0.006	0.187±0.018	4.172±1.657	Zhang et al. (2023b); Orell-Miquel et al. (2023)
HD 283636 b	K0V	0.636±0.024	8.5±1.6	6.41 <sup>+8.09</sup> <sub>-2.89</sub>	2	0.025±0.006	0.205±0.027	3.599±1.664	Zhang et al. (2023b)
KELT-9 b	A0V	2.362±0.07	<1.2	0.2:	5	2.880±0.350	1.840±0.040	0.573±0.079	Borsa et al. (2019); Nortmann et al. (2018)
TOI-1268 b	K2V	0.92±0.06	17.7±1.9	6.8:	4	0.303±0.026	0.810±0.050	0.707±0.144	Šubjak et al. (2022); Orell-Miquel et al. (2024)
TOI-1420 b	G6V	0.923±0.024	42.9±5.1	< 1.4	4	0.079±0.012	1.062±0.027	0.082±0.014	Yoshida et al. (2023); Vissapragada et al. (2024)
TOI-2018 b	K4V	0.62±0.01	6.8±1.5	1.4:	4	0.029±0.007	0.203±0.006	4.316±1.062	Dai et al. (2023); Orell-Miquel et al. (2024)
TOI-2076 b	K0	0.761±0.016	10.0±0.7	9.91 <sup>+2.17</sup> <sub>-3.07</sub>	3	0.028: <sup>c</sup>	0.293±0.004	1.383:	Hedges et al. (2021); Zhang et al. (2023b)
TOI-2134 b	K5V	0.744±0.027	3.3±0.3	0.19 <sup>+0.10</sup> <sub>-0.04</sub>	2	0.029±0.002	0.240±0.014	2.575±0.499	Rescigno et al. (2024); Zhang et al. (2023a)
WASP-12 b	G0V	1.657±0.045	<4.0	<236.8:	2	1.460±0.270	1.884±0.057	0.271±0.056	Turner et al. (2021); Czesla et al. (2024)
WASP-52 b	K2V	0.79±0.02	39.6±1.4	50.67 <sup>+8.63</sup> <sub>-7.29</sub>	1	0.460±0.020	1.270±0.030	0.278±0.023	Hébrard et al. (2013); Kirk et al. (2022)
WASP-69 b	K4V	0.813±0.028	28.3±0.9	3.33 <sup>+1.17</sup> <sub>-0.48</sub>	2	0.260±0.017	1.057±0.047	0.273±0.041	Anderson et al. (2014); Nortmann et al. (2018)
WASP-76 b	F7IV-V	1.73±0.04	<21.3	<103.4	2	0.920±0.030	1.830±0.060	0.186±0.019	West et al. (2016); Casasayas-Barris et al. (2021)
WASP-107 b	K7V	0.66±0.02	87.2±7.6	2.46 <sup>+3.12</sup> <sub>-1.09</sub>	2	0.120±0.001	0.940±0.020	0.179±0.012	Anderson et al. (2017); Allart et al. (2019)
WASP-177 b	K2V	0.885±0.046	6.8±1.6	10.9:	4	0.508±0.038	1.580±0.660	0.160±0.201	Turner et al. (2019); Kirk et al. (2022)
V 1298 Tau b	K11V	1.305±0.07	<19.0	34.42 <sup>+9.84</sup> <sub>-5.28</sub>	1	0.64±0.19	0.888±0.032	0.886±0.096	Suárez Mascareño et al. (2021); Orell-Miquel et al. (2024)
V 1298 Tau c	K11V	1.305±0.07	<95.8	144.08 <sup>+41.20</sup> <sub>-22.09</sub>	1	0.062±0.029	0.467±0.021	0.755±0.368	Sikora et al. (2023); Orell-Miquel et al. (2024)
55 Cnc e	G8V	0.98±0.016	<0.7	4.53 <sup>+1.15</sup> <sub>-0.73</sub>	2	0.027±0.001	0.174±0.003	6.396±0.492	Crida et al. (2018); Zhang et al. (2021)
GJ 486 b	M3.5V	0.328±0.011	<1.9	0.10 <sup>+0.05</sup> <sub>-0.02</sub>	1	(944±41)e-5	0.120±0.006	6.809±1.000	Caballero et al. (2022); Masson et al. (2024)
GJ 9827 b	K6V	0.651±0.065	<1.9	0.72 <sup>+0.22</sup> <sub>-0.13</sub>	1	0.015±0.001	0.136±0.005	7.485±1.022	Kosiarek et al. (2021); Carleo et al. (2021)
GJ 9827 d	K6V	0.651±0.065	<1.2	0.08 <sup>+0.02</sup> <sub>-0.01</sub>	1	0.011±0.002	0.174±0.007	2.515±0.540	Kosiarek et al. (2021); Carleo et al. (2021)
HD 63433 b	G5V	0.912±0.034	<2.0	6.46 <sup>+0.65</sup> <sub>-0.59</sub>	1	<0.068: <sup>c</sup>	0.191±0.007	<12.174	Mallorquín et al. (2023); Zhang et al. (2022b)
HD 63433 c	G5V	0.912±0.034	<4.2	1.57 <sup>+0.16</sup> <sub>-0.14</sub>	1	0.048±0.013	0.243±0.009	4.181±1.220	Mallorquín et al. (2023); Zhang et al. (2022b)
HD 97658 b	K1V	0.73±0.02	<0.9	0.13 <sup>+0.02</sup> <sub>-0.01</sub>	1	0.025±0.002	0.200±0.009	3.782±0.558	Van Grootel et al. (2014); Kasper et al. (2020)
K2-100 b	G0V	1.22±0.02	<5.7	127.72 <sup>+8.54</sup> <sub>-4.41</sub>	2	0.069±0.019	0.346±0.014	2.054±0.635	Barragán et al. (2019); Gaidos et al. (2020)
K2-105 b	G8V	0.91±0.01	<23.3	1.2:	4	0.094±0.060	0.301±0.011	4.275±2.768	Narita et al. (2017); Zhang et al. (2023b)
K2-136 c	K5V	0.66±0.02	<25.0	0.58 <sup>+0.59</sup> <sub>-0.21</sub>	2	0.022: <sup>c</sup>	0.260±0.010	1.552:	Mann et al. (2018); Gaidos et al. (2021)
Kepler-25 c	F6V	1.31±0.02	<18.6	1.5:	4	0.048±0.004	0.465±0.006	0.591±0.060	Mills et al. (2019); Zhang et al. (2023b)
Kepler-68 b	G1V	1.24±0.02	<7.2	< 0.8	4	0.024±0.004	0.206±0.065	3.415±3.287	Mills et al. (2019); Zhang et al. (2023b)
TOI-1807 b	K3V	0.68±0.015	<2.8	207.30±59.90	3	0.008±0.002	0.122±0.009	5.498±1.630	Nardiello et al. (2022); Masson et al. (2024)
TOI-3757 b	M0V	0.62±0.01	<73.0	< 12.7	4	0.268±0.028	1.071±0.040	0.271±0.041	Kanodia et al. (2022)
TRAPPIST-1 b	M8V	0.119±0.001	<3.5	0.72 <sup>+0.03</sup> <sub>-0.04</sub>	2	(43.2±2.2)e-4	0.100±0.001	5.429±0.336	Agol et al. (2021); Krishnamurthy et al. (2021)
TRAPPIST-1 e	M8V	0.119±0.001	<10.5	0.11±0.01	2	(218±7)e-5	0.082±0.001	4.889±0.264	Agol et al. (2021); Krishnamurthy et al. (2021)
TRAPPIST-1 f	M8V	0.119±0.001	<4.1	0.07±0.00	2	(327±10)e-5	0.093±0.001	5.004±0.244	Agol et al. (2021); Krishnamurthy et al. (2021)
WASP-47 d	G9V	1.14±0.01	<32.9	1.1:	4	0.041±0.005	0.319±0.004	1.575±0.190	Vanderburg et al. (2017); Zhang et al. (2023b)
WASP-48 b	F8IV	1.75±0.09	<25	207.9:	4	0.984±0.085	1.670±0.100	0.262±0.052	Enoch et al. (2011); Bennett et al. (2023)
WASP-80 b	K7V	0.63±0.15	<21	1.64 <sup>+0.27</sup> <sub>-0.14</sub>	2	0.554±0.040	0.952±0.027	0.796±0.089	Triaud et al. (2013); Fossati et al. (2022)
WASP-127 b	G5V	1.39±0.03	<6.8	< 16.8	2	0.180±0.020	1.370±0.040	0.087±0.012	Lam et al. (2017); dos Santos et al. (2020)

**Notes.** <sup>(a)</sup> Equivalent width of the net transmission planetary signal. <sup>(b)</sup> Model employed to calculate XUV flux (see text): coronal model with (1) and without (2) UV data; X vs. EUV relation (3); X-rays vs  $P_{\text{rot}}$  relation (4); and blackbody emission (5). <sup>(c)</sup> No error bars associated with the mass are used in the plot of these objects.

Appendix D: Spectral fits, line fluxes and emission measure distribution

Table D.1. Low-resolution X-ray spectral fits<sup>a</sup>.

Star	$\log N_{\text{H}}$ ( $\text{cm}^{-2}$ )	$\log T$ (K)	$\log EM$ ( $\text{cm}^{-3}$ )	Elements (X)	[X/H]
14 Her	18.3	$6.50^{+0.05}_{-0.06}$	$49.52^{+0.09}_{-0.13}$	Fe	$-0.22^{+0.12}_{-0.00}$
16 Cyg B	18.3	$6.30^{+0.00}_{-0.00}$	$49.32^{+0.23}_{-0.54}$	Fe	-0.20
2M 1207 A	19.0	$6.30^{+0.00}_{-0.00}$	$48.70^{+0.28}_{-0.00}$	Fe	-0.20
30 Ari B	18.7	$6.67^{+0.02}_{-0.02}, 6.23^{+0.16}_{-0.08}, 6.93^{+0.01}_{-0.01}$	$51.91^{+0.04}_{-0.04}, 51.33^{+0.14}_{-0.18}, 51.79^{+0.03}_{-0.03}$	Fe, O, Ne	$-0.06^{+0.03}_{-0.03}, -0.34^{+0.06}_{-0.08}, 0.03^{+0.06}_{-0.07}$
47 UMa	18.3	$6.25^{+0.14}_{-0.25}$	$48.32^{+0.21}_{-0.47}$	Fe	$-0.30^{+0.20}_{-0.00}$
51 Peg	18.3	$6.30^{+0.00}_{-0.00}$	$49.20^{+0.24}_{-0.59}$	Fe	-0.20
55 Cnc	18.3	$6.56^{+0.04}_{-0.05}$	$49.61^{+0.08}_{-0.10}$	Fe, O	$-0.53^{+0.28}_{-0.33}, -0.80^{+0.32}_{-1.05}$
Barnard's star	18.0	$6.67^{+0.15}_{-0.13}$	$48.12^{+0.21}_{-0.21}$	Fe	0.00
Corot 7	20.0	$6.03^{+0.45}_{-0.03}$	$51.60^{+0.37}_{-1.34}$	Fe	0.03
GJ 12	18.5	$6.44^{+0.12}_{-0.11}$	$48.39^{+0.14}_{-0.19}$	Fe	-0.50
GJ 86	18.3	$6.56^{+0.03}_{-0.03}$	$50.04^{+0.07}_{-0.09}$	Fe, O, Ne	$-0.27^{+0.15}_{-0.14}, -0.03^{+0.10}_{-0.10}, -0.04^{+0.18}_{-0.20}$
GJ 317	18.0	$6.60^{+0.10}_{-0.06}$	$49.24^{+0.13}_{-0.14}$	Fe	$-0.34^{+0.36}_{-0.49}$
GJ 357	18.3	$6.47^{+0.04}_{-0.05}$	$48.22^{+0.08}_{-0.10}$	Fe	-0.10
GJ 436	18.0	$6.41^{+0.08}_{-0.08}, 6.94^{+0.22}_{-0.14}$	$48.55^{+0.11}_{-0.11}, 48.23^{+0.15}_{-0.40}$	Fe	$-0.29^{+0.19}_{-0.01}$
GJ 486	18.0	$6.67^{+0.40}_{-0.09}$	$48.07^{+0.07}_{-0.16}$	Fe	-0.15
GJ 806	18.5	$6.58^{+0.10}_{-0.09}$	$48.90^{+0.10}_{-0.12}$	Fe	-0.45
GJ 832	18.0	$6.52^{+0.04}_{-0.05}$	$48.81^{+0.07}_{-0.10}$	Fe	$-0.36^{+0.37}_{-0.38}$
GJ 876	18.0	$6.90^{+0.77}_{-0.19}, 6.53^{+0.05}_{-0.04}$	$48.19^{+0.38}_{-0.94}, 48.89^{+0.11}_{-0.11}$	Fe, O, Ne	$-0.50^{+0.15}_{-0.15}, -0.34^{+0.12}_{-0.13}, -0.09^{+0.19}_{-0.22}$
GJ 1214	18.5	$6.61^{+1.14}_{-0.15}$	$48.20^{+0.19}_{-0.34}$	Fe	0.39
GJ 3470	18.5	$7.05^{+0.62}_{-0.11}, 6.47^{+0.06}_{-0.07}$	$49.29^{+0.13}_{-0.18}, 49.89^{+0.07}_{-0.10}$	Fe	0.20
GJ 9827	18.5	$6.60^{+0.08}_{-0.06}$	$49.16^{+0.08}_{-0.10}$	Fe	-0.28
QQ Lup	21.8	$6.57^{+0.12}_{-0.11}, 7.52^{+0.10}_{-0.08}$	$52.98^{+0.55}_{-0.54}, 52.89^{+0.06}_{-0.07}$	Fe, Ne	$-0.77^{+0.36}_{-1.51}, 0.16^{+0.29}_{-0.24}$
HAT-P 1	21.0	$6.30^{+0.00}_{-0.00}$	$50.63^{+0.36}_{-N/A}$	Fe	0.13
HAT-P 11	18.7	$6.41^{+0.05}_{-0.03}, 7.06^{+0.22}_{-0.20}$	$49.75^{+0.08}_{-0.10}, 48.80^{+0.27}_{-0.88}$	Fe	0.30
HAT-P 12	20.0	$6.30^{+0.00}_{-0.00}$	$50.51^{+0.36}_{-N/A}$	Fe	-0.29
HAT-P 32	21.1	$6.61^{+0.09}_{-0.07}$	$51.89^{+0.10}_{-0.11}$	Fe	-0.04
HD 4308	18.3	$6.30^{+0.00}_{-0.00}$	$48.69^{+0.23}_{-0.54}$	Fe	-0.20
HD 20367	18.7	$6.67^{+0.06}_{-0.02}, 6.30^{+0.17}_{-0.15}, 6.98^{+0.02}_{-0.02}$	$51.61^{+0.05}_{-0.12}, 50.85^{+0.36}_{-0.21}, 51.36^{+0.05}_{-0.07}$	Fe, O, Ne	$-0.09^{+0.04}_{-0.04}, -0.26^{+0.09}_{-0.07}, -0.22^{+0.16}_{-0.27}$
HD 27442	18.3	$6.33^{+0.04}_{-0.04}$	$49.09^{+0.08}_{-0.09}$	Fe	0.20
HD 46375	18.7	$6.61^{+0.14}_{-0.11}$	$49.67^{+0.09}_{-0.17}$	Fe	$-0.30^{+0.20}_{-0.00}$
HD 49674	18.8	$6.50^{+0.06}_{-0.05}$	$49.92^{+0.09}_{-0.11}$	Fe	0.25
HD 50554	18.5	$6.30^{+0.00}_{-0.00}$	$48.86^{+0.20}_{-0.38}$	Fe	0.00
HD 52265	18.3	$6.40^{+0.06}_{-0.04}$	$49.46^{+0.13}_{-0.16}$	Fe	0.20
HD 63433	18.3	$6.93^{+0.05}_{-0.06}, 6.64^{+0.05}_{-0.06}$	$51.03^{+0.18}_{-0.16}, 51.11^{+0.12}_{-0.21}$	Fe, O	$-0.18^{+0.09}_{-0.08}, -0.14^{+0.14}_{-0.14}$
HD 70642	18.5	$6.49^{+0.14}_{-0.10}$	$48.92^{+0.17}_{-0.27}$	Fe	0.00
HD 73583	18.7	$6.64^{+0.05}_{-0.06}$	$50.54^{+0.07}_{-0.08}$	Fe	$-0.66^{+0.24}_{-0.33}$
HD 75289	18.7	$6.23^{+0.21}_{-0.23}$	$48.00^{+0.42}_{-0.81}$	Fe	0.30
HD 93083	18.5	$6.50^{+0.07}_{-0.05}$	$49.35^{+0.10}_{-0.12}$	Fe	0.10
HD 95089	20.5	$6.30^{+0.00}_{-0.00}$	$49.14^{+1.57}_{-N/A}$	Fe	-0.20
HD 97658	18.0	$6.92^{+0.26}_{-0.19}, 6.40^{+0.04}_{-0.07}$	$48.76^{+0.24}_{-0.48}, 49.39^{+0.08}_{-0.09}$	Fe	-0.23
HD 99492	18.3	$6.51^{+0.05}_{-0.03}$	$49.04^{+0.07}_{-0.09}$	Fe	0.20
HD 101930	18.7	$6.30^{+0.00}_{-0.00}$	$48.54^{+0.43}_{-N/A}$	Fe	-0.20
HD 102195	18.5	$6.45^{+0.05}_{-0.06}, 6.84^{+0.04}_{-0.04}$	$50.80^{+0.07}_{-0.08}, 50.62^{+0.10}_{-0.13}$	Fe, O	$-0.17^{+0.10}_{-0.10}, -0.45^{+0.10}_{-0.11}$
HD 108147	18.7	$6.67^{+0.15}_{-0.10}, 6.38^{+0.10}_{-0.11}$	$50.02^{+0.26}_{-0.65}, 50.05^{+0.21}_{-0.46}$	Fe	$0.19^{+0.20}_{-0.14}$
HD 111232	18.7	$6.30^{+0.00}_{-0.00}$	$49.05^{+0.08}_{-0.00}$	Fe	-0.20
HD 114386	18.7	$6.38^{+0.24}_{-0.23}$	$49.17^{+0.21}_{-0.35}$	Fe	$-0.10^{+0.00}_{-0.20}$
HD 114762	18.7	$6.30^{+0.00}_{-0.00}$	$49.25^{+0.34}_{-N/A}$	Fe	-0.20
HD 114783	18.3	$6.37^{+0.13}_{-0.15}$	$49.09^{+0.21}_{-0.45}$	Fe	$-0.30^{+0.20}_{-0.00}$
HD 130322	18.7	$6.54^{+0.09}_{-0.07}$	$49.93^{+0.11}_{-0.13}$	Fe	$-0.18^{+0.09}_{-0.12}$
HD 149026	20.0	$6.94^{+0.10}_{-0.44}$	$49.59^{+0.13}_{-0.18}$	Fe	0.36
HD 154345	18.3	$6.43^{+0.05}_{-0.05}$	$49.68^{+0.08}_{-0.10}$	Fe	-0.10
HD 164922	18.3	$6.30^{+0.00}_{-0.00}$	$48.01^{+0.55}_{-N/A}$	Fe	0.00
HD 179949	18.7	$6.53^{+0.04}_{-0.05}, 6.25^{+0.10}_{-0.08}, 6.82^{+0.02}_{-0.01}$	$50.79^{+0.06}_{-0.21}, 50.70^{+0.09}_{-0.12}, 50.79^{+0.05}_{-0.06}$	Fe, O, Ne	$-0.08^{+0.02}_{-0.02}, -0.46^{+0.07}_{-0.05}, -0.15^{+0.06}_{-0.07}$
HD 187123	18.8	$6.30^{+0.00}_{-0.00}$	$49.78^{+0.00}_{-0.00}$	Fe	0.00
HD 189733	18.3	$7.30^{+0.00}_{-0.00}, 6.44^{+0.01}_{-0.01}, 6.88^{+0.01}_{-0.01}$	$50.58^{+0.01}_{-0.01}, 50.61^{+0.03}_{-0.03}, 50.80^{+0.04}_{-0.04}$	Fe, O, Ne, Mg, Si	$-0.51^{+0.03}_{-0.03}, -0.27^{+0.01}_{-0.01}, -0.28^{+0.06}_{-0.07}, -0.27^{+0.05}_{-0.06}, -0.19^{+0.05}_{-0.05}$
HD 190360	18.3	$6.30^{+0.00}_{-0.00}$	$49.04^{+0.08}_{-0.19}$	Fe	0.00
HD 195019	18.3	$6.30^{+0.00}_{-0.00}$	$48.83^{+0.00}_{-0.56}$	Fe	0.00
HD 201585	20.8	$6.30^{+0.00}_{-0.00}$	$51.12^{+0.25}_{-0.63}$	Fe	0.00

**Table D.1.** (continued) Low-resolution X-ray spectral fits<sup>a</sup>.

Star	$\log N_{\text{H}}$ ( $\text{cm}^{-2}$ )	$\log T$ (K)	$\log EM$ ( $\text{cm}^{-3}$ )	Elements (X)	[X/H]
HD 209458	18.7	$6.00^{+0.28}_{-0.00}$	$49.52^{+0.22}_{-0.48}$	Fe	-0.20
HD 216435	18.5	$6.58^{+0.05}_{-0.05}$	$50.31^{+0.70}_{-0.09}$	Fe	$-0.08^{+0.08}_{-0.22}$
HD 216437	18.3	$6.40^{+0.15}_{-0.11}$	$49.16^{+0.20}_{-0.38}$	Fe	0.00
HD 217107	18.7	$6.30^{+0.00}_{-0.00}$	$48.25^{+0.20}_{-0.32}$	Fe	0.00
HD 218566	18.7	$6.48^{+0.09}_{-0.08}$	$49.62^{+0.12}_{-0.17}$	Fe	0.20
HD 235088	19.0	$6.87^{+0.07}_{-0.09}$ , $6.53^{+0.14}_{-0.13}$	$50.64^{+0.18}_{-0.40}$ , $50.44^{+0.32}_{-0.31}$	Fe, Ne	$-0.24^{+0.17}_{-0.17}$ , $0.17^{+0.29}_{-0.69}$
HD 283636	19.0	$6.56^{+0.09}_{-0.07}$	$50.25^{+0.09}_{-0.12}$	Fe	0.00
HD 330075	18.7	$6.50^{+0.00}_{-0.00}$	$49.09^{+0.27}_{-0.87}$	Fe	-0.20
HR 8799	18.5	$6.55^{+0.06}_{-0.06}$	$50.79^{+0.07}_{-0.09}$	Fe	-0.50
K2 100	20.0	$6.84^{+0.03}_{-0.04}$ , $6.33^{+0.12}_{-0.18}$	$51.35^{+0.19}_{-0.20}$ , $51.11^{+0.11}_{-0.16}$	Fe, Ne	$0.22^{+0.19}_{-0.19}$ , $0.60^{+0.17}_{-0.31}$
K2 136	19.0	$7.01^{+0.08}_{-0.08}$ , $6.46^{+0.09}_{-0.07}$	$49.87^{+0.22}_{-0.28}$ , $50.15^{+0.11}_{-0.11}$	Fe	$-0.04^{+0.27}_{-0.29}$
Kelt 7	20.0	$6.80^{+0.28}_{-0.17}$ , $6.33^{+0.37}_{-0.27}$	$50.70^{+0.21}_{-0.85}$ , $50.57^{+0.37}_{-0.50}$	Fe	0.24
Kelt 8	21.1	$6.30^{+0.00}_{-0.00}$	$51.67^{+0.30}_{-0.24}$	Fe	0.27
Kelt 9	22.1	$6.30^{+0.00}_{-0.00}$	$52.00^{+0.80}_{-N/A}$	Fe	0.00
NGC 2423 3	21.6	$7.10^{+0.00}_{-0.00}$	$52.48^{+0.38}_{-N/A}$	Fe	0.00
Pollux	18.0	$6.23^{+0.05}_{-0.11}$ , $6.64^{+0.17}_{-0.11}$	$49.86^{+0.06}_{-0.08}$ , $48.60^{+0.59}_{-0.30}$	Fe, O	$0.20^{+0.43}_{-0.30}$ , $-0.29^{+0.23}_{-0.13}$
Teegarden's star	18.0	$6.77^{+0.10}_{-0.06}$ , $6.10^{+0.11}_{-0.08}$	$48.37^{+0.07}_{-0.19}$ , $48.39^{+0.24}_{-0.21}$	Fe	$-0.89^{+0.20}_{-0.26}$
TOI-836	18.7	$6.57^{+0.07}_{-0.05}$	$50.04^{+0.08}_{-0.09}$	Fe	-0.30
TOI-2134	18.5	$6.40^{+0.05}_{-0.04}$	$49.43^{+0.09}_{-0.11}$	Fe	0.12
TRAPPIST-1	18.0	$6.43^{+0.04}_{-0.04}$ , $7.00^{+0.08}_{-0.08}$	$48.47^{+0.06}_{-0.09}$ , $47.86^{+0.16}_{-0.20}$	Fe	0.04
WASP 12	21.3	$6.30^{+0.00}_{-0.00}$	$51.20^{+1.04}_{-N/A}$	Fe	0.30
WASP 13	20.1	$6.30^{+0.00}_{-0.00}$	$50.93^{+0.22}_{-0.49}$	Fe	0.00
WASP 39	20.7	$6.30^{+0.00}_{-0.00}$	$50.79^{+0.50}_{-N/A}$	Fe	-0.12
WASP 52	20.6	$6.55^{+1.06}_{-0.29}$	$51.13^{+0.33}_{-0.63}$	Fe	-0.19
WASP 69	18.5	$6.73^{+0.03}_{-0.04}$	$50.80^{+0.04}_{-0.95}$	Fe	$-0.56^{+0.11}_{-0.12}$
WASP 76	20.3	$6.30^{+0.00}_{-0.00}$	$51.15^{+0.16}_{-1.52}$	Fe	0.23
WASP 77A	20.5	$6.94^{+0.12}_{-0.47}$	$50.57^{+0.16}_{-0.25}$	Fe	0.00
WASP 80	18.6	$6.47^{+0.08}_{-0.09}$ , $6.96^{+0.08}_{-0.08}$	$49.83^{+0.15}_{-0.21}$ , $49.70^{+0.15}_{-0.25}$	Fe	-0.14
WASP 107	20.3	$6.52^{+0.05}_{-0.05}$	$50.21^{+0.10}_{-0.08}$	Fe	0.02
WASP 127	20.7	$6.30^{+0.00}_{-0.00}$	$50.87^{+0.33}_{-N/A}$	Fe	0.00
$\beta$ Pic	18.7	$6.35^{+0.07}_{-0.08}$	$48.30^{+0.12}_{-0.16}$	Fe	-0.20
$\mu$ Ara	18.3	$6.30^{+0.00}_{-0.00}$	$48.69^{+0.20}_{-0.39}$	Fe	0.10
$\nu$ And	18.7	$6.80^{+0.07}_{-0.19}$ , $6.46^{+0.03}_{-0.06}$	$49.23^{+1.08}_{-0.52}$ , $50.22^{+0.10}_{-0.14}$	Fe, O	$0.24^{+0.12}_{-0.12}$ , $0.03^{+0.12}_{-0.11}$

**Notes.** <sup>(a)</sup> Spectral fits of stars with no X-rays coronal lines in the sample (including stars from SF11). Element abundances and FIP are based on solar photospheric values by Anders & Grevesse (1989). Abundances with no error bars are set based on photospheric abundances.

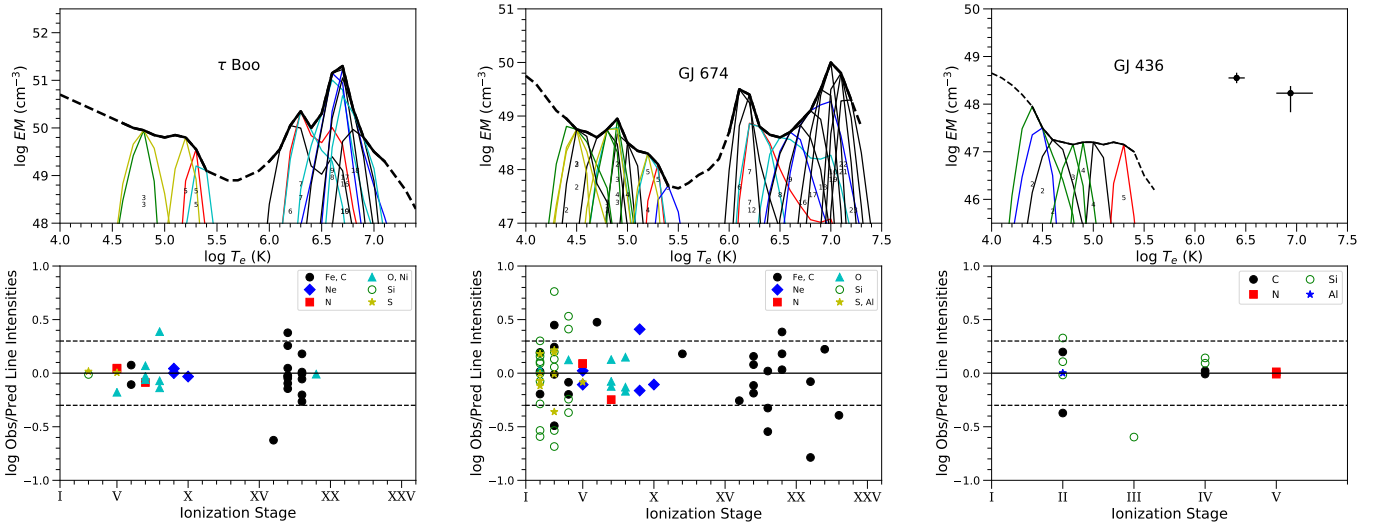


**Fig. D.1.** Emission Measure Distributions as in Fig. 1. *left:*  $\tau$  Boo EMD combining data from XMM-Newton (Maggio et al. 2011), and HST/STIS. *center:* GJ 674 combining data from XMM-Newton and HST/STIS and COS. *right:* GJ 436 using HST/COS data. The 2- $T$  global fit to XMM-Newton/EPIC spectra is also indicated with error bars.



**Table D.2.** *XMM-Newton*/RGS, EUVE, FUSE, and HST/STIS line fluxes of Proxima Centauri<sup>a</sup>.

Ion	$\lambda_{\text{model}}$ (Å)	$\log T_{\text{max}}$	$F_{\text{obs}}$	$S/N$	Ratio	Blends
Si xiv	6.1804	7.3	5.30e-14	10.8	-0.14	Si xiv 6.1858
Si xiii	6.6479	7.1	6.43e-14	16.1	-0.59	Si xiii 6.6882, 6.7403
Mg xii	7.1058	7.1	2.85e-14	12.4	0.20	Mg xii 7.1069, Al xiii 7.1710, 7.1764
Fe xxi	8.0904	7.2	5.64e-15	6.7	0.59	Mg x 8.0696, 8.0701
Fe xxiv	8.2326	7.4	2.08e-15	4.1	0.10	Fe xxi 8.1684, 8.1684, Ni xxi 8.2329, Ni xiii 8.2685, Fe xxiv 8.2850
Mg xii	8.4192	7.1	4.75e-14	20.0	-0.09	Mg xii 8.4246
Mg xi	9.1687	6.9	6.22e-14	25.0	0.05	
Mg xi	9.2312	6.9	1.43e-14	12.1	-0.10	Mg xi 9.2282, Ne x 9.2461, 9.2912, 9.2913, Ni xix 9.2540,
Mg xi	9.3143	6.9	3.51e-14	19.2	0.03	Ne x 9.3616
Ne x	9.4807	6.9	2.42e-14	16.3	0.44	Ne x 9.4809
Ne x	9.7080	6.9	2.55e-14	17.3	0.05	Ne x 9.7085
Na xi	10.0232	7.0	3.04e-14	19.4	0.01	Na xi 10.0286
Fe xvii	10.1210	6.9	9.71e-15	11.1	0.26	Ni xix 10.1100, Fe xix 10.1195, 10.1419
Ne x	10.2385	6.9	5.21e-14	26.0	-0.04	Ne x 10.2396
Fe xvii	10.5040	6.9	1.75e-14	15.6	0.56	
Fe xviii	10.5364	7.0	3.43e-15	6.9	-0.00	
Fe xix	10.6193	7.1	3.71e-14	22.9	0.15	Fe xix 10.6001, 10.6116, 10.6840, Fe xxiv 10.6190, 10.6630, Ne ix 10.6426, Fe xvii 10.6570
Fe xvii	10.7700	6.9	1.93e-14	16.7	0.18	Ne ix 10.7650
Fe xix	10.8160	7.1	7.97e-15	10.8	0.14	Fe xix 10.8083
Fe xxiii	10.9810	7.3	1.60e-14	15.4	-0.02	
Ne ix	11.0010	6.7	2.96e-14	21.1	-0.15	Fe xxiii 10.9810, 10.9810, 11.0190, Fe xvii 11.0260, Fe xxiv 11.0290
Fe xvii	11.1310	6.9	1.21e-14	13.6	-0.01	
Fe xxiv	11.1760	7.4	9.15e-15	11.9	0.09	Fe xxiv 11.1870
Fe xvii	11.2540	6.9	2.27e-14	18.8	0.07	Fe xxiv 11.2680
Fe xviii	11.4230	7.0	1.54e-14	15.7	-0.16	Fe xxii 11.4270, Fe xviii 11.4274, Fe xxiv 11.4320, Fe xxiii 11.4580
Ne ix	11.5440	6.7	3.76e-14	24.7	-0.12	Fe xviii 11.5270, 11.5270
Fe xxiii	11.7360	7.3	2.74e-14	21.2	-0.11	
Fe xxii	11.7700	7.2	2.16e-14	18.9	-0.42	Fe xxiii 11.7360, 11.7360
Ni xx	11.8320	7.1	1.57e-14	16.2	0.16	Fe xxii 11.8020, Ni xx 11.8460
Fe xxii	11.9770	7.2	1.24e-14	14.6	-0.14	Fe xxii 11.8810, 11.9320, 11.9474, Fe xxi 11.9023, 11.9750, Ni xx 11.9617
Fe xviii	12.0827	7.0	8.54e-15	12.2	0.53	Ni xx 12.0787, 12.0879, Fe xxii 12.0928, Ne ix 12.0960
Ne x	12.1321	6.9	2.67e-13	68.6	-0.19	Fe xvii 12.1240, Ne x 12.1375
Fe xxii	12.2100	7.2	9.26e-15	12.8	0.27	Fe xxi 12.2040, Ni xxi 12.2080, Fe xix 12.2120
Fe xxi	12.2840	7.2	6.88e-14	35.1	-0.01	Fe xvii 12.2660
Ni xix	12.4350	7.0	3.16e-14	24.0	-0.09	Fe xxi 12.3930, Fe xx 12.4234, 12.4310
Fe xvi	12.5399	6.8	3.00e-14	23.5	0.20	Fe xxi 12.4990, 12.5048, Fe xx 12.5260, 12.5760, 12.5760, Fe xvii 12.5391
Ni xix	12.6560	7.0	1.23e-14	15.1	-0.07	Fe xx 12.6210, Fe xxi 12.6490, Fe xvii 12.6950
Fe xxii	12.7540	7.2	1.74e-14	18.0	0.14	Fe xxi 12.7200, 12.7209, 12.7675
Fe xx	12.8460	7.1	5.96e-14	33.3	0.06	Fe xxi 12.8220, Fe xx 12.8240, 12.8640
Fe xx	12.9120	7.1	3.91e-14	26.6	-0.04	Fe xix 12.9033, 12.9330, 13.0220, 13.0220, Fe xviii 12.9494, Fe xxii 12.9530, Fe xx 12.9650
Fe xix	13.0220	7.1	3.81e-15	7.1	-0.22	
Fe xvii	13.1530	6.9	1.82e-14	18.0	0.25	Fe xx 13.1530, 13.1530, 13.1370, 13.1370
Fe xx	13.2740	7.1	2.16e-14	20.4	0.21	Fe xx 13.2453, Fe xix 13.2261, 13.2933, Fe xxii 13.2360, Ni xx 13.2560
Fe xviii	13.3230	7.0	1.28e-14	15.9	0.24	Ni xx 13.3090, Fe xviii 13.3312
Ne ix	13.4473	6.7	3.10e-13	79.2	0.03	Fe xix 13.4970, 13.5180, Ne ix 13.5531
Ne ix	13.6990	6.7	1.23e-13	50.4	0.07	Fe xix 13.6450, 13.7054
Fe xvii	13.8250	6.9	9.15e-14	43.7	0.13	Ni xix 13.7790, Fe xix 13.7950, Fe xvii 13.8920
Fe xviii	13.9530	7.0	2.23e-14	21.6	0.43	Fe xx 13.9620
Ni xix	14.0430	7.0	2.60e-14	23.4	-0.01	Fe xxi 14.0080, Fe xix 14.0179, 14.0340, 14.0388
Ni xix	14.0770	7.0	1.45e-14	17.5	0.02	Fe xviii 14.0549, Fe xx 14.0620, 14.0784
Fe xviii	14.2080	7.0	1.26e-13	51.5	-0.05	Fe xviii 14.2560
Fe xviii	14.3730	7.0	6.33e-14	36.3	-0.05	Fe xviii 14.3430, 14.3990, 14.4250, 14.4555
Fe xviii	14.5340	7.0	3.95e-14	28.9	-0.05	O viii 14.5242, Fe xviii 14.5608, 14.5710
Fe xix	14.6640	7.1	2.44e-14	22.7	-0.08	Fe xviii 14.6160, 14.6566, 14.6887, O viii 14.6343, 14.6344
Fe xx	14.7540	7.1	7.96e-15	13.0	-0.24	Fe xix 14.7250, Fe xviii 14.7499, 14.7510, Fe xx 14.7824
Fe xvi	14.9555	6.7	3.00e-14	25.7	-0.28	O viii 14.8205, 14.8207, Fe xviii 14.8920, Fe xix 14.9610, 14.9632
Fe xvii	15.0140	6.9	2.19e-13	69.4	-0.12	
Fe xix	15.0790	7.1	3.58e-14	28.1	0.43	
O viii	15.1760	6.6	5.28e-14	34.0	-0.05	O viii 15.1765, Fe xix 15.1770, 15.1980
Fe xvii	15.2610	6.9	9.18e-14	44.7	0.02	
Fe xviii	15.3539	7.0	1.94e-14	20.2	0.08	Fe xix 15.3123, 15.3340, Fe xvi 15.3694, 15.3907, 15.3926, 15.3992
Fe xvii	15.4530	6.8	2.66e-14	23.9	0.03	Fe xvi 15.4485, 15.4533, 15.5023, Fe xviii 15.4940, Fe xx 15.5170
Fe xviii	15.6250	7.0	2.67e-14	24.3	-0.10	
Fe xviii	15.7590	7.0	4.07e-15	9.5	-0.04	
Fe xviii	15.8240	7.0	2.24e-14	21.9	-0.19	Fe xviii 15.8700
O viii	16.0055	6.6	1.16e-13	50.5	-0.11	Fe xviii 16.0040, O viii 16.0067
Fe xviii	16.0710	7.0	5.07e-14	33.3	-0.08	Fe xviii 16.0450
Fe xviii	16.1590	7.0	2.25e-14	22.1	-0.08	Fe xix 16.1100
Fe xix	16.2830	7.1	1.41e-14	17.5	-0.21	Fe xvii 16.2285, 16.3500, Fe xix 16.2857, Fe xviii 16.3200
Fe xvii	16.7800	6.8	1.13e-13	50.0	-0.20	
Fe xvii	17.0510	6.8	2.85e-13	79.7	-0.13	Fe xvii 17.0960
O vii	17.3960	6.5	1.17e-14	16.1	0.35	Fe xix 17.3908
Fe xviii	17.6230	7.0	1.76e-14	20.0	-0.23	
O vii	17.7680	6.5	1.09e-14	15.3	-0.04	Ar xvi 17.7371, 17.7468
O vii	18.6270	6.4	1.81e-14	20.1	-0.40	Ca xviii 18.6909
O viii	18.9671	6.6	5.85e-13	114.0	-0.04	O viii 18.9725
N vii	20.9095	6.4	1.76e-14	18.7	-0.16	N vii 20.9106
O vii	21.6015	6.4	2.19e-13	66.0	0.05	
O vii	21.8036	6.4	4.96e-14	31.1	0.17	
O vii	22.0977	6.4	1.08e-13	45.8	-0.08	Ca xvi 22.1372
S xiv	23.0050	6.7	8.03e-15	10.5	0.16	
N vi	23.2770	6.3	5.08e-15	10.1	0.13	Ca xii 23.2473, Ca xvi 23.2608, Ca xiv 23.2711, Ca xii 23.3326, 23.3326
Ar xvi	23.5063	6.8	8.04e-15	13.3	-0.53	Ar xvi 23.5465, Ca xvi 23.5775, Ca xiv 23.5950, 23.6006
N vi	23.7710	6.3	5.14e-15	10.5	0.38	

**Table D.2.** (continued) *XMM-Newton*/RGS, EUVE, FUSE, and HST/STIS line fluxes of Proxima Centauri<sup>a</sup>.

Ion	$\lambda_{\text{model}}$ (Å)	$\log T_{\text{max}}$	$F_{\text{obs}}$	$S/N$	Ratio	Blends
S xiv	24.2000	6.7	4.38e-15	9.8	0.16	
S xiv	24.2850	6.7	6.88e-15	12.2	0.08	
S xiv	24.4180	6.7	5.82e-15	11.3	-0.08	Ca xiv 24.4046, Ca xv 24.4120, 24.4282, 24.4442, S xiii 24.4175
S xiv	24.5080	6.7	1.98e-15	6.6	-0.04	
S xiii	24.5900	6.6	5.43e-15	10.9	0.47	
N vii	24.7792	6.4	9.58e-14	45.5	-0.29	N vii 24.7846
Ar xvi	24.9942	6.8	8.89e-15	13.6	-0.21	Ar xvi 25.0098, Ca xiv 25.0636
No id.	25.1640	0.0	1.93e-15	6.4	...	
Ca xi	25.3270	6.4	5.08e-15	10.3	0.00	Ca xiii 25.3503
Ar xvi	25.5168	6.8	6.29e-15	11.3	-0.13	Ca xi 25.5170, Ca xiii 25.5301
Ar xvi	25.6844	6.8	7.50e-15	12.1	0.11	
C vi	26.3572	6.3	7.86e-15	12.4	-0.20	Ca xv 26.2720, Ar xiv 26.2730, C vi 26.3574, Ca xiv 26.3720, Ca xiii 26.3762
Si xii	26.4560	6.5	4.05e-15	8.8	0.37	Ar xiv 26.4300, Si xii 26.4590
C vi	26.9896	6.3	2.01e-14	19.6	0.07	S xiii 26.9792, C vi 26.9901, Ar xv 27.0432
Ar xiv	27.4640	6.7	1.50e-14	16.6	0.07	S xiii 27.3918, Ca xii 27.4131, Ar xiv 27.6360
C vi	28.4652	6.3	3.40e-14	23.6	0.12	Ar xv 28.3464, C vi 28.4663, Ca xii 28.4781
N vi	28.7870	6.3	2.48e-14	19.7	-0.19	
N vi	29.0843	6.2	1.30e-14	14.0	-0.14	Ca xiv 28.9586, 29.1320, Ar xiii 29.1420
S xii	29.2942	6.5	8.25e-15	11.1	0.25	Ar xiv 29.2060, Ca xiv 29.2123, 29.2577, Ar xiii 29.2245
Si xii	29.4390	6.5	1.99e-14	17.0	-0.22	Si xii 29.5090, N vi 29.5347
S xiv	30.4270	6.6	2.75e-14	19.2	-0.46	Ca xi 30.4480, S xiv 30.4690
Si xii	31.0120	6.5	5.82e-15	8.7	-0.28	Si xii 31.0230, S xi 31.0501
Ar xii	31.3030	6.5	3.38e-15	6.6	0.39	
S xiii	32.2391	6.6	1.05e-14	11.6	-0.21	S xiii 32.1911, Ca xii 32.2805
S xiv	32.4160	6.6	1.56e-14	14.1	-0.12	
S xiv	32.5600	6.6	2.00e-14	15.7	-0.39	S xiv 32.5750, Ca xii 32.6571
S xiv	33.5490	6.6	1.40e-14	12.9	-0.11	
C vi	33.7342	6.2	1.69e-13	45.0	0.23	C vi 33.7396
S xiii	33.9461	6.5	1.23e-14	11.9	0.63	S xiii 33.9526, Fe xvii 33.9618
C v	34.9728	6.1	7.26e-15	9.0	0.26	Ar ix 35.0240, Fe xvi 35.1059
Fe xvii	35.6844	6.9	1.86e-14	14.5	0.13	Ca xi 35.7370
Fe xviii	93.9230	7.0	1.10e-14	3.8	-0.80	Fe xx 93.7800
Ne viii	98.2600	5.9	2.31e-14	5.7	-0.04	Fe xxi 97.8800, Ne viii 98.1150, 98.2740
Fe xx	121.8300	7.1	1.63e-14	4.5	-0.14	
Fe xxi	128.7300	7.2	1.40e-14	3.5	-0.37	
Fe xxiii	132.8500	7.3	4.22e-14	6.5	-0.34	Fe xx 132.8500
Fe xxii	135.7800	7.2	1.45e-14	3.2	-0.28	Fe xi 135.6988
Fe xv	284.1630	6.4	1.53e-13	4.3	-0.04	
Fe xvi	335.4099	6.5	1.80e-13	6.6	-0.07	Fe xiv 334.1800
Mg ix	368.0577	6.1	9.96e-14	4.5	-0.01	
S xiv	417.6655	6.6	1.17e-13	3.2	-0.06	Fe xv 417.2580
S vi	933.3788	5.4	2.28e-15	3.6	-0.22	
O vi	1031.9121	5.6	1.42e-13	18.2	0.31	
C ii	1036.3390	4.8	2.34e-15	6.6	-0.61	
C ii	1037.0200	4.8	8.05e-15	8.7	-0.37	
O vi	1037.6136	5.6	7.04e-14	15.5	0.31	
Si iii	1108.3610	4.9	1.22e-15	4.6	0.01	
Si iii	1109.9720	4.9	1.74e-15	5.3	-0.20	Si iii 1109.9430
Si iv	1122.4852	5.0	7.56e-16	5.0	0.14	
Si iv	1128.3404	5.0	1.64e-15	6.4	0.23	
Ne v	1145.5959	5.5	5.90e-16	5.7	-0.28	
C iii	1176.0000	4.8	5.81e-14	7.5	-0.31	
C iii	1176.0000	4.8	6.20e-14	20.9	-0.28	
S iii	1200.9610	4.9	3.18e-15	42.6	-0.10	
O v	1218.3440	5.5	1.40e-14	104.6	0.17	
N v	1238.8218	5.4	4.28e-14	74.6	0.20	
N v	1242.8042	5.4	2.02e-14	45.8	0.17	
C iii	1247.3830	5.1	6.29e-16	18.7	-0.21	
Si ii	1264.7400	4.5	1.64e-15	20.6	-0.03	
Si ii	1265.0040	4.6	1.06e-15	48.7	-0.08	
Si iii	1294.5480	4.9	8.71e-16	12.5	0.70	
Si iii	1296.7280	4.9	9.89e-16	31.3	0.35	
Si iii	1298.9480	4.9	2.30e-15	35.0	0.65	
Si iii	1301.1510	4.9	6.32e-16	15.3	0.63	
Si iii	1303.3249	4.9	8.65e-16	33.3	0.20	
Si ii	1304.3719	4.6	4.01e-16	26.3	-0.20	
Si ii	1309.2770	4.6	7.10e-16	15.1	-0.25	
C ii	1323.9080	4.8	4.07e-16	11.9	-0.55	C ii 1323.9540
Fe xix	1328.6999	7.1	4.21e-16	23.4	-0.44	
C ii	1334.5350	4.7	1.75e-14	43.7	-0.66	
C ii	1335.7100	4.7	4.45e-14	69.5	-0.05	C ii 1335.6650
Fe xii	1349.4000	6.3	4.75e-16	38.4	0.01	
O v	1371.2960	5.5	2.22e-15	22.4	-0.03	
Si iv	1393.7552	5.0	2.34e-14	70.3	-0.11	
O iv	1397.2309	5.3	7.47e-16	24.2	-0.49	
Si iv	1402.7704	5.0	1.14e-14	82.1	-0.12	
S iv	1406.0160	5.1	4.28e-15	77.5	-0.06	
Fe xi	1467.4230	6.2	3.28e-16	12.1	-0.07	
Si ii	1526.7090	4.5	1.58e-15	25.5	0.04	
Si ii	1533.4320	4.5	2.60e-15	25.7	-0.04	

**Table D.2.** (continued) *XMM-Newton*/RGS, EUVE, FUSE, and HST/STIS line fluxes of Proxima Centauri<sup>a</sup>.

Ion	$\lambda_{\text{model}}$ (Å)	$\log T_{\text{max}}$	$F_{\text{obs}}$	$S/N$	Ratio	Blends
C IV	1548.1871	5.1	1.31e-13	71.8	0.16	
C IV	1550.7723	5.1	6.60e-14	40.6	0.16	
Al II	1670.7870	4.6	1.12e-14	20.8	-0.01	

**Notes.** <sup>(a)</sup> Line fluxes (in  $\text{erg cm}^{-2} \text{s}^{-1}$  units) measured in the spectra, and corrected by the ISM absorption when needed.  $\log T_{\text{max}}$  (K) indicates the maximum temperature of formation of the line (unweighted by the EMD). “Ratio” is the observed-to-predicted line flux ratio,  $\log(F_{\text{obs}}/F_{\text{pred}})$ , with predicted flux as calculated with the resulting EMD. “Blends” amounting to more than 5% of the total flux for each line are indicated, with wavelengths in Å.

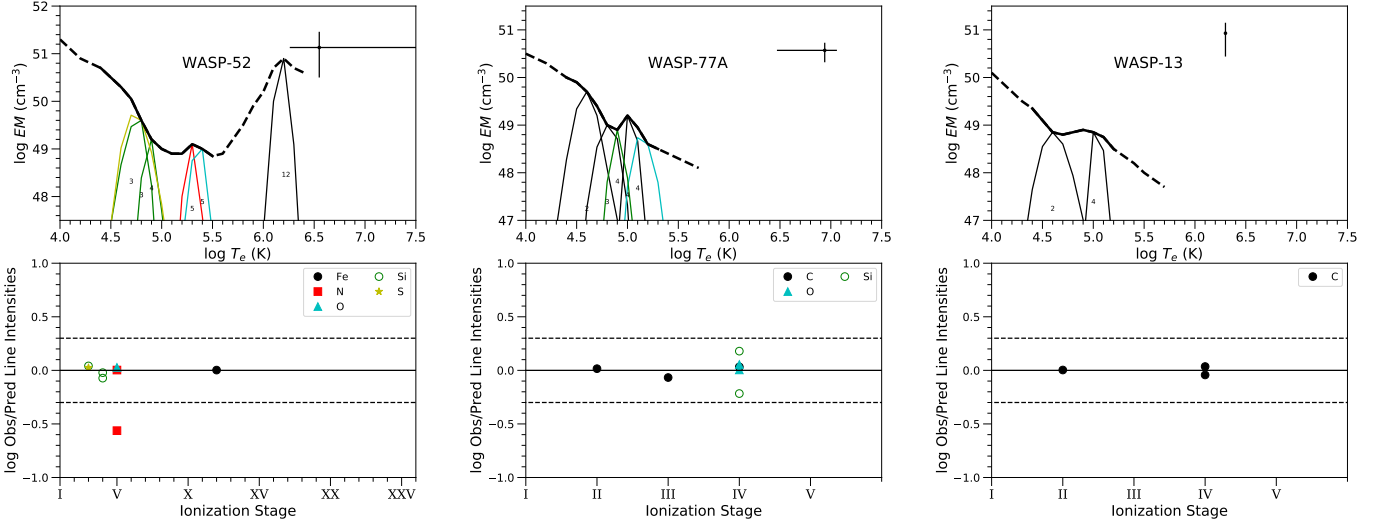


**Fig. D.2.** Emission Measure Distributions as in Fig. 1, using HST/STIS data for WASP-52 (*left*) and WASP-77 (*center*), and HST/COS data for WASP-13 (*right*). The 1- $T$  global fit to Chandra/ACIS spectra is also indicated with error bars.

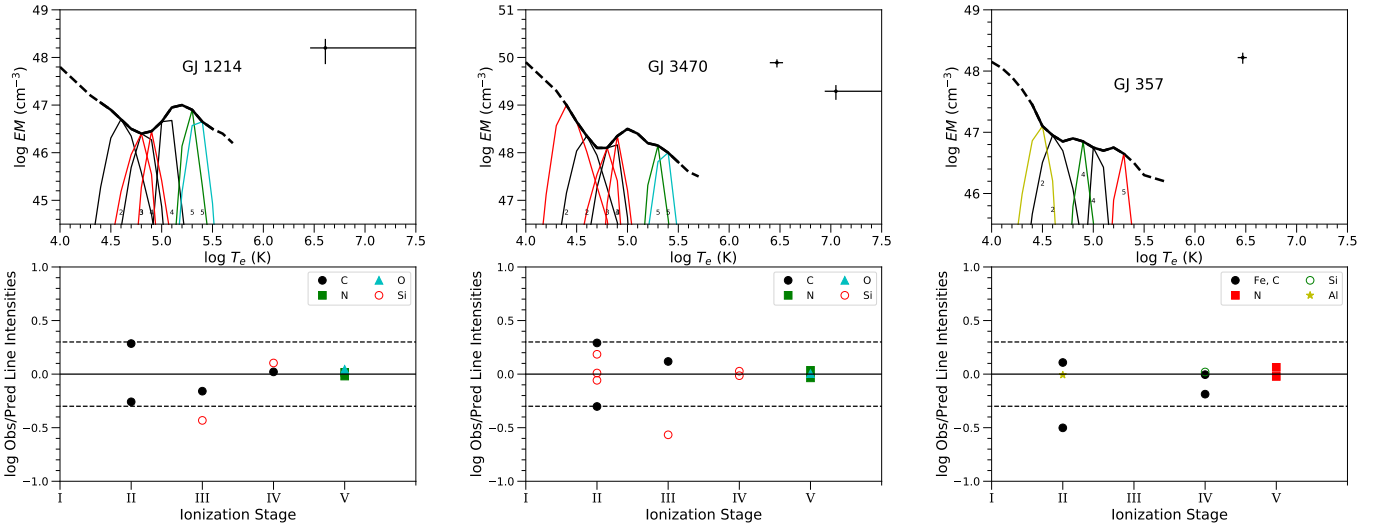


**Fig. D.3.** Same as in Fig. 1 but for GJ 1214, GJ 3470, and GJ 357, using HST/COS data. The 1- $T$  and 2- $T$  global fits to XMM-Newton/EPIC spectra are also indicated with error bars.

**Table D.3.** *XMM-Newton*/RGS, EUVE, FUSE, and HST/STIS line fluxes of AU Mic<sup>a</sup>.

Ion	$\lambda_{\text{model}}$ (Å)	$\log T_{\text{max}}$	$F_{\text{obs}}$	$S/N$	Ratio	Blends
Mg XII	8.4192	7.1	2.58e-14	9.5	-0.43	Mg XII 8.4246
Mg XI	9.1687	6.9	5.81e-14	15.9	0.02	Fe XXI 9.1944
Mg XI	9.2312	6.9	2.47e-14	10.5	-0.15	Fe XII 9.2298, Ne X 9.2461, 9.2462, Ne X 9.2912, 9.2913
Mg XI	9.3143	6.9	5.40e-14	15.7	0.14	Ne X 9.3616
Ne X	9.4807	6.9	4.07e-14	13.9	0.02	Ne X 9.4809
Ne X	9.7080	6.9	6.78e-14	18.5	-0.14	Ne X 9.7085
Ne X	10.2385	6.9	1.43e-13	28.2	-0.23	Ne X 10.2396
Fe XVIII	10.5364	7.0	3.38e-14	14.2	-0.04	Fe XVII 10.5040, Fe XVIII 10.5382, 10.5640, Ne IX 10.5406, 10.5650
Fe XIX	10.6193	7.1	5.43e-14	18.2	-0.09	Fe XIX 10.6001, 10.6116, 10.6840, Fe XXIV 10.6190, 10.6630, Ne IX 10.6426, Fe XVII 10.6570
Fe XVII	10.7700	6.9	2.40e-14	12.3	-0.10	Fe XIX 10.7650, Ne IX 10.7650
Fe XXIII	10.9810	7.3	8.26e-14	22.8	-0.01	Ne IX 11.0010, Fe XXIII 11.0190, Fe XVII 11.0260, Fe XXIV 11.0290
Fe XXIV	11.1760	7.4	3.13e-14	14.5	-0.11	Fe XVII 11.1310
Fe XVII	11.2540	6.9	3.99e-14	16.4	0.08	Fe XXIV 11.2680
Fe XVIII	11.4230	7.0	3.20e-14	14.6	-0.20	Fe XXI 11.4270, Fe XVIII 11.4274, Fe XXIV 11.4320, Fe XXIII 11.4580
Ne IX	11.5440	6.7	1.22e-13	27.7	-0.04	Fe XVIII 11.5270
Fe XXII	11.7700	7.2	9.03e-14	25.5	-0.07	Fe XXIII 11.7360
Ni XX	11.8320	7.1	4.61e-15	5.8	-0.24	Ni XX 11.8460
Fe XXII	11.9770	7.2	3.37e-14	16.0	-0.09	Fe XXII 11.8810, 11.9320, 11.9474, Fe XXI 11.9023, 11.9750
Ne X	12.1321	6.9	9.03e-13	83.7	-0.25	Ne X 12.1375
Fe XXI	12.2840	7.2	1.31e-13	32.2	-0.08	Fe XVII 12.2660
Ni XIX	12.4350	7.0	9.12e-14	27.1	0.04	Fe XXI 12.3930, 12.4990, Fe XX 12.4234, 12.4310, 12.5760
Fe XXI	12.6490	7.2	4.33e-14	18.9	0.48	Ni XIX 12.6560, Fe XVII 12.6950
Fe XX	12.8460	7.1	1.09e-13	29.9	-0.14	Fe XXI 12.8220, Fe XX 12.8240, 12.8640
Fe XX	12.9120	7.1	8.79e-14	26.4	-0.07	Fe XIX 12.9033, 12.9330, 13.0220, Fe XVIII 12.9494, Fe XXII 12.9530, Fe XX 12.9650, 12.9920
Fe XX	13.1530	7.1	3.72e-14	15.1	0.16	Fe XX 13.1530, 13.1370, 13.1370
Fe XX	13.2740	7.1	5.00e-14	20.6	0.03	Fe XIX 13.2261, 13.2933, Fe XXII 13.2360, Fe XX 13.2453, Ni XX 13.3090, Fe XVIII 13.3230
Ne IX	13.4473	6.7	8.00e-13	83.6	-0.04	Fe XIX 13.4970, 13.5180, Ne IX 13.5531
Ne IX	13.6990	6.7	4.01e-13	59.5	0.10	Fe XIX 13.7054
Fe XVII	13.8250	6.9	1.79e-13	40.2	0.13	Fe XIX 13.7590, 13.7950, 13.8390, Fe XX 13.7670, Ni XIX 13.7790, Fe XVII 13.8920
Fe XX	13.9620	7.1	4.74e-14	20.8	0.40	Fe XVIII 13.9530
Fe XXI	14.0080	7.2	3.97e-14	19.0	-0.09	Fe XIX 14.0179, Cr XXI 14.0339, Fe XIX 14.0340, 14.0388, Ni XIX 14.0430
Ni XIX	14.0770	7.0	4.23e-14	19.7	0.42	Fe XVIII 14.0549, Fe XX 14.0620, 14.0784
Fe XVIII	14.2080	7.0	2.68e-13	49.5	-0.07	Fe XVIII 14.2560
Fe XVIII	14.3730	7.0	1.40e-13	35.7	-0.06	Fe XVIII 14.3430, 14.3990, 14.4250, 14.4555
Fe XVIII	14.5340	7.0	1.06e-13	31.5	0.01	O VIII 14.5242, 14.5243, Fe XVIII 14.5608, 14.5710
Fe XIX	14.6640	7.1	7.88e-14	27.2	-0.17	O VIII 14.6343, 14.6344, Fe XIX 14.7250, Fe XVIII 14.7499, Fe XX 14.7540
O VIII	14.8205	6.6	5.21e-14	22.3	-0.03	O VIII 14.8207
Fe XIX	14.9610	7.1	2.41e-14	15.2	-0.38	Fe XX 14.8791, 14.9279, Fe XVIII 14.8920, 14.9717, Fe XIX 14.8995, 14.9170, 14.9632
Fe XVII	15.0140	6.9	3.79e-13	60.4	-0.09	
Fe XIX	15.0790	7.1	5.52e-14	23.1	0.19	
O VIII	15.1760	6.6	1.47e-13	37.3	-0.08	O VIII 15.1765, Fe XIX 15.1770, 15.1980
Fe XVII	15.2610	6.9	1.54e-13	38.1	0.04	
Fe XVIII	15.3539	7.0	3.59e-14	18.0	0.03	Fe XIX 15.3123, 15.3340, 15.3709, Fe XVI 15.3907
Fe XVII	15.4530	6.8	4.93e-14	21.2	0.07	Fe XVI 15.4533, Fe XVIII 15.4940, Fe XX 15.5170
Fe XVIII	15.6250	7.0	4.65e-14	21.1	-0.19	
Fe XVIII	15.7590	7.0	1.19e-14	10.8	0.10	
Fe XVIII	15.8700	7.0	4.65e-14	21.1	-0.20	Fe XVIII 15.8240
O VIII	16.0055	6.6	2.99e-13	54.4	-0.16	Fe XVIII 16.0040, O VIII 16.0067
Fe XVIII	16.0710	7.0	1.11e-13	33.1	-0.06	Fe XVIII 16.0450
Fe XVIII	16.1590	7.0	1.79e-14	13.1	-0.58	Fe XIX 16.1100
Fe XIX	16.2830	7.1	2.92e-14	16.8	-0.23	Fe XVII 16.2285, 16.3500, Fe XIX 16.2857, 16.3247, Fe XVIII 16.3200
Fe XVII	16.7800	6.8	2.12e-13	45.7	-0.12	
Fe XVII	17.0510	6.8	5.23e-13	70.5	-0.06	Fe XVII 17.0960
O VII	17.3960	6.5	3.61e-14	18.1	0.07	Cr XVIII 17.4031, Cr XVI 17.4207, 17.4252
Fe XVIII	17.6230	7.0	4.55e-14	21.0	-0.15	
O VII	17.7680	6.5	3.50e-14	17.8	0.08	Ar XVI 17.7371, 17.7468
O VII	18.6270	6.4	6.85e-14	26.5	-0.30	Ca XVIII 18.6909
O VIII	18.9671	6.6	1.41e-12	119.3	-0.16	O VIII 18.9725
N VII	20.9095	6.4	4.56e-14	20.4	0.26	
Ca XVI	21.4501	6.8	1.64e-14	12.6	-0.56	
O VII	21.6015	6.4	3.59e-13	59.0	-0.04	
O VII	21.8036	6.4	7.47e-14	26.8	0.07	
No id.	21.9686	0.0	1.11e-14	10.3	...	
O VII	22.0977	6.4	2.65e-13	50.2	0.02	Ca XVI 22.1372
S XIV	23.0050	6.7	1.56e-14	10.2	-0.05	S XIV 23.0150, Ca XV 23.0230, Ca XVI 23.0433
N VI	23.1274	6.3	1.34e-14	9.6	0.16	Ca XIV 23.1518, Ca XVII 23.1752, Ca XV 23.1818, Ca XII 23.1892
N VI	23.2770	6.3	1.64e-14	12.5	0.39	Ca XII 23.2473, 23.3326, Ca XVI 23.2608, Ca XIV 23.2711
Ar XVI	23.5063	6.8	3.67e-14	19.3	0.05	Ca XV 23.5034
Ar XVI	23.5465	6.8	1.38e-14	11.9	-0.14	Ca XIV 23.6006
No id.	23.7700	0.0	3.14e-14	12.6	...	
Ca XIV	24.0860	6.7	2.16e-14	15.2	-0.36	Ca XIV 24.0335
S XIV	24.2000	6.7	2.48e-14	16.4	-0.38	Ca XIV 24.1331, Ca XVI 24.2214, Ca XV 24.2344
S XIV	24.2850	6.7	2.13e-14	15.2	0.12	Ca XIV 24.2599, S XIV 24.2890
S XIV	24.4180	6.7	2.46e-14	16.3	0.16	Ca XV 24.3365, 24.4120, 24.4282, 24.4442, Ca XIV 24.4046
S XIII	24.5900	6.6	2.61e-14	16.8	0.48	S XIV 24.5080, Si XIII 24.5172, Ca XV 24.5274
N VII	24.7792	6.4	1.97e-13	45.3	-0.16	Ar XV 24.7400, N VII 24.7846, Ar XVI 24.8509
Ar XVI	24.9942	6.8	5.24e-14	23.4	0.04	Ar XVI 25.0098
No id.	25.2000	0.0	1.15e-14	11.0	...	
Ca XI	25.3270	6.4	1.55e-14	12.8	0.27	Ca XIII 25.3503
Ar XVI	25.5168	6.8	2.21e-14	15.2	-0.28	Ca XV 25.4749, Ca XI 25.5170, Ca XIII 25.5301
Ar XVI	25.6844	6.8	7.53e-14	27.0	0.28	Si XII 25.6580, Ca XIV 25.7299, Ca XVI 25.7330
C VI	26.3572	6.3	3.33e-14	18.3	0.03	Ca XV 26.2720, Ar XIV 26.2730, C VI 26.3574, Ca XIV 26.3720, Ca XIII 26.3762
Si XII	26.4560	6.5	4.21e-14	20.4	0.36	Ar XIV 26.4300, Si XII 26.4590, Ca XIV 26.5141, Ca XIII 26.5862
C VI	26.9896	6.3	7.35e-14	26.8	0.13	C VI 26.9901, Si XII 27.0350, Ar XV 27.0432

**Table D.3.** (continued) *XMM-Newton*/RGS, EUVE, FUSE, and HST/STIS line fluxes of AU Mic<sup>a</sup>.

Ion	$\lambda_{\text{model}}$ (Å)	$\log T_{\text{max}}$	$F_{\text{obs}}$	$S/N$	Ratio	Blends
Ar xiv	27.4640	6.7	4.55e-14	20.9	0.32	S xii 27.3918, Ca xii 27.4131
Fe xvii	27.5097	6.9	3.14e-14	16.8	0.53	S xv 27.5300, 27.5598, Ar xiv 27.5490, 27.6310, 27.6360, Ar xv 27.5559
C vi	28.4652	6.3	7.51e-14	25.8	-0.04	Ar xv 28.3464, C vi 28.4663, Ca xii 28.4781
Ca xii	28.6811	6.5	1.40e-14	11.1	0.34	Ca xii 28.6131, 28.6370
N vi	28.7870	6.3	1.46e-14	11.3	-0.27	
Ca xiii	28.9161	6.6	1.37e-14	11.0	0.21	Ar xiv 28.8940
N vi	29.0843	6.2	3.69e-14	17.2	0.17	Ca xiv 29.1320, Ar xiii 29.1420
Ar xiii	29.2245	6.6	3.31e-14	15.9	0.47	Ar xiv 29.2060, Ca xiv 29.2123, 29.2577, Ar xv 29.2210
N vi	29.5347	6.2	4.96e-14	19.8	0.10	Si xii 29.4390, 29.5090
S xiv	30.4270	6.6	4.68e-14	18.6	-0.40	Ca xi 30.4480, S xiv 30.4690
Ca xiii	30.5402	6.6	1.32e-14	9.8	0.64	Ca x 30.5033
Ca xi	30.8670	6.4	1.59e-14	10.9	0.26	Ar xiv 30.8320, Ar xiii 30.8854
Si xii	31.0120	6.5	3.50e-14	15.9	-0.27	Si xii 31.0230
Fe xvii	31.9515	6.9	3.04e-14	15.0	0.45	Fe xvii 31.8776, Ar xiii 31.8954, Ca xii 31.9561, Ar xiv 32.0140
Fe xvii	32.1188	6.9	1.07e-14	8.9	0.51	Fe xvii 32.0941, Ca xii 32.1057, Fe xvi 32.1658
S xiii	32.2391	6.6	3.84e-14	16.8	0.18	S xiii 32.1911, Ca xii 32.2805
S xiv	32.4160	6.6	3.38e-14	15.7	0.04	Ca xii 32.4184
S xiv	32.5600	6.6	6.38e-14	21.2	-0.13	Ca xii 32.4988, 32.6571, S xiv 32.5750
S xiv	33.3810	6.6	1.52e-14	10.2	0.10	
C v	33.4257	6.1	1.13e-14	8.9	0.29	Ca xiii 33.4080, Si xiv 33.4444, Ar xiv 33.4600
S xiv	33.5490	6.6	3.65e-14	15.5	-0.05	Si xiv 33.5051, Si xi 33.5301, 33.5731
C vi	33.7342	6.2	2.89e-13	44.2	-0.08	C vi 33.7396
Fe xvii	33.8758	6.9	1.38e-14	9.5	0.33	Fe xvii 33.8863, Si xi 33.9070, S xiii 33.9461, 33.9526
C v	34.9728	6.1	2.57e-14	12.9	0.47	Ar xiii 34.8385, Fe xvi 34.8569, Ar ix 35.0240
Ca xi	35.2130	6.4	3.40e-14	14.7	-0.00	
Si xi	35.4374	6.3	1.33e-14	9.4	0.40	S xii 35.3990, Ca xiii 35.4444
Ca xi	35.5760	6.4	1.07e-14	8.5	-0.33	
Fe xvii	35.6844	6.9	3.39e-14	14.7	0.21	Fe xxi 35.6238, Ca xi 35.7370
Fe xviii	93.9230	7.0	1.04e-13	9.1	-0.11	Fe xx 93.7800
Ne viii	98.2600	5.9	1.02e-13	9.8	0.26	Fe xxi 97.8800, Ne viii 98.1150, 98.2740
Fe xix	101.5500	7.0	4.85e-14	7.3	0.11	
Fe xxi	102.2200	7.2	1.03e-13	11.0	0.20	O viii 102.3476, 102.3552, 102.3919, 102.4897, 102.5497
Ne viii	103.0850	5.9	3.27e-14	5.6	0.30	Fe ix 103.5662
Fe xviii	103.9370	7.0	2.42e-14	4.8	-0.22	
Fe xix	106.3300	7.0	2.38e-14	3.9	0.38	Ni xxii 106.0640, Fe xix 106.1200, Ne viii 106.1900
Fe xix	108.3700	7.0	9.00e-14	9.6	-0.06	Fe xxi 108.1200
Fe xix	109.9700	7.0	2.91e-14	4.7	0.21	
Fe xxii	114.4100	7.2	3.06e-14	4.9	0.26	
Fe xxii	117.1700	7.2	1.27e-13	12.5	0.10	Fe xxi 117.5100
Ni xxii	117.9330	7.2	2.32e-14	3.9	0.15	Ni xxv 117.9330, Si v 117.8540, Cr xx 117.9580
Fe xx	118.6600	7.1	4.72e-14	6.7	0.14	
Fe xx	121.8300	7.1	5.56e-14	7.3	-0.06	
Fe xxi	128.7300	7.2	1.18e-13	10.8	0.11	
Fe xxiii	132.8500	7.3	3.76e-13	20.7	0.19	Fe xx 132.8500
Fe xxii	135.7800	7.2	8.62e-14	8.7	0.09	
Fe ix	171.0730	6.0	7.18e-14	4.7	-0.04	O v 172.1690
Fe xi	182.1690	6.2	4.85e-14	3.7	0.59	C vi 182.0969, 182.1323, C vi 182.2304, 182.2900, Fe x 182.3070
Fe xxiv	192.0170	7.4	2.86e-13	11.0	-0.29	Ca xvii 192.8532
Fe xiii	197.4330	6.3	4.94e-14	3.4	0.70	Fe xiii 196.7675, 196.8215, Fe ix 197.3784
Ar xv	221.1356	6.7	8.41e-14	4.7	-0.26	S xii 221.4005
S xiii	256.6852	6.5	1.50e-13	6.9	-0.38	He ii 256.3183, 256.3194, Si x 256.3660
S x	264.2306	6.3	5.58e-14	3.7	0.03	Fe xiv 264.7900
Si x	277.2780	6.2	3.89e-14	3.1	-0.18	
Fe xv	284.1630	6.4	1.96e-13	8.4	-0.00	
Si viii	314.3560	6.0	5.45e-14	3.6	0.13	
Fe xvi	335.4099	6.5	1.55e-13	9.8	-0.23	Fe xiv 334.1800
Ar xvi	353.8535	6.8	7.21e-14	6.4	-0.26	
Fe xvi	360.7580	6.5	9.12e-14	7.3	-0.18	Ne v 359.3750
Mg ix	368.0577	6.1	3.78e-14	4.1	0.38	
S xiv	417.6655	6.6	6.55e-14	4.0	-0.42	Fe xv 417.2580
Ne vi	558.6850	5.7	1.48e-13	4.1	-0.25	O iv 555.2630, Ca x 557.7640, Ne v 568.4220
S vi	933.3788	5.4	3.57e-15	3.3	-0.21	
N iii	991.5770	5.0	7.91e-15	4.8	-0.41	
Ne vi	999.1830	5.7	4.52e-15	4.0	0.45	
Ne vi	1010.2050	5.7	1.90e-15	4.2	0.48	
S iii	1021.3230	4.9	2.05e-15	5.5	0.31	
O vi	1031.9121	5.6	2.29e-13	16.0	0.15	
C ii	1036.3390	4.8	8.63e-15	6.2	-0.28	
C ii	1037.0200	4.8	1.71e-14	7.2	-0.29	
O vi	1037.6136	5.6	1.15e-13	13.7	0.15	
S iv	1062.6639	5.1	2.04e-15	7.0	-0.73	
S iv	1072.9740	5.1	5.14e-15	8.4	-0.14	
S iii	1077.1730	4.9	1.99e-15	8.7	0.16	
N ii	1085.7030	4.7	1.16e-14	3.4	0.39	N ii 1085.5310, 1085.5480
Si iii	1108.3610	4.9	2.09e-15	6.4	-0.08	
Si iii	1109.9720	4.9	5.92e-15	6.3	0.19	
Si iii	1113.2320	4.9	5.90e-15	7.3	-0.19	Si iii 1113.2061
Fe xix	1118.0699	7.0	5.73e-15	6.4	-0.19	
Si iv	1122.4852	5.0	5.01e-15	7.1	0.39	
Si iv	1128.3404	5.0	4.55e-15	6.7	0.05	Si iv 1128.3252
Ne v	1145.5959	5.5	2.01e-15	6.3	-0.37	
S iii	1190.1990	4.9	2.80e-15	8.1	0.13	
Si ii	1190.4170	4.6	1.53e-15	4.8	-0.07	
S iii	1194.0490	4.9	4.81e-15	11.8	0.45	

**Table D.3.** (continued) *XMM-Newton*/RGS, EUVE, FUSE, and HST/STIS line fluxes of AU Mic<sup>a</sup>.

Ion	$\lambda_{\text{model}}$ (Å)	$\log T_{\text{max}}$	$F_{\text{obs}}$	$S/N$	Ratio	Blends
Si II	1194.5010	4.6	4.36e-15	13.7	-0.36	Sm 1194.4430
S III	1200.9610	4.9	8.55e-15	23.6	0.74	
Si III	1206.5019	4.9	1.24e-13	35.7	-0.68	
O V	1218.3440	5.5	2.26e-14	77.0	-0.22	
N V	1238.8218	5.4	6.78e-14	37.0	0.12	
N V	1242.8042	5.4	3.30e-14	23.2	0.11	
C III	1247.3830	5.1	6.14e-15	11.5	0.40	
S II	1259.5210	4.6	3.03e-15	12.6	0.04	
Si II	1264.7400	4.5	6.67e-15	13.4	-0.13	
Si II	1265.0040	4.6	3.80e-15	15.9	-0.20	
Si III	1296.7280	4.9	4.88e-15	17.2	0.72	
Si III	1303.3249	4.9	4.96e-15	19.7	0.64	
Si II	1304.3719	4.6	1.91e-15	9.3	-0.22	
Si II	1309.2770	4.6	4.61e-15	15.7	-0.14	
Si III	1312.5930	4.9	1.80e-15	9.5	-0.42	
C II	1323.9080	4.8	2.88e-15	8.7	0.39	
Fe XIX	1328.6999	7.1	9.39e-16	6.3	-0.51	
C II	1334.5350	4.7	9.08e-14	56.4	-0.25	
C II	1335.7100	4.7	1.96e-13	59.7	0.44	
O IV	1338.6140	5.3	1.16e-15	9.0	0.49	
Fe XXI	1354.0800	7.2	7.92e-15	13.6	-0.27	
O V	1371.2960	5.5	4.95e-15	18.6	-0.27	
Si IV	1393.7552	5.0	1.26e-13	33.2	0.13	
Si IV	1402.7704	5.0	7.09e-14	25.3	0.18	
S IV	1406.0160	5.1	9.56e-16	16.3	-0.59	
Cr XVI	1410.5990	6.8	4.83e-16	14.2	0.06	
S V	1501.7660	5.3	1.26e-15	21.3	-0.04	
Si II	1526.7090	4.5	8.62e-15	19.6	0.03	
Si II	1533.4320	4.5	1.03e-14	9.7	-0.19	
C IV	1548.1871	5.1	4.30e-13	49.9	0.04	
C IV	1550.7723	5.1	2.24e-13	35.3	0.06	
Al II	1670.7870	4.6	2.35e-14	27.1	0.02	

**Notes.** <sup>(a)</sup> Line fluxes (in  $\text{erg cm}^{-2} \text{s}^{-1}$  units) measured in the spectra, and corrected by the ISM absorption when needed.  $\log T_{\text{max}}$  (K) indicates the maximum temperature of formation of the line (unweighted by the EMD). “Ratio” is the  $\log(F_{\text{obs}}/F_{\text{pred}})$  of the line. “Blends” amounting to more than 5% of the total flux for each line are indicated, with wavelengths in Å.

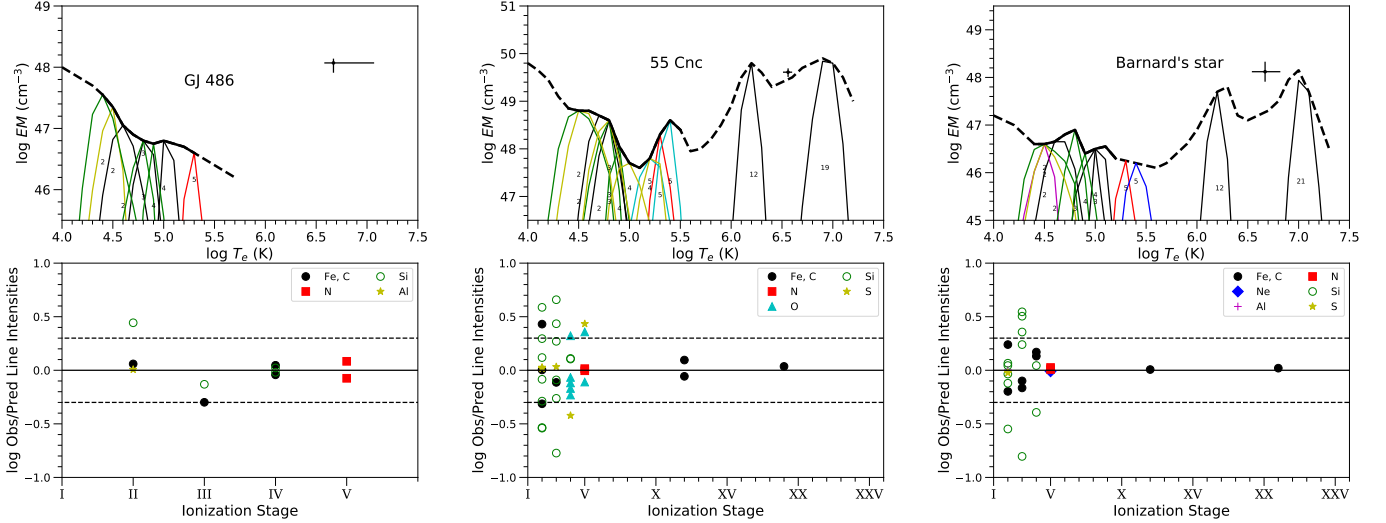


**Fig. D.4.** Same as in Fig. 1 but for GJ 486, 55 Cnc, and Barnard’s star (GJ 699), using HST/STIS and COS data. The 1- $T$  global fit to *XMM-Newton*/EPIC (GJ 486 and 55 Cnc) and *Chandra*/ACIS-S (Barnard’s star) spectra are also indicated with error bars. In 55 Cnc (*center*) and Barnard’s star (*right*), coronal lines in the HST/COS spectra were used to tentatively extend the EMD to coronal temperatures.

**Table D.4.** *XMM-Newton*/RGS and HST/COS line fluxes of  $\tau$  Boo<sup>a</sup>.

Ion	$\lambda_{\text{model}}$ (Å)	$\log T_{\text{max}}$	$F_{\text{obs}}$	$S/N$	Ratio	Blends
Fe xvii	11.2540	6.9	2.68e-14	7.2	0.38	Fe xviii 11.3260, 11.3260, 11.3260
Ne x	12.1321	6.9	4.70e-14	4.1	-0.03	Fe xvii 12.1240, Ne x 12.1375
Fe xvii	12.2660	6.9	1.50e-14	3.0	-0.10	
Ne ix	13.4473	6.7	5.02e-14	7.7	0.04	Fe xix 13.5180, Ne ix 13.5531
Ne ix	13.6990	6.7	2.10e-14	7.3	0.00	
Fe xvii	13.8250	6.9	1.97e-14	5.0	-0.14	Ni xix 13.7790, Fe xvii 13.8920
Ni xix	14.0430	7.0	2.53e-14	6.9	-0.01	Fe xviii 13.9530, Ni xix 14.0770
Fe xviii	14.2080	7.0	2.70e-14	7.9	-0.06	Fe xviii 14.2560
Fe xviii	14.3730	7.0	1.15e-14	4.6	-0.20	Fe xviii 14.3430, 14.3430, 14.3990, 14.4250, 14.4250, 14.4555
Fe xviii	14.5340	7.0	5.76e-15	3.7	-0.26	O viii 14.5242, Fe xviii 14.5608, 14.5710, 14.6160
Fe xvi	14.9555	6.7	2.28e-15	3.5	-0.63	Fe xix 14.9610
Fe xvii	15.0140	6.9	1.48e-13	28.0	-0.05	Fe xvi 15.0496
O viii	15.1760	6.6	2.77e-14	6.6	0.39	O viii 15.1765, Fe xix 15.1980
Fe xvii	15.2610	6.9	5.48e-14	13.5	0.05	
Fe xvii	15.4530	6.8	3.64e-14	7.9	0.26	Fe xvi 15.3907, 15.4485, 15.4533, 15.4955, 15.5023
Fe xviii	15.6250	7.0	1.26e-14	5.5	0.18	
Fe xviii	15.8240	7.0	8.63e-15	6.9	0.01	Fe xviii 15.8700
O viii	16.0055	6.6	3.49e-14	6.6	-0.07	Fe xvii 15.9956, Fe xviii 16.0040, O viii 16.0067
Fe xviii	16.0710	7.0	1.96e-14	5.4	-0.00	Fe xviii 16.0450, 16.1590, Fe xix 16.1100
Fe xvii	16.7800	6.8	9.26e-14	15.3	-0.03	
Fe xvii	17.0510	6.8	2.30e-13	16.6	-0.02	Fe xvii 17.0960
O vii	18.6270	6.4	7.02e-15	3.3	-0.06	
O viii	18.9671	6.6	1.32e-13	19.3	-0.14	O viii 18.9725
O vii	21.6015	6.4	4.50e-14	6.6	-0.03	
O vii	22.0977	6.4	3.71e-14	5.8	0.07	
N vii	24.7792	6.4	1.28e-14	4.4	-0.09	N vii 24.7846
C vi	28.4652	6.3	7.02e-15	4.0	0.08	Ag xv 28.3464, C vi 28.4663
C vi	33.7342	6.2	2.52e-14	6.5	-0.11	S xiv 33.5490, C vi 33.7396
S v	1199.1360	5.3	1.68e-15	12.3	0.01	
S iii	1200.9611	4.9	2.50e-15	14.1	0.02	
Si iii	1206.5019	4.9	1.20e-13	43.5	-0.01	
O v	1218.3440	5.5	1.10e-14	29.4	-0.18	
N v	1238.8218	5.4	2.02e-14	30.2	0.05	
N v	1242.8042	5.4	1.00e-14	23.0	0.04	

**Notes.** <sup>(a)</sup> Line fluxes (in erg cm<sup>-2</sup> s<sup>-1</sup>) units measured in the spectra, and corrected by the ISM absorption when needed. *XMM-Newton*/RGS  $\tau$  Boo data from Maggio et al. (2011).  $\log T_{\text{max}}$  (K) indicates the maximum temperature of formation of the line (unweighted by the EMD). “Ratio” is the  $\log(F_{\text{obs}}/F_{\text{pred}})$  of the line. “Blends” amounting to more than 5% of the total flux for each line are indicated, with wavelengths in Å.

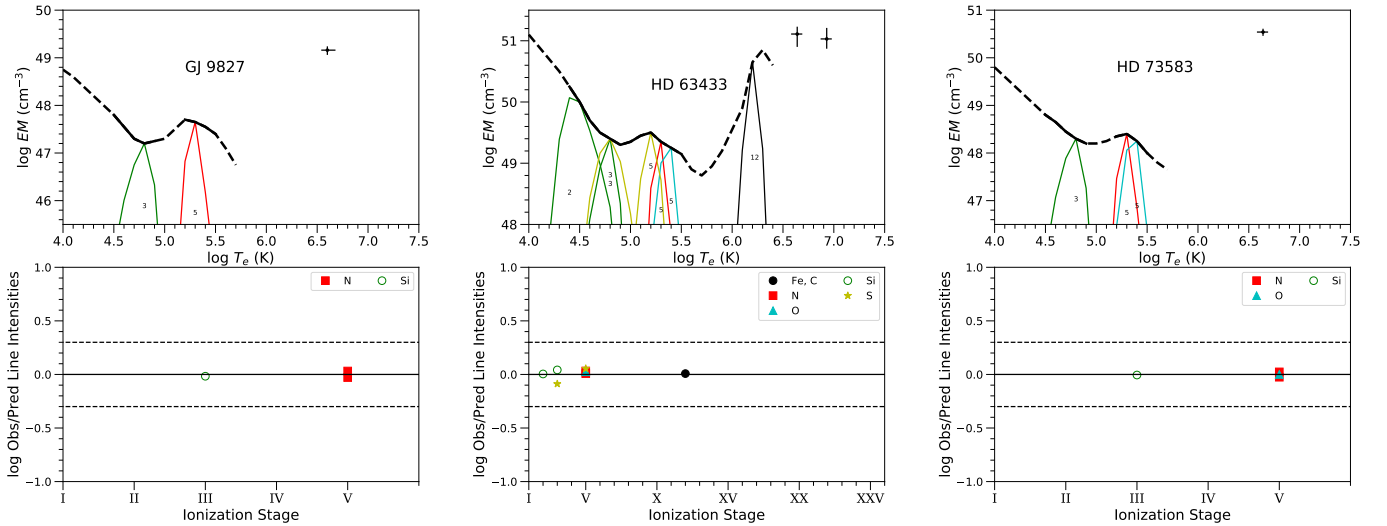


**Fig. D.5.** Same as in Fig. 1 but for GJ 9827, HD 63443 (TOI-1726), and HD 73583 (TOI-560), using HST/STIS data. The 1- $T$  and 2- $T$  global fits to *XMM-Newton*/EPIC spectra are also indicated with error bars.

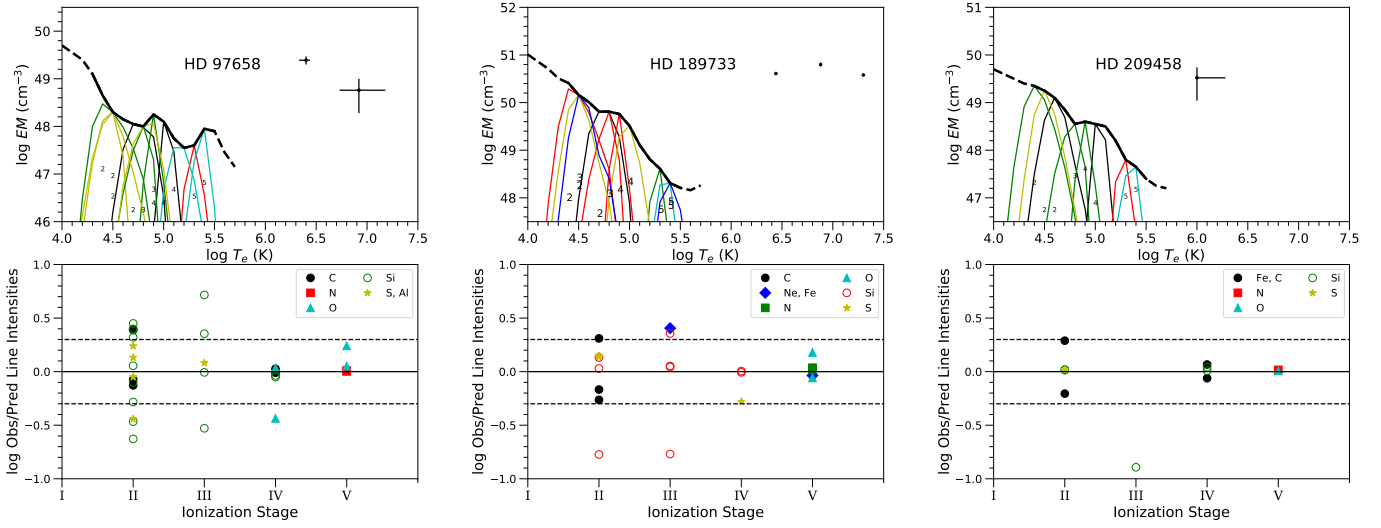


**Fig. D.6.** Same as in Fig. 1 but for HD 97658, HD 189733 and HD 209458, using HST/COS data. HD 209458 COS data taken from France et al. (2010). The 1 to 3- $T$  global fits to XMM-Newton/EPIC spectra are also indicated with error bars.

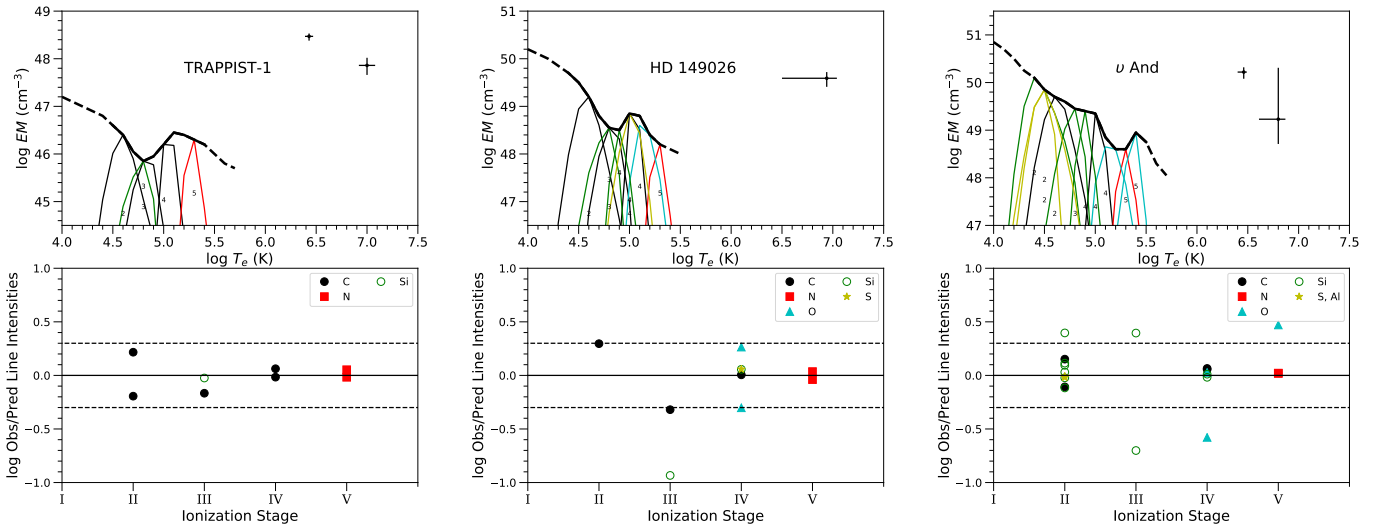


**Fig. D.7.** Emission Measure Distributions as in Fig. 1, using HST/COS (TRAPPIST-1) and HST/STIS (HD 149026 and  $\nu$  And) data. The 1- $T$  and 2- $T$  global fits to XMM-Newton/EPIC spectra are also indicated with error bars.



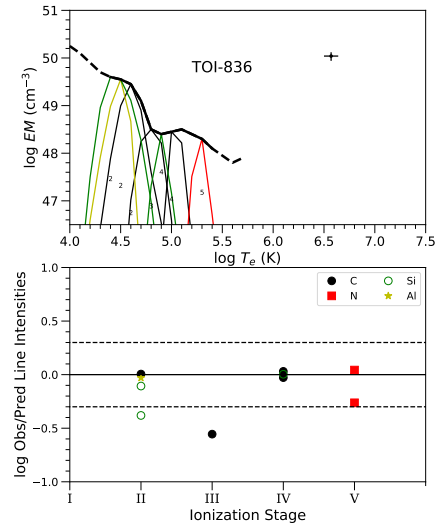


**Fig. D.8.** Same as in Fig. 1 but for TOI-836, using HST/STIS data. The  $1-T$  global fit to XMM-Newton/EPIC spectra is also indicated with error bars.

**Table D.5.** *Chandra*/HETG and LETG, *EUVE*, and *HST*/STIS line fluxes of AD Leo<sup>a</sup>.

Ion	$\lambda_{\text{model}}$ (Å)	$\log T_{\text{max}}$	$F_{\text{obs}}$	$S/N$	Ratio	Blends
S xv	5.0387	7.3	2.51e-14	3.1	-0.46	
Si xiv	6.1804	7.3	6.55e-14	9.3	-0.29	Si xiv 6.1858
Si xiii	6.6479	7.1	9.67e-14	12.2	-0.39	
Si xii	6.6638	7.0	1.06e-14	4.1	-0.01	Si xii 6.6627
Si xiii	6.6882	7.1	2.19e-14	5.8	-0.35	Si xiii 6.6850
Si xiii	6.7403	7.1	6.40e-14	10.7	-0.33	Si xii 6.7432
Mg xi	7.4730	6.9	5.61e-15	3.3	0.12	Fe xxiii 7.4780
Al xii	7.7573	7.0	4.98e-15	3.2	-0.16	
Mg xi	7.8503	6.9	5.57e-15	3.4	-0.20	
Fe xxiv	7.9857	7.4	7.43e-15	4.1	0.37	Fe xxiii 7.9360, Fe xxiv 7.9960
Fe xxiv	8.3161	7.4	4.90e-15	3.3	-0.06	Fe xxi 8.3162, Fe xxiii 8.3038
Mg xi	8.4192	7.1	4.70e-14	10.4	-0.18	Mg xi 8.4246
No id.	8.4577	0.0	4.31e-15	3.1	...	
Fe xxii	8.7140	7.2	6.13e-15	3.7	0.11	Fe xxii 8.7035, 8.7360, Ni xxii 8.7227, Ni xx 8.7286, Ni xix 8.7440
Fe xxii	8.9748	7.2	7.35e-15	3.9	0.24	
Fe xx	9.0659	7.1	6.48e-15	3.3	0.16	Fe xxii 9.0501, 9.0629, Ni xxvi 9.0603, Fe xx 9.0647, 9.0683
Mg xi	9.1687	6.9	4.75e-14	8.0	-0.09	
Mg xi	9.2312	6.9	1.11e-14	3.8	-0.07	Mg xi 9.2282, Fe xxii 9.2298
Ni xix	9.2540	7.0	7.66e-15	3.2	0.19	Ne x 9.2461, 9.2462
Mg xi	9.3143	6.9	2.35e-14	5.6	-0.13	
Ni xx	9.3850	7.1	4.77e-15	3.4	0.51	Ni xxvi 9.3853, Ni xxv 9.3900
No id.	9.4000	0.0	5.99e-15	3.7	...	
Ne x	9.4807	6.9	1.56e-14	5.8	0.02	Ni xx 9.4719, Ne x 9.4809
Ne x	9.7080	6.9	2.09e-14	5.4	-0.16	Ne x 9.7085
Ni xix	9.9770	7.0	8.01e-15	3.6	0.05	Ni xxv 9.9700, Fe xxi 9.9887
No id.	10.0100	0.0	9.21e-15	3.8	...	
Na xi	10.0232	7.0	8.56e-15	3.7	0.00	Fe xx 10.0235, Na xi 10.0286
No id.	10.0500	0.0	6.03e-15	3.1	...	
Ni xix	10.1100	7.0	6.34e-15	3.2	0.15	
Fe xvii	10.1210	6.9	7.94e-15	3.5	0.54	Fe xix 10.1195, 10.1309
Ne x	10.2385	6.9	8.39e-14	11.0	-0.02	Ne x 10.2396
Fe xviii	10.4483	7.0	1.39e-14	4.4	0.26	Fe xx 10.4537, Fe xviii 10.4639, 10.4654, 10.4726
Fe xvii	10.5040	6.9	1.32e-14	4.2	0.34	
Fe xviii	10.5364	7.0	7.42e-15	3.1	-0.07	Fe xviii 10.5382
Fe xxiv	10.6190	7.4	1.29e-14	4.2	-0.11	Fe xix 10.6193
Fe xvii	10.7700	6.9	2.85e-14	6.2	0.23	Fe xix 10.7650, Ne ix 10.7650
Fe xix	10.8160	7.1	7.02e-15	3.1	-0.20	Fe xix 10.8083
Fe xxiii	10.9810	7.3	1.91e-14	4.9	0.08	Fe xx 10.9866
Ne ix	11.0010	6.7	1.26e-14	4.0	-0.08	Fe xx 11.0065
Fe xxiv	11.0290	7.4	1.62e-14	4.5	-0.06	Fe xxiii 11.0190, Fe xvii 11.0260
Fe xvii	11.1310	6.9	2.13e-14	5.0	0.10	Fe xx 11.1415
Fe xxiv	11.1760	7.4	1.43e-14	3.9	-0.04	Fe xxiv 11.1870, Ni xxii 11.1950
Fe xvii	11.2540	6.9	2.17e-14	4.9	-0.02	
Fe xviii	11.3260	7.0	2.40e-14	5.1	-0.07	Fe xviii 11.3260, Ni xxi 11.3180, Fe xxiii 11.3360
Fe xviii	11.4230	7.0	1.71e-14	4.2	-0.27	Fe xxii 11.4270, Fe xviii 11.4274, Fe xxiv 11.4320
Fe xxiii	11.4580	7.3	9.10e-15	3.0	0.18	Fe xviii 11.4445, 11.4471, Fe xxi 11.4451
Fe xxii	11.4900	7.2	9.37e-15	3.2	0.12	Fe xxii 11.4900, 11.5025
Fe xviii	11.5270	7.0	1.79e-14	4.3	-0.07	Fe xviii 11.5270
Ne ix	11.5440	6.7	5.29e-14	7.5	0.10	Ni xix 11.5390
No id.	11.6060	0.0	1.06e-14	3.4	...	
Fe xxiii	11.7360	7.3	3.01e-14	5.5	0.02	
Fe xxii	11.7700	7.2	1.83e-14	4.3	-0.25	Fe xx 11.7620
Fe xxii	11.9320	7.2	1.36e-14	3.7	0.22	Fe xxi 11.9432, Fe xxii 11.9474
Ni xx	12.1120	7.1	1.03e-14	3.1	0.34	Ne ix 12.1110, Fe xxi 12.1147
Ne x	12.1321	6.9	6.32e-13	24.4	0.03	Fe xvii 12.1240, Ne x 12.1375
Fe xxiii	12.1610	7.3	2.10e-14	4.4	0.17	
Fe xxii	12.2100	7.2	1.12e-14	3.2	0.11	Fe xxii 12.2008, Fe xxi 12.2040, Ni xxi 12.2080, Fe xix 12.2120
Fe xvii	12.2660	6.9	3.58e-14	5.7	-0.09	
Fe xxi	12.2840	7.2	3.22e-14	5.4	-0.25	
Ne ix	12.3560	6.8	1.30e-14	3.4	0.12	Fe xxi 12.3508, 12.3527, 12.3626, 12.3628, 12.3630, Fe xxii 12.3648
Fe xxi	12.3930	7.2	1.18e-14	3.2	0.07	
Ni xix	12.4350	7.0	2.16e-14	4.4	-0.39	Fe xxi 12.4220, Fe xx 12.4234, 12.4310
Fe xx	12.4680	7.1	1.25e-14	3.3	0.05	Ni xviii 12.4590, Fe xxi 12.4625, Fe xxii 12.4728, Fe xix 12.4729, 12.4767
Fe xxi	12.4990	7.2	1.16e-14	3.2	0.01	Fe xxi 12.5023, 12.5048, Ni xxi 12.5105
Fe xx	12.5760	7.1	1.40e-14	3.5	0.14	
Ni xix	12.6560	7.0	1.29e-14	3.3	0.02	Fe xxi 12.6490
Ni xix	12.8120	7.0	1.49e-14	3.5	0.29	Fe xxi 12.8071, 12.8089, 12.8095, 12.8110, Mn xxii 12.8109
Fe xx	12.8240	7.1	1.02e-13	9.1	0.01	Fe xxi 12.8220, Fe xx 12.8460
Fe xx	12.9120	7.1	1.15e-14	3.0	-0.22	Fe xix 12.9033, 12.9169
Fe xx	12.9650	7.1	2.16e-14	4.1	-0.15	Fe xviii 12.9494, Fe xxii 12.9530
Fe xix	13.0220	7.1	1.73e-14	3.7	-0.00	Fe xviii 13.0121, Fe xxi 13.0126, Fe xx 13.0152, 13.0240
Fe xx	13.1000	7.1	2.49e-14	4.1	0.46	Fe xix 13.0810, 13.1011, Fe xxi 13.1056
Fe xx	13.1370	7.1	1.87e-14	3.6	0.28	Fe xxi 13.1223, 13.1338, Ni xx 13.1350
Fe xx	13.1530	7.1	1.74e-14	3.5	0.07	Fe xvii 13.1530, Fe xx 13.1565, Ni xx 13.1610
Fe xviii	13.3230	7.0	1.56e-14	3.3	0.02	Ni xx 13.3090, 13.3236, Fe xviii 13.3312
Fe xx	13.3850	7.1	1.68e-14	3.3	-0.16	Fe xviii 13.3550, 13.3807, Fe xx 13.3752, 13.3953
Fe xix	13.4230	7.1	2.32e-14	3.8	0.42	Fe xix 13.4239
Ne ix	13.4473	6.7	4.13e-13	16.2	0.26	
Fe xix	13.4620	7.1	4.72e-14	5.6	0.18	Ne viii 13.4610, 13.4690, 13.4700
Fe xix	13.4970	7.1	2.27e-14	3.9	-0.24	Ne viii 13.4910, Fe xix 13.4923
Fe xix	13.5180	7.1	7.87e-14	7.3	0.01	

**Table D.5.** (continued) *Chandra*/HETG and LETG, *EUVE*, and *HST*/STIS line fluxes of AD Leo<sup>a</sup>.

Ion	$\lambda_{\text{model}}$ (Å)	$\log T_{\text{max}}$	$F_{\text{obs}}$	$S/N$	Ratio	Blends
Ne ix	13.5531	6.7	5.60e-14	6.2	0.08	
Fe xix	13.6450	7.1	2.21e-14	3.7	0.22	Fe xix 13.6442, 13.6476
Ne ix	13.6990	6.7	2.50e-13	12.5	0.24	Fe xix 13.6878, 13.7054
Fe xix	13.7590	7.1	2.39e-14	3.6	0.42	
Ni xix	13.7790	7.0	2.05e-14	3.3	-0.07	Fe xx 13.7670, Fe xix 13.8041, 13.8068
Fe xix	13.7950	7.1	2.86e-14	3.8	-0.04	
Fe xvii	13.8250	6.9	2.03e-14	3.1	-0.17	
Fe xix	13.8390	7.1	1.95e-14	3.0	0.27	Fe xx 13.8430
Fe xviii	13.9530	7.0	4.66e-14	4.5	0.39	Fe xix 13.9263, 13.9330, Fe xx 13.9620
Ni xix	14.0430	7.0	2.29e-14	3.5	-0.21	Fe xix 14.0179, 14.0340, 14.0388
Ni xix	14.0770	7.0	2.94e-14	3.9	0.13	Fe xix 14.0610, Fe xx 14.0620, 14.0784
No id.	14.1736	0.0	1.59e-14	3.0	...	
Fe xviii	14.2080	7.0	1.03e-13	7.8	-0.25	
No id.	14.2492	0.0	2.71e-14	4.0	...	
Fe xviii	14.2560	7.0	3.51e-14	4.6	-0.12	Fe xx 14.2670
Fe xx	14.3259	7.1	1.53e-14	3.3	0.78	Fe xix 14.3275, 14.3391, 14.3397, Fe xx 14.3321, Fe xxi 14.3388
Fe xviii	14.3430	7.0	1.89e-14	3.7	-0.06	
Fe xviii	14.3730	7.0	3.01e-14	4.7	-0.16	
Fe xviii	14.4250	7.0	1.68e-14	3.5	0.17	Fe xix 14.4106
Fe xviii	14.4345	7.0	1.81e-14	3.6	0.31	Fe xviii 14.4432
Fe xx	14.4600	7.1	2.92e-14	4.6	0.14	Fe xviii 14.4610, 14.4555, 14.4769, Fe xx 14.4793
Fe xviii	14.5340	7.0	7.96e-14	7.4	0.03	O viii 14.5242, 14.5243, Fe xviii 14.5608, 14.5710
O viii	14.6342	6.6	1.56e-14	3.2	-0.12	O viii 14.6344
Fe xix	14.6640	7.1	2.12e-14	3.7	-0.01	
Fe xx	14.7540	7.1	1.80e-14	3.5	0.12	Fe xviii 14.7499, 14.7510
O viii	14.8205	6.6	3.20e-14	4.5	-0.11	O viii 14.8207, Fe xx 14.8304
Fe xvii	15.0140	6.9	3.77e-13	14.5	0.04	
Fe xvi	15.0496	6.7	3.54e-14	4.5	0.31	Fe xx 15.0470, 15.0470
Fe xix	15.0790	7.1	3.48e-14	4.5	0.12	
O viii	15.1760	6.6	7.73e-14	6.4	-0.08	O viii 15.1765, Fe xix 15.1770
Fe xix	15.1980	7.1	3.25e-14	4.1	0.27	Fe xviii 15.1898
Fe xvii	15.2610	6.9	1.77e-13	9.5	0.21	
Fe xvii	15.4530	6.8	2.87e-14	3.9	0.23	
Fe xviii	15.4940	7.0	1.78e-14	3.1	0.32	Fe xvi 15.4955, 15.5023, Cr xviii 15.5020
Fe xviii	15.6250	7.0	3.51e-14	4.4	-0.17	
Fe xviii	15.8240	7.0	3.53e-14	4.4	0.05	
Fe xviii	15.8700	7.0	2.36e-14	3.6	0.04	Fe xix 15.8708
O viii	16.0055	6.6	2.61e-13	11.6	-0.02	Fe xviii 16.0040, O viii 16.0067
Fe xviii	16.0710	7.0	1.10e-13	7.5	0.09	
No id.	16.7276	0.0	2.07e-14	3.0	...	
Fe xvii	16.7800	6.8	2.38e-13	10.1	0.04	
Fe xvii	17.0510	6.8	3.27e-13	11.4	0.10	
Fe xvii	17.0960	6.8	2.56e-13	10.0	0.11	
Fe xviii	17.6230	7.0	2.73e-14	3.1	-0.24	
O vii	18.6270	6.4	7.76e-14	4.9	0.03	Ar xvi 18.6324
O viii	18.9671	6.6	1.38e-12	19.0	0.01	O viii 18.9725
O vii	21.6015	6.4	4.51e-13	8.1	-0.00	
O vii	21.8036	6.4	1.12e-13	3.8	0.08	
O vii	22.0977	6.4	1.93e-13	4.7	-0.19	
N vii	24.7792	6.4	1.51e-13	4.6	-0.25	N vii 24.7846
C vi	28.4652	6.3	3.96e-14	6.5	0.18	C vi 28.4663
N vi	28.7870	6.3	3.67e-14	6.2	-0.19	
N vi	29.0843	6.2	3.27e-14	5.8	0.38	
N vi	29.5347	6.2	3.86e-14	6.2	0.01	Si xii 29.5090
S xiv	30.4270	6.6	3.65e-14	5.6	0.12	
S xiv	30.4690	6.6	1.52e-14	3.7	0.04	
S xiii	32.2391	6.6	2.90e-14	5.5	0.39	S xiii 32.1911
S xiv	32.5600	6.6	4.60e-14	6.9	0.09	S xiv 32.5750
S xiv	33.5490	6.6	4.68e-14	6.9	0.36	Si xi 33.5301
C vi	33.7342	6.2	2.61e-13	16.3	0.21	C vi 33.7396
Si xi	43.7501	6.4	2.34e-14	7.8	0.03	
Si xii	44.0190	6.4	3.07e-14	9.1	0.01	
Si xii	44.1650	6.4	5.73e-14	12.4	0.03	
Si xii	45.5210	6.4	2.44e-14	8.1	0.24	
Si xii	45.6910	6.4	2.58e-14	8.4	-0.03	
Fe xvi	50.3613	6.6	8.09e-15	4.3	0.00	
Fe xvi	54.1264	6.6	1.46e-14	4.2	0.12	S viii 54.1181, S ix 54.1750
Fe xvi	54.7101	6.6	1.98e-14	4.9	0.21	Fe xvi 54.7472
Mg x	57.8760	6.2	8.36e-15	4.2	0.15	
Fe xvi	63.7106	6.6	8.70e-15	3.0	-0.22	
Mg x	65.8450	6.2	1.59e-14	5.3	0.48	Ne viii 65.8940
Fe xvi	66.3568	6.6	4.83e-14	9.7	0.36	Fe xvi 66.2489
Ne viii	88.0820	5.9	3.59e-14	13.2	0.24	Ne viii 88.1190
Fe vii	89.8267	6.3	1.40e-14	7.3	0.39	Fe xii 89.4789, Fe xvii 89.5977, Ne vii 89.9472
Fe xix	91.0200	7.0	1.77e-14	8.4	0.06	Fe xvii 90.5205, Fe xx 90.6000, Fe x 90.6830, Fe xiii 90.7058, Fe xi 90.7197
Fe xiv	92.4616	6.4	7.45e-15	4.3	0.17	Fe xvii 92.0282, Fe xiv 92.0572, Fe xi 92.7554
Fe xviii	93.9230	7.0	7.72e-14	23.2	-0.07	
Ne viii	98.2600	5.9	6.45e-14	20.9	0.19	Fe xxi 97.8800, Ne viii 98.1150
Fe xix	101.5500	7.0	1.17e-14	6.7	-0.37	
Fe xxi	102.2200	7.2	3.05e-14	14.0	-0.14	Fe xiii 102.0757, O viii 102.3476, 102.3552, 102.3919, 102.4897, 102.5497
Ne viii	103.0850	5.9	1.57e-14	8.9	0.14	Ni xxii 103.3260, Fe xiii 103.3386
Fe xviii	103.9370	7.0	2.27e-14	11.3	-0.12	
O vi	104.8130	5.6	7.03e-15	5.9	0.55	O vi 104.8129, Fe xvii 104.7669

**Table D.5.** (continued) *Chandra*/HETG and LETG, *EUVE*, and *HST*/STIS line fluxes of AD Leo<sup>a</sup>.

Ion	$\lambda_{\text{model}}$ (Å)	$\log T_{\text{max}}$	$F_{\text{obs}}$	$S/N$	Ratio	Blends
Ni xxii	106.0640	7.2	7.74e-15	6.0	-0.02	Fe xii 106.0264, 106.0341, 106.2027, Fe xix 106.1200, 106.3300
Fe xix	108.3700	7.0	5.02e-14	19.4	-0.16	
Fe xix	109.9700	7.0	6.86e-15	5.7	-0.27	
Fe xx	110.6300	7.1	6.43e-15	4.5	0.09	Fe xx 110.4464
Fe xix	111.7000	7.0	8.00e-15	5.2	-0.20	Ni xxiii 111.8600
Fe xxii	114.4100	7.2	1.32e-14	7.8	0.10	Fe xii 114.5616, 114.9055
Mn xviii	115.3653	7.0	1.04e-14	7.2	0.09	
Fe xxii	117.1700	7.2	5.58e-14	19.6	-0.01	Fe xxi 117.5100
Ni xxv	117.9330	7.4	7.41e-15	5.7	0.04	Ni xxii 117.9330, Cr xx 117.9580
Fe xx	118.6600	7.1	1.49e-14	8.5	-0.18	
Fe xix	120.0000	7.0	1.51e-14	8.0	-0.22	O vii 120.3310, O vii 120.3327
Fe xx	121.8300	7.1	3.60e-14	14.1	-0.08	
Ne vi	122.4879	5.8	6.45e-15	4.5	0.08	Ne vi 122.6850, Cr xvii 122.9718
Fe xxi	128.7300	7.2	5.59e-14	17.2	0.00	
Fe xxiii	132.8500	7.3	1.65e-13	30.6	0.04	Fe xx 132.8500
Fe xxii	135.7800	7.2	4.26e-14	14.3	0.02	
Fe xxi	142.2700	7.2	1.87e-14	8.1	0.28	Fe xxi 142.1600
Fe ix	171.0729	6.0	5.97e-14	9.9	-0.10	Ni xiv 171.3703
Fe x	174.5310	6.1	6.07e-14	8.6	-0.00	
Fe xi	180.4080	6.2	2.41e-14	6.1	-0.69	
Fe xii	193.5090	6.3	2.02e-13	19.1	-0.28	S xi 191.2664, Fe xxiv 192.0170, Fe xii 192.3940, 195.1190
Fe xiii	203.8280	6.3	5.00e-14	9.2	0.23	Ar xiv 203.3510, Fe xii 203.7280, Mn xi 203.9122, Fe xi 204.7440, Fe xiii 204.9450
Fe xiv	211.3180	6.4	6.67e-14	10.2	-0.28	
Ni xvii	249.1780	6.6	5.20e-14	7.1	0.30	Fe xii 248.7670, 249.3880
Fe xv	284.1630	6.4	2.38e-13	15.4	-0.13	
Fe xvi	335.4098	6.5	2.59e-13	12.7	-0.04	Fe xiv 334.1800
Fe xvi	360.7581	6.5	1.09e-13	6.6	-0.07	Fe xiii 359.6420, 359.8420
C iii	1176.0000	4.8	1.93e-13	20.4	0.06	
S iii	1190.1990	4.9	9.87e-16	8.2	-0.64	
S iii	1194.0490	4.9	2.21e-15	10.7	-0.19	
Si ii	1194.5010	4.6	3.38e-15	13.6	-0.27	S iii 1194.4430
Si ii	1197.3950	4.6	2.14e-15	27.6	0.00	
S v	1199.1360	5.3	2.13e-15	9.1	-0.04	
S iii	1200.9610	4.9	4.52e-15	23.4	0.16	
O ii	1204.2345	4.9	5.35e-16	4.9	-0.19	
Si iii	1206.5019	4.9	1.29e-13	56.2	-0.29	
O v	1218.3440	5.5	2.63e-14	78.3	-0.13	
N v	1238.8218	5.4	9.23e-14	79.2	0.12	
Fe xii	1242.0050	6.3	2.28e-15	25.8	0.38	
N v	1242.8042	5.4	4.50e-14	41.2	0.11	
C iii	1247.3830	5.1	1.88e-15	17.6	-0.24	
Ne ix	1248.1030	6.7	6.81e-16	32.1	0.03	
S ii	1250.5870	4.6	1.05e-15	22.1	-0.05	
S ii	1253.8130	4.6	1.69e-15	19.9	-0.15	
S ii	1259.5210	4.6	2.40e-15	31.8	-0.22	
Si ii	1264.7400	4.5	7.76e-15	24.2	0.31	
Si ii	1265.0040	4.6	3.82e-15	19.5	0.19	
Si ii	1304.3719	4.6	2.89e-15	21.5	0.33	
Si ii	1309.2770	4.6	5.77e-15	35.4	0.33	
Si iii	1312.5930	4.9	8.90e-16	14.3	-0.47	
C ii	1323.9080	4.8	2.22e-15	18.3	0.39	
Fe xix	1328.6999	7.1	1.82e-15	13.8	-0.08	
C ii	1334.5350	4.7	5.16e-14	41.6	-0.29	
C ii	1335.7100	4.7	1.59e-13	64.2	0.54	
O iv	1338.6140	5.3	4.70e-16	13.4	0.02	
Fe xii	1349.4000	6.3	8.71e-16	16.8	0.20	
Fe xxi	1354.0800	7.2	7.30e-15	12.5	-0.08	
O v	1371.2960	5.5	5.97e-15	25.3	-0.16	
Ar xi	1392.0980	6.4	1.10e-15	24.2	-0.02	
Si iv	1393.7552	5.0	1.09e-13	52.0	0.19	
Si iv	1402.7704	5.0	6.32e-14	35.6	0.25	
Si iii	1417.2400	4.9	8.94e-16	23.1	0.34	
Si viii	1445.7371	6.0	4.82e-16	9.1	-0.20	
S v	1501.7660	5.3	1.19e-15	19.5	-0.19	
Si ii	1526.7090	4.5	8.05e-15	21.8	0.33	
Si ii	1533.4320	4.5	1.40e-14	20.5	0.28	
C iv	1548.1871	5.1	3.54e-13	64.5	-0.09	
C iv	1550.7723	5.1	1.93e-13	48.7	-0.05	
Ne v	1574.7560	5.5	1.31e-15	15.2	0.36	
S xi	1614.4946	6.4	1.23e-15	8.8	0.27	
O vii	1623.6672	6.4	2.41e-15	12.4	0.08	
S iv	1629.1550	5.2	1.03e-15	10.7	0.33	
Al ii	1670.7870	4.6	1.52e-14	17.9	0.22	

**Notes.** <sup>(a)</sup> Line fluxes (in erg cm<sup>-2</sup> s<sup>-1</sup> units) measured in the spectra, and corrected by the ISM absorption when needed.  $\log T_{\text{max}}$  (K) indicates the maximum temperature of formation of the line (unweighted by the EMD). “Ratio” is the log ( $F_{\text{obs}}/F_{\text{pred}}$ ) of the line. “Blends” amounting to more than 5% of the total flux for each line are indicated, with wavelengths in Å.

**Table D.6.** *XMM-Newton*/RGS and HST/STIS line fluxes of Lalande 21185<sup>a</sup>.

Ion	$\lambda_{\text{model}}$ (Å)	$\log T_{\text{max}}$	$F_{\text{obs}}$	$S/N$	Ratio	Blends
Si xiv	6.1804	7.3	2.47e-14	3.8	0.02	Si xiv 6.1858
Ne x	10.2385	6.9	5.38e-15	3.9	0.20	Ne x 10.2396
No id.	10.5040	0.0	5.56e-15	4.0	...	
No id.	10.7700	0.0	6.84e-15	4.6	...	
Ne ix	11.5440	6.7	4.38e-15	3.9	0.16	Fe xxii 11.4900, Fe xviii 11.5270
Ne x	12.1321	6.9	1.92e-14	8.5	-0.10	Fe xvii 12.1240, Ne x 12.1375
Fe xvi	12.5399	6.8	2.64e-15	3.2	0.29	Fe xxi 12.4990, 12.5048, Fe xx 12.5260, 12.5760, Fe xvii 12.5391
Ne ix	13.4473	6.7	3.23e-14	11.8	0.21	Fe xix 13.4970, 13.5180, Ne ix 13.5531
Ne ix	13.6990	6.7	5.52e-15	4.1	-0.13	Fe xix 13.6450, 13.7054
Fe xvii	13.8250	6.9	7.16e-15	5.6	0.26	Fe xix 13.7590, 13.7950, 13.8390, Fe xx 13.7670, Ni xix 13.7790, Fe xvii 13.8920
Fe xviii	14.2080	7.0	4.78e-15	4.7	-0.24	Fe xviii 14.2560, Fe xx 14.2670
Fe xviii	14.3730	7.0	5.79e-15	5.1	0.14	Fe xviii 14.3430, 14.3990, 14.4250, 14.4555
Fe xviii	14.5340	7.0	2.17e-15	3.1	-0.12	O viii 14.5242, 14.5243, Fe xviii 14.5608, 14.5710
Fe xvi	14.9555	6.7	3.70e-15	4.1	-0.08	O viii 14.8205, 14.8207, Fe xix 14.9610
Fe xvii	15.0140	6.9	1.50e-14	8.3	-0.02	
O viii	15.1760	6.6	3.15e-15	3.8	-0.20	O viii 15.1765, Fe xix 15.1980
Fe xvii	15.2610	6.9	4.38e-15	4.5	-0.02	
Fe xvii	15.4530	6.8	3.60e-15	4.1	0.41	Fe xvi 15.4485, 15.4533, 15.5023, Fe xviii 15.4940, Fe xx 15.5170
O viii	16.0055	6.6	1.60e-14	8.4	0.07	Fe xviii 16.0040, O viii 16.0067
Fe xix	16.2830	7.1	3.24e-15	3.9	0.36	Fe xvii 16.2285, 16.3500, Fe xix 16.2857, 16.3247, Fe xviii 16.3200
Fe xvii	16.7800	6.8	1.11e-14	7.2	0.11	
Fe xvii	17.0510	6.8	1.59e-14	8.5	-0.13	Fe xvii 17.0960
Fe xviii	17.6230	7.0	1.86e-15	3.0	0.03	
O vii	18.6270	6.4	6.27e-15	5.5	0.14	Ar xvi 18.6324, Ca xviii 18.6909
O viii	18.9671	6.6	6.88e-14	18.1	-0.01	O viii 18.9725
O vii	21.6015	6.4	3.61e-14	12.3	0.19	
O vii	21.8036	6.4	2.41e-15	3.2	-0.16	
O vii	22.0977	6.4	2.38e-14	9.9	0.18	
No id.	23.0050	0.0	4.01e-15	3.6	...	
N vii	24.7792	6.4	5.49e-15	5.1	-0.28	Ar xv 24.7366, 24.7400, N vii 24.7846, Ar xvi 24.8509
C vi	26.9896	6.3	2.88e-15	3.5	-0.21	C vi 26.9901, Ar xv 27.0432
Ar xiv	27.4640	6.7	3.11e-15	3.6	-0.17	Ar xiv 27.6310, 27.6360
Ar xiii	29.1420	6.6	4.95e-15	4.2	0.10	
S xiv	30.4270	6.6	3.88e-15	3.5	-0.09	Ca xi 30.4480, S xiv 30.4690
S xiv	32.5600	6.6	4.02e-15	3.4	0.06	S xiv 32.5750, Ca xii 32.6571
C vi	33.7342	6.2	3.44e-14	10.0	0.23	C vi 33.7396
No id.	35.6844	0.0	5.70e-15	3.8	...	
O v	1218.3440	5.5	2.51e-15	4.4	0.06	
N v	1238.8218	5.4	2.55e-15	4.1	0.14	
N v	1242.8042	5.4	1.47e-15	3.0	0.20	
Si ii	1264.7400	4.5	3.90e-16	4.2	0.06	
C ii	1335.7100	4.7	4.12e-15	5.6	-0.22	C ii 1335.6650
O v	1371.2960	5.5	2.96e-16	3.4	-0.28	
Si iv	1393.7552	5.0	4.73e-15	5.2	0.02	
O iv	1401.1570	5.3	5.89e-16	3.0	-0.48	
Si iv	1402.7704	5.0	1.61e-15	5.4	-0.15	
Si ii	1533.4320	4.5	4.96e-16	3.2	-0.06	
C iv	1548.1871	5.1	1.66e-14	8.1	-0.00	
C iv	1550.7723	5.1	7.85e-15	5.6	-0.03	
Al ii	1670.7870	4.6	4.41e-15	3.1	-0.02	

**Notes.** <sup>(a)</sup> Line fluxes (in erg cm<sup>-2</sup> s<sup>-1</sup> units) measured in the spectra, and corrected by the ISM absorption when needed.  $\log T_{\text{max}}$  (K) indicates the maximum temperature of formation of the line (unweighted by the EMD). “Ratio” is the  $\log (F_{\text{obs}}/F_{\text{pred}})$  of the line. “Blends” amounting to more than 5% of the total flux for each line are indicated, with wavelengths in Å.

**Table D.7.** *XMM-Newton*/RGS, HST/COS, and STIS line fluxes of GJ 674<sup>a</sup>.

Ion	$\lambda_{\text{model}}$ (Å)	$\log T_{\text{max}}$	$F_{\text{obs}}$	$S/N$	Ratio	Blends
Fe xxiii	11.7360	7.3	2.86e-15	3.1	-0.39	
Fe xxii	11.9770	7.2	6.49e-15	4.8	0.22	Fe xxii 11.8810, 11.9320, 11.9474, Fe xxii 11.9023, 11.9750, Ni xx 11.9617
Ne x	12.1321	6.9	2.24e-14	9.0	-0.11	Fe xvii 12.1240, Ne x 12.1375, Fe xxiii 12.1610
Fe xxii	12.2840	7.2	2.51e-15	3.0	-0.79	Fe xvii 12.2660
Ne ix	13.4473	6.7	2.15e-14	9.4	-0.16	Fe xix 13.4620, 13.4970, 13.5180, Fe xxii 13.5070
Ne ix	13.6990	6.7	1.93e-14	9.0	0.41	Fe xix 13.6450, 13.6878, 13.7054
Fe xviii	14.2080	7.0	1.01e-14	6.5	-0.33	Fe xviii 14.2560, Fe xx 14.2670
Fe xviii	14.3730	7.0	3.14e-15	3.6	-0.55	Fe xviii 14.3430, 14.3430, 14.3990, 14.4250, 14.4555, Fe xx 14.3887
Fe xviii	14.5340	7.0	6.56e-15	5.3	0.02	O viii 14.5242, Fe xviii 14.5608, 14.5710
Fe xvi	14.9555	6.7	4.92e-15	4.6	-0.26	O viii 14.8205, 14.8207, Fe xx 14.8791, 14.9279, Fe xix 14.9610, 14.9632
Fe xvii	15.0140	6.9	1.69e-14	8.6	-0.11	
Fe xix	15.0790	7.1	7.77e-15	5.8	0.38	
O viii	15.1760	6.6	5.02e-15	4.6	-0.17	O viii 15.1765, Fe xix 15.1980
Fe xvii	15.2610	6.9	9.26e-15	6.3	0.16	
O viii	16.0055	6.6	1.89e-14	9.2	-0.13	Fe xviii 16.0040, 16.0710, O viii 16.0067
Fe xvii	16.7800	6.8	7.27e-15	5.7	-0.19	
Fe xvii	17.0510	6.8	3.35e-14	12.2	0.08	Fe xvii 17.0960
O viii	18.9671	6.6	9.82e-14	20.8	0.15	O viii 18.9725
O vii	21.6015	6.4	5.02e-14	14.1	0.13	
O vii	21.8036	6.4	5.34e-15	4.6	-0.08	
O vii	22.0977	6.4	2.14e-14	9.1	-0.12	
N vii	24.7792	6.4	6.15e-15	5.1	-0.25	N vii 24.7846, N vi 24.8980
C vi	33.7342	6.2	4.45e-14	9.9	0.48	C vi 33.7396
Si iii	1108.3610	4.9	1.13e-15	3.8	0.20	
Si iii	1109.9720	4.9	2.22e-15	5.3	0.13	Si iii 1109.9430
Si iii	1113.2321	4.9	3.00e-15	7.1	0.06	Si iii 1113.2061
Fe xix	1118.0700	7.0	1.07e-15	4.9	0.18	
Si iv	1122.4852	5.0	1.74e-15	4.9	0.53	
Si iv	1128.3405	5.0	2.74e-15	6.2	0.41	Si iv 1128.3252
Ne v	1136.5081	5.5	2.01e-16	3.6	0.02	
Fe iii	1141.7170	4.6	1.69e-16	3.9	0.45	
Ne v	1145.5959	5.5	4.22e-16	4.2	-0.11	
C iii	1176.0000	4.8	5.24e-14	21.6	-0.01	
C iii	1176.0000	4.8	1.74e-14	4.1	-0.49	
S iii	1190.1990	4.9	4.99e-16	8.4	-0.36	
Si ii	1190.4170	4.6	4.62e-16	6.5	0.30	
Si ii	1193.2910	4.6	4.15e-16	6.7	-0.53	
S iii	1194.4430	4.9	1.65e-15	8.6	-0.01	S iii 1194.0490
Si ii	1197.3950	4.6	3.62e-16	6.7	-0.29	
S v	1199.1360	5.3	2.87e-16	6.6	-0.08	
S iii	1200.9611	4.9	1.41e-15	12.8	0.22	
S iii	1201.7200	4.9	3.78e-16	6.1	0.19	
O ii	1204.2345	4.9	3.66e-16	9.5	0.04	
Si iii	1206.5019	4.9	3.15e-14	33.6	-0.68	
N v	1238.8218	5.4	1.51e-14	24.4	0.09	
Fe xii	1242.0050	6.3	4.22e-16	8.1	0.18	
N v	1242.8042	5.4	7.54e-15	19.5	0.09	
C iii	1247.3830	5.1	1.08e-15	10.9	0.24	
S ii	1250.5870	4.6	3.57e-16	4.7	0.18	
S ii	1253.8130	4.6	4.03e-16	4.8	-0.07	
S ii	1259.5210	4.6	6.18e-16	7.2	-0.12	
Si ii	1260.4239	4.6	1.02e-15	7.2	-0.59	
Si ii	1264.7400	4.5	1.59e-15	10.8	0.16	
Si ii	1265.0040	4.6	7.76e-16	8.6	-0.00	
Si iii	1303.3250	4.9	1.76e-15	13.6	0.76	
Si ii	1304.3719	4.6	4.96e-16	9.5	0.09	
Si ii	1309.2770	4.6	1.02e-15	7.9	0.11	
Si iii	1312.5930	4.9	4.14e-16	5.2	-0.54	
C ii	1323.9080	4.8	6.49e-16	6.0	0.02	C ii 1323.8640, 1323.9540
Fe xix	1328.7000	7.1	2.69e-16	5.2	0.03	
C ii	1334.5350	4.7	1.83e-14	21.4	-0.22	
C ii	1335.7100	4.7	2.98e-14	27.4	0.19	C ii 1335.6650
O iv	1338.6140	5.3	1.49e-16	3.5	0.12	
Fe xxii	1354.0800	7.2	1.22e-15	5.3	-0.08	
Si iv	1393.7552	5.0	1.14e-14	3.3	-0.37	
Si iv	1402.7704	5.0	7.65e-15	3.2	-0.24	
Si ii	1526.7090	4.5	1.51e-15	8.6	0.19	
Si ii	1533.4320	4.5	1.63e-15	5.7	-0.08	
C iv	1548.1871	5.1	3.53e-14	4.7	-0.20	
C iv	1550.7723	5.1	2.29e-14	9.4	-0.08	
Al ii	1670.7870	4.6	4.14e-15	11.3	-0.00	

**Notes.** <sup>(a)</sup> Line fluxes (in  $\text{erg cm}^{-2} \text{s}^{-1}$ ) measured in the spectra, and corrected by the ISM absorption when needed.  $\log T_{\text{max}}$  (K) indicates the maximum temperature of formation of the line (unweighted by the EMD). “Ratio” is the  $\log (F_{\text{obs}}/F_{\text{pred}})$  of the line. “Blends” amounting to more than 5% of the total flux for each line are indicated, with wavelengths in Å.

**Table D.8.** HST/COS and STIS line fluxes of 55 Cnc, HD 97658, Barnard’s star, HD 189733, and  $\nu$  And<sup>a</sup>.

Ion	$\lambda_{\text{model}}$ (Å)	$\log T_{\text{max}}$ (K)	55 Cnc			HD 97658			Barnard’s star			HD 189733			$\nu$ And			Blends
			S/N	$F_{\text{obs}}$	Ratio	S/N	$F_{\text{obs}}$	Ratio	S/N	$F_{\text{obs}}$	Ratio	S/N	$F_{\text{obs}}$	Ratio	S/N	$F_{\text{obs}}$	Ratio	
Si III	1113.2060	4.9	...	...	...	...	...	...	5.2	1.05e-16	0.24	...	...	...	...	...	...	...
Ne V	1145.5959	5.5	...	...	...	...	...	...	3.5	1.92e-16	-0.01	4.5	7.09e-17	-0.04	...	...	...	...
C III	1176.0000	4.8	22.4	8.21e-15	-0.11	...	...	...	6.9	5.08e-15	-0.16	...	...	...	...	...	...	...
S III	1190.1990	4.9	...	...	...	40.4	5.19e-17	0.08	...	...	...	...	...	...	...	...	...	Si II 1190.4170
Si II	1193.2910	4.6	9.5	3.78e-16	-0.54	23.7	3.71e-17	-0.47	...	...	...	...	...	...	...	...	...	...
Si II	1194.5010	4.6	16.4	8.66e-16	-0.08	15.7	8.23e-17	-0.10	...	...	...	...	...	...	...	...	...	Si III 1194.4430
Si II	1197.3950	4.6	18.9	3.33e-16	-0.29	13.2	2.79e-17	-0.28	...	...	...	...	...	...	...	...	...	...
S V	1199.1360	5.3	5.7	2.45e-16	0.43	...	...	...	...	...	...	...	...	...	...	...	...	...
S III	1200.9611	4.9	14.8	2.62e-16	0.03	...	...	...	...	...	...	...	...	...	...	...	...	...
S II	1204.3260	4.6	13.8	1.96e-16	1.08	...	...	...	...	...	...	...	...	...	...	...	...	O II 1204.2345
Si III	1206.5019	4.9	50.3	1.67e-14	-0.77	18.0	1.51e-15	-0.53	8.0	4.00e-15	-0.80	39.9	1.10e-14	-0.77	11.9	7.86e-14	-0.70	...
O V	1218.3440	5.5	28.1	2.24e-15	0.36	21.2	1.81e-16	0.24	...	...	...	39.8	2.19e-15	0.18	12.3	1.06e-14	0.47	...
N V	1238.8218	5.4	25.2	3.07e-15	-0.00	14.4	2.10e-16	0.01	10.9	2.80e-15	0.01	25.9	3.32e-15	0.04	5.2	9.82e-15	0.02	...
Fe XII	1242.0050	6.3	18.1	3.70e-16	0.10	...	...	...	5.4	1.25e-16	0.01	...	...	...	...	...	...	...
N V	1242.8042	5.4	26.3	1.60e-15	0.02	11.4	1.03e-16	0.00	8.9	1.46e-15	0.03	17.6	1.58e-15	0.01	5.9	4.87e-15	0.02	...
C III	1247.3831	5.1	...	...	...	...	...	...	5.2	5.52e-17	-0.10	...	...	...	...	...	...	...
Si II	1250.5870	4.6	13.9	1.17e-16	0.03	12.7	1.82e-17	0.24	...	...	...	...	...	...	...	...	...	...
S II	1253.8130	4.6	12.8	2.32e-16	0.02	8.5	2.87e-17	0.13	...	...	...	9.6	1.56e-16	0.14	...	...	...	...
S II	1259.5210	4.6	18.1	3.94e-16	0.02	9.8	1.28e-17	-0.44	3.8	6.93e-17	-0.02	11.7	2.70e-16	0.15	5.5	2.07e-15	-0.02	...
Si II	1260.4239	4.6	16.0	1.07e-15	-0.53	...	...	...	5.3	1.37e-16	-0.55	...	...	...	...	...	...	...
Si II	1260.4240	4.6	...	...	...	11.0	7.44e-17	-0.63	...	...	...	15.2	5.00e-16	-0.77	...	...	...	...
Si II	1264.7400	4.5	27.0	3.48e-15	0.30	10.3	2.68e-16	0.45	5.8	1.48e-16	0.07	18.5	1.95e-15	0.13	5.4	5.95e-15	0.03	Si II 1265.0040
Si II	1265.0040	4.6	...	...	...	8.9	1.30e-16	0.32	5.0	8.80e-17	-0.04	...	...	...	4.3	2.89e-15	-0.12	...
Si III	1294.5480	4.9	8.8	1.15e-16	0.27	4.0	1.64e-17	0.72	5.2	5.95e-17	0.55	...	...	...	...	...	...	...
Si III	1296.7280	4.9	8.8	8.62e-17	-0.26	4.5	7.82e-18	-0.01	...	...	...	6.6	1.13e-16	0.05	...	...	...	...
Si III	1298.9480	4.9	18.1	5.00e-16	0.43	7.7	3.45e-17	0.35	5.7	1.87e-16	0.36	7.4	4.36e-16	0.36	5.3	2.92e-15	0.40	Si III 1296.7280, 1298.8940
Si III	1301.1510	4.9	14.0	2.40e-16	0.66	...	...	...	4.2	4.58e-17	0.50	...	...	...	...	...	...	...
Si III	1303.3249	4.9	15.9	1.58e-16	-0.09	...	...	...	...	...	...	...	...	...	...	...	...	...
Si III	1303.3250	4.9	...	...	...	...	...	...	...	...	...	7.9	1.36e-16	0.04	...	...	...	...
Si II	1304.3719	4.6	25.5	1.45e-15	0.59	...	...	...	4.5	3.52e-17	-0.12	...	...	...	6.3	1.90e-15	-0.02	...
Si II	1309.2770	4.6	16.2	9.76e-16	0.12	9.7	7.66e-17	0.05	5.2	1.02e-16	0.04	11.0	6.49e-16	0.03	11.5	4.92e-15	0.09	...
C II	1323.9080	4.8	11.3	7.60e-17	-0.31	5.7	1.29e-17	-0.13	...	...	...	5.9	9.90e-17	-0.26	...	...	...	C II 1323.8640, 1323.9540
Fe XIX	1328.7000	7.1	8.6	1.63e-16	0.04	...	...	...	...	...	...	...	...	...	...	...	...	...
C II	1334.5350	4.7	47.5	1.04e-14	0.00	11.3	8.59e-16	-0.15	12.9	2.61e-15	-0.20	33.6	8.96e-15	-0.17	14.6	5.41e-14	-0.19	...
C II	1335.7100	4.7	56.4	1.78e-14	0.43	20.9	1.94e-15	0.39	16.2	4.48e-15	0.24	42.8	1.72e-14	0.31	14.5	7.56e-14	0.15	C II 1334.5350, 1335.6650
Fe XII	1349.4000	6.3	20.4	1.50e-16	-0.06	...	...	...	...	...	...	...	...	...	...	...	...	...
Fe XXI	1354.0800	7.2	...	...	...	...	...	...	7.3	4.54e-16	0.02	...	...	...	...	...	...	...
Fe III	1364.2950	4.6	...	...	...	...	...	...	...	...	...	9.8	1.53e-16	0.41	...	...	...	...
O V	1371.2960	5.5	20.3	2.16e-16	-0.11	11.1	3.28e-17	0.05	...	...	...	11.2	2.96e-16	-0.06	...	...	...	...
Si IV	1393.7552	5.0	38.5	9.08e-15	0.10	14.1	7.68e-16	-0.04	26.6	3.38e-15	0.04	25.8	6.91e-15	-0.01	17.3	4.03e-14	-0.02	...
O IV	1397.2310	5.3	7.3	3.52e-17	-0.17	...	...	...	...	...	...	...	...	...	...	...	...	...
O IV	1399.7800	5.3	20.7	1.26e-16	-0.07	...	...	...	...	...	...	...	...	...	...	...	...	...
O IV	1401.1570	5.3	28.5	5.94e-16	0.32	6.8	7.37e-17	0.03	...	...	...	...	...	...	7.2	3.46e-15	0.03	...
Si IV	1402.7704	5.0	30.1	4.61e-15	0.11	11.7	3.71e-16	-0.05	22.2	2.42e-15	-0.39	20.1	3.55e-15	0.00	15.3	2.16e-14	0.01	O IV 1399.7800, 1401.1570, 1404.8060
O IV	1404.8060	5.3	14.4	2.35e-16	-0.23	24.4	3.87e-17	-0.44	...	...	...	...	...	...	7.2	1.31e-15	-0.58	Si IV 1404.8080
Si IV	1406.0160	5.1	28.4	6.83e-17	-0.42	...	...	...	...	...	...	5.8	6.40e-17	-0.28	...	...	...	...
O IV	1407.3820	5.3	22.1	1.10e-16	-0.12	...	...	...	...	...	...	...	...	...	...	...	...	...
Si II	1526.7090	4.5	...	...	...	5.8	2.36e-16	0.40	...	...	...	...	...	...	11.4	1.27e-14	0.40	...
Si II	1533.4320	4.5	...	...	...	5.5	4.68e-16	0.40	...	...	...	...	...	...	9.6	1.30e-14	0.11	...
C IV	1548.1871	5.1	...	...	...	5.7	1.94e-15	0.03	26.9	1.14e-14	0.13	...	...	...	11.3	8.31e-14	0.06	...
C IV	1550.7723	5.1	...	...	...	5.6	8.93e-16	-0.01	23.0	6.21e-15	0.17	...	...	...	12.3	4.24e-14	0.07	...
Al II	1670.7870	4.6	...	...	...	6.6	1.28e-15	-0.05	17.0	7.69e-15	0.00	...	...	...	8.8	3.84e-14	-0.01	...

**Notes.** <sup>(a)</sup> Line fluxes (in  $\text{erg cm}^{-2} \text{s}^{-1}$ ) measured in the spectra.  $\log T_{\text{max}}$  indicates the maximum temperature of formation of the line (unweighted by the EMD). “Ratio” is the  $\log(F_{\text{obs}}/F_{\text{pred}})$  of the line. “Blends”, in at least one of the stars, amounting to more than 5% of the total flux for each line are indicated, with wavelengths in Å.

**Table D.9.** HST/COS and STIS line fluxes of GJ 436, HD 209458, GJ 3470, TRAPPIST-1, and GJ 486<sup>a</sup>.

Ion	$\lambda_{\text{model}}$ (Å)	$\log T_{\text{max}}$ (K)	GJ 436			HD 209458			GJ 3470			TRAPPIST-1			GJ 486			Blends
			S/N	$F_{\text{obs}}$	Ratio	S/N	$F_{\text{obs}}$	Ratio	S/N	$F_{\text{obs}}$	Ratio	S/N	$F_{\text{obs}}$	Ratio	S/N	$F_{\text{obs}}$	Ratio	
C III	1176.0000	4.8	...	...	...	...	...	...	20.0	5.41e-16	0.12	4.3	2.41e-17	-0.17	1.0	2.58e-16	-0.30	
Si III	1206.5019	4.9	5.9	4.58e-16	-0.60	36.8	1.29e-15	-0.89	23.5	3.40e-16	-0.57	5.1	2.04e-17	-0.02	3.5	9.49e-16	-0.13	Si III 1206.5570
O V	1218.3440	5.5	...	...	...	26.5	3.97e-16	0.01	23.1	1.16e-16	0.00	...	...	...	...	...	...	
N V	1238.8218	5.4	11.4	5.46e-16	-0.01	...	...	...	16.9	4.02e-16	0.04	4.1	3.80e-17	0.05	2.2	1.76e-16	0.08	
N V	1242.8042	5.4	8.2	2.86e-16	0.01	6.5	2.60e-17	0.02	21.2	1.71e-16	-0.03	4.5	1.62e-17	-0.02	2.9	6.09e-17	-0.07	
S II	1259.5210	4.6	...	...	...	3.1	1.68e-16	0.01	...	...	...	...	...	...	...	...	...	
Si II	1264.7400	4.5	12.5	7.57e-17	0.33	...	...	...	13.7	4.15e-17	0.19	...	...	...	...	...	...	
Si II	1265.0040	4.6	4.6	3.02e-17	0.11	...	...	...	14.0	1.83e-17	0.01	...	...	...	...	...	...	
Si II	1309.2770	4.6	...	...	...	...	...	...	14.1	1.68e-17	-0.06	...	...	...	...	...	...	
C II	1334.5350	4.7	7.9	2.98e-16	-0.45	32.2	8.04e-16	-0.21	25.1	2.21e-16	-0.30	5.7	2.79e-17	-0.19	...	...	...	
C II	1335.7100	4.7	9.1	8.59e-16	0.20	114.7	1.61e-15	0.29	33.3	5.61e-16	0.29	4.7	4.62e-17	0.22	2.3	4.35e-16	0.06	C II 1335.6650
Si IV	1393.7552	5.0	7.4	3.22e-16	0.09	23.7	9.47e-16	0.01	24.1	2.43e-16	0.03	...	...	...	1.6	1.42e-16	-0.02	
Si IV	1402.7704	5.0	7.1	1.80e-16	0.14	10.4	5.11e-16	0.04	23.6	1.10e-16	-0.01	...	...	...	1.3	7.79e-17	0.02	
Si II	1526.7090	4.5	...	...	...	16.5	1.19e-16	0.02	...	...	...	...	...	...	1.2	5.03e-17	0.44	
Si II	1533.4320	4.5	3.6	6.44e-17	-0.02	16.5	2.31e-16	0.01	...	...	...	...	...	...	...	...	...	
C IV	1548.1871	5.1	9.3	1.40e-15	-0.01	27.7	1.05e-15	-0.06	...	...	...	3.9	1.15e-16	-0.02	2.8	8.90e-16	0.05	
C IV	1550.7723	5.1	6.4	7.51e-16	0.02	7.4	7.07e-16	0.07	...	...	...	3.1	6.88e-17	0.06	1.8	3.62e-16	-0.04	
Al II	1670.7870	4.6	6.3	3.07e-16	0.00	...	...	...	...	...	...	...	...	...	1.1	3.29e-16	0.01	

**Notes.** <sup>(a)</sup> Line fluxes (in erg cm<sup>-2</sup> s<sup>-1</sup>) measured in the spectra.  $\log T_{\text{max}}$  (K) indicates the maximum temperature of formation of the line (unweighted by the EMD). “Ratio” is the  $\log(F_{\text{obs}}/F_{\text{pred}})$  of the line. “Blends”, in at least one of the stars, amounting to more than 5% of the total flux for each line are indicated, with wavelengths in Å.

**Table D.10.** HST/COS and STIS line fluxes of HD 149026, WASP-52, HD 63433, GJ 357, and TOI-836<sup>a</sup>.

Ion	$\lambda_{\text{model}}$ (Å)	$\log T_{\text{max}}$ (K)	HD 149026			WASP 52			HD 63433			GJ 357			TOI-836			Blends
			S/N	$F_{\text{obs}}$	Ratio	S/N	$F_{\text{obs}}$	Ratio	S/N	$F_{\text{obs}}$	Ratio	S/N	$F_{\text{obs}}$	Ratio	S/N	$F_{\text{obs}}$	Ratio	
C III	1176.0000	4.8	1.4	2.24e-16	-0.32	...	...	...	...	...	...	...	...	2.3	1.24e-15	-0.56		
Si II	1197.3950	4.6	...	...	...	...	...	...	17.7	4.33e-16	0.00	...	...	...	...	...		
S V	1199.1360	5.3	...	...	...	...	...	...	33.5	4.46e-16	0.05	...	...	...	...	...		
Si III	1200.9610	4.9	...	...	...	5.9	2.60e-16	0.03	13.8	3.29e-16	-0.09	...	...	...	...	...		
Si III	1206.5019	4.9	1.5	4.46e-16	-0.93	10.5	1.88e-15	0.04	68.8	3.84e-14	0.04	...	...	...	...	...		
O V	1218.3440	5.5	...	...	...	2.6	3.36e-16	0.03	94.5	9.20e-15	0.03	...	...	...	...	...		
N V	1238.8218	5.4	2.0	8.46e-17	0.04	3.4	3.08e-16	0.00	36.3	4.06e-15	0.01	4.1	1.32e-16	0.06	3.2	1.33e-15	0.04	
Fe XII	1242.0050	6.3	...	...	...	1.0	2.08e-17	0.00	24.8	4.62e-16	0.01	...	...	...	...	...		
N V	1242.8042	5.4	1.7	3.55e-17	-0.04	1.5	4.18e-17	-0.56	29.7	2.14e-15	0.03	4.0	5.42e-17	-0.02	3.0	3.29e-16	-0.26	
Si II	1264.7400	4.5	...	...	...	...	...	...	...	...	...	...	...	2.7	2.03e-16	-0.38	Si II 1265.0040	
C II	1334.5350	4.7	...	...	...	...	...	...	...	...	...	4.7	1.13e-16	-0.50	...	...		
C II	1335.7100	4.7	7.3	1.07e-15	0.30	...	...	...	...	...	...	4.9	2.94e-16	0.11	7.1	3.38e-15	0.01	C II 1335.6650
Si IV	1393.7552	5.0	4.7	3.89e-16	0.06	2.7	5.80e-17	-0.07	...	...	...	...	...	3.8	7.19e-16	-0.08		
O IV	1401.1570	5.3	1.4	2.69e-17	-0.30	...	...	...	...	...	...	...	...	...	...	...		
Si IV	1402.7704	5.0	...	...	...	2.0	3.27e-17	-0.02	...	...	...	1.8	5.11e-17	0.02	...	...		
O IV	1404.8060	5.3	2.4	1.37e-16	0.26	...	...	...	...	...	...	...	...	...	...	...		
S IV	1406.0160	5.1	2.5	2.14e-16	0.06	...	...	...	...	...	...	...	...	...	...	...	O IV 1407.3820	
Si II	1533.4320	4.5	...	...	...	...	...	...	...	...	...	...	...	1.7	3.88e-16	-0.11		
C IV	1548.1871	5.1	9.3	1.33e-15	0.01	...	...	...	...	...	...	2.8	5.55e-16	-0.01	4.9	3.18e-15	-0.03	C IV 1550.7723
C IV	1550.7723	5.1	...	...	...	...	...	...	...	...	...	2.3	1.82e-16	-0.19	4.6	1.82e-15	0.03	
Al II	1670.7870	4.6	...	...	...	...	...	...	...	...	...	3.2	1.95e-16	-0.01	2.2	8.05e-16	-0.03	

**Notes.** <sup>(a)</sup> Line fluxes (in erg cm<sup>-2</sup> s<sup>-1</sup>) measured in the spectra.  $\log T_{\text{max}}$  (K) indicates the maximum temperature of formation of the line (unweighted by the EMD). “Ratio” is the  $\log(F_{\text{obs}}/F_{\text{pred}})$  of the line. “Blends”, in at least one of the stars, amounting to more than 5% of the total flux for each line are indicated, with wavelengths in Å.

**Table D.11.** HST/COS and STIS line fluxes of GJ 1214, WASP-77A, HD 73583, WASP-13 and GJ 9827<sup>a</sup>.

Ion	$\lambda_{\text{model}}$ (Å)	$\log T_{\text{max}}$ (K)	GJ 1214			WASP-77A			HD 73583			WASP-13			GJ 9827			Blends
			S/N	$F_{\text{obs}}$	Ratio	S/N	$F_{\text{obs}}$	Ratio	S/N	$F_{\text{obs}}$	Ratio	S/N	$F_{\text{obs}}$	Ratio	S/N	$F_{\text{obs}}$	Ratio	
C III	1176.0000	4.8	3.7	5.10e-17	-0.16	2.8	6.19e-16	-0.07	...	...	...	...	...	...	...	...		
Si III	1206.5019	4.9	3.4	5.39e-17	-0.43	...	...	...	14.6	1.52e-15	-0.01	...	...	...	4.8	1.44e-16	-0.02	
O V	1218.3440	5.5	3.6	3.77e-17	0.04	...	...	...	10.8	5.80e-16	-0.00	...	...	...	...	...		
N V	1238.8218	5.4	3.7	9.79e-17	-0.02	...	...	...	11.8	5.36e-16	0.02	...	...	...	...	...		
N V	1242.8042	5.4	3.5	5.29e-17	0.02	...	...	...	8.3	2.38e-16	-0.03	...	...	...	...	...		
C II	1334.5350	4.7	3.5	3.77e-17	-0.26	...	...	...	...	...	...	...	...	...	...	...		
C II	1335.7100	4.7	3.3	8.45e-17	0.29	3.2	7.45e-16	0.02	...	...	...	4.7	8.36e-17	0.00	...	...	C II 1334.5350, 1335.6650	
Si IV	1393.7552	5.0	4.3	3.27e-17	0.10	4.3	5.80e-16	0.18	...	...	...	...	...	...	...	...		
O IV	1399.7800	5.3	...	...	...	1.7	7.85e-17	0.05	...	...	...	...	...	...	...	...		
Si IV	1402.7704	5.0	...	...	...	4.6	1.99e-16	-0.22	...	...	...	...	...	...	...	...	O IV 1401.1570	
O IV	1404.8060	5.3	...	...	...	3.4	1.90e-16	0.00	...	...	...	...	...	...	...	...		
C IV	1548.1871	5.1	3.2	2.90e-16	0.02	4.0	1.41e-15	0.03	...	...	...	4.2	1.11e-16	0.04	...	...	C IV 1550.7723	
C IV	1550.7723	5.1	...	...	...	...	...	...	...	...	...	4.5	4.61e-17	-0.04	...	...		

**Notes.** <sup>(a)</sup> Line fluxes (in erg cm<sup>-2</sup> s<sup>-1</sup>) measured in the spectra.  $\log T_{\text{max}}$  (K) indicates the maximum temperature of formation of the line (unweighted by the EMD). “Ratio” is the  $\log(F_{\text{obs}}/F_{\text{pred}})$  of the line. “Blends”, in at least one of the stars, amounting to more than 5% of the total flux for each line are indicated, with wavelengths in Å.



**Table D.12.** EMDs of stars with UV and X-ray high-resolution spectra<sup>a</sup>.

log $T$ (K)	Proxima Cen	AU Mic	AD Leo	Lalande 21185	$\tau$ Boo	GJ 674	WASP 52 <sup>b</sup>	55 Cnc <sup>b</sup>	Barnard's star <sup>b</sup>	HD 63433 <sup>b</sup>
4.0	48.55 <sup>+0.30</sup> <sub>-0.20</sub>	50.70:	50.50:	47.70:	50.70:	49.75:	51.30:	49.80:	47.20:	51.10:
4.1	48.30 <sup>+0.30</sup> <sub>-0.30</sub>	50.50 <sup>+0.30</sup> <sub>-0.30</sub>	50.30 <sup>+0.50</sup> <sub>-0.20</sub>	47.60 <sup>+0.30</sup> <sub>-0.30</sub>	50.60:	49.60 <sup>+0.30</sup> <sub>-0.20</sub>	51.10 <sup>+0.20</sup> <sub>-0.40</sub>	49.65 <sup>+0.20</sup> <sub>-0.30</sub>	47.10 <sup>+0.20</sup> <sub>-0.30</sub>	50.90 <sup>+0.30</sup> <sub>-0.20</sub>
4.2	48.05 <sup>+0.20</sup> <sub>-0.30</sub>	50.40 <sup>+0.30</sup> <sub>-0.40</sub>	50.10 <sup>+0.60</sup> <sub>-0.00</sub>	47.50 <sup>+0.30</sup> <sub>-0.30</sub>	50.50:	49.35 <sup>+0.40</sup> <sub>-0.10</sub>	50.90 <sup>+0.40</sup> <sub>-0.20</sub>	49.45 <sup>+0.20</sup> <sub>-0.30</sub>	47.00 <sup>+0.10</sup> <sub>-0.30</sub>	50.70 <sup>+0.20</sup> <sub>-0.20</sub>
4.3	47.90 <sup>+0.20</sup> <sub>-0.40</sub>	50.20 <sup>+0.20</sup> <sub>-0.40</sub>	49.80 <sup>+0.40</sup> <sub>-0.20</sub>	47.40 <sup>+0.20</sup> <sub>-0.30</sub>	50.40:	49.10 <sup>+0.20</sup> <sub>-0.20</sub>	50.80 <sup>+0.40</sup> <sub>-0.30</sub>	49.10 <sup>+0.20</sup> <sub>-0.20</sub>	46.80 <sup>+0.10</sup> <sub>-0.30</sub>	50.50 <sup>+0.10</sup> <sub>-0.30</sub>
4.4	47.80 <sup>+0.30</sup> <sub>-0.30</sub>	50.05 <sup>+0.30</sup> <sub>-0.30</sub>	49.45 <sup>+0.00</sup> <sub>-0.40</sub>	47.30 <sup>+0.10</sup> <sub>-0.30</sub>	50.30:	48.95 <sup>+0.10</sup> <sub>-0.30</sub>	50.70 <sup>+0.30</sup> <sub>-0.20</sub>	48.85 <sup>+0.15</sup> <sub>-0.15</sub>	46.60 <sup>+0.10</sup> <sub>-0.40</sub>	50.25 <sup>+0.10</sup> <sub>-0.30</sub>
4.5	47.75 <sup>+0.40</sup> <sub>-0.20</sub>	49.80 <sup>+0.40</sup> <sub>-0.20</sub>	49.00 <sup>+0.10</sup> <sub>-0.40</sub>	47.10 <sup>+0.10</sup> <sub>-0.30</sub>	50.20 <sup>+0.30</sup> <sub>-0.20</sub>	48.75 <sup>+0.15</sup> <sub>-0.15</sub>	50.50 <sup>+0.10</sup> <sub>-0.30</sub>	48.80 <sup>+0.20</sup> <sub>-0.20</sub>	46.60 <sup>+0.10</sup> <sub>-0.30</sub>	50.00 <sup>+0.10</sup> <sub>-0.40</sub>
4.6	47.75 <sup>+0.30</sup> <sub>-0.30</sub>	49.50 <sup>+0.30</sup> <sub>-0.40</sub>	48.75 <sup>+0.20</sup> <sub>-0.40</sub>	46.90 <sup>+0.05</sup> <sub>-0.25</sub>	50.10 <sup>+0.20</sup> <sub>-0.30</sub>	48.70 <sup>+0.10</sup> <sub>-0.30</sub>	50.30 <sup>+0.10</sup> <sub>-0.30</sub>	48.80 <sup>+0.30</sup> <sub>-0.30</sub>	46.65 <sup>+0.10</sup> <sub>-0.30</sub>	49.70 <sup>+0.05</sup> <sub>-0.35</sub>
4.7	47.80 <sup>+0.20</sup> <sub>-0.40</sub>	49.40 <sup>+0.30</sup> <sub>-0.30</sub>	48.60 <sup>+0.00</sup> <sub>-0.40</sub>	46.95 <sup>+0.10</sup> <sub>-0.30</sub>	50.00 <sup>+0.10</sup> <sub>-0.30</sub>	48.60 <sup>+0.00</sup> <sub>-0.30</sub>	50.05 <sup>+0.10</sup> <sub>-0.30</sub>	48.70 <sup>+0.20</sup> <sub>-0.20</sub>	46.80 <sup>+0.20</sup> <sub>-0.20</sub>	49.50 <sup>+0.05</sup> <sub>-0.35</sub>
4.8	47.75 <sup>+0.30</sup> <sub>-0.30</sub>	49.35 <sup>+0.20</sup> <sub>-0.40</sub>	48.70 <sup>+0.00</sup> <sub>-0.40</sub>	46.95 <sup>+0.10</sup> <sub>-0.30</sub>	49.95 <sup>+0.05</sup> <sub>-0.45</sub>	48.75 <sup>+0.00</sup> <sub>-0.40</sub>	49.60 <sup>+0.10</sup> <sub>-0.40</sub>	48.60 <sup>+0.20</sup> <sub>-0.20</sub>	46.90 <sup>+0.20</sup> <sub>-0.40</sub>	49.40 <sup>+0.05</sup> <sub>-0.35</sub>
4.9	47.55 <sup>+0.30</sup> <sub>-0.40</sub>	49.40 <sup>+0.20</sup> <sub>-0.40</sub>	49.30 <sup>+0.10</sup> <sub>-0.00</sub>	46.80 <sup>+0.10</sup> <sub>-0.20</sub>	49.85 <sup>+0.20</sup> <sub>-0.30</sub>	48.95 <sup>+0.40</sup> <sub>-0.00</sub>	49.20 <sup>+0.20</sup> <sub>-0.40</sub>	48.05 <sup>+0.15</sup> <sub>-0.15</sub>	46.40 <sup>+0.00</sup> <sub>-0.40</sub>	49.30 <sup>+0.20</sup> <sub>-0.30</sub>
5.0	47.35 <sup>+0.40</sup> <sub>-0.30</sub>	49.55 <sup>+0.45</sup> <sub>-0.35</sub>	49.35 <sup>+0.10</sup> <sub>-0.10</sub>	46.70 <sup>+0.10</sup> <sub>-0.30</sub>	49.80 <sup>+0.20</sup> <sub>-0.30</sub>	48.50 <sup>+0.20</sup> <sub>-0.20</sub>	49.00 <sup>+0.30</sup> <sub>-0.20</sub>	47.70 <sup>+0.10</sup> <sub>-0.30</sub>	46.50 <sup>+0.20</sup> <sub>-0.10</sub>	49.35 <sup>+0.20</sup> <sub>-0.20</sub>
5.1	47.15 <sup>+0.35</sup> <sub>-0.45</sub>	49.55 <sup>+0.30</sup> <sub>-0.40</sub>	49.00 <sup>+0.20</sup> <sub>-0.20</sub>	46.60 <sup>+0.10</sup> <sub>-0.30</sub>	49.85 <sup>+0.10</sup> <sub>-0.30</sub>	48.35 <sup>+0.15</sup> <sub>-0.25</sub>	48.90 <sup>+0.40</sup> <sub>-0.20</sub>	47.60 <sup>+0.10</sup> <sub>-0.30</sub>	46.55 <sup>+0.00</sup> <sub>-0.40</sub>	49.45 <sup>+0.30</sup> <sub>-0.30</sub>
5.2	46.95 <sup>+0.40</sup> <sub>-0.20</sub>	49.40 <sup>+0.30</sup> <sub>-0.30</sub>	48.65 <sup>+0.10</sup> <sub>-0.40</sub>	46.65 <sup>+0.30</sup> <sub>-0.20</sub>	49.80 <sup>+0.15</sup> <sub>-0.15</sub>	48.30 <sup>+0.15</sup> <sub>-0.15</sub>	48.90 <sup>+0.00</sup> <sub>-0.40</sub>	47.80 <sup>+0.10</sup> <sub>-0.40</sub>	46.30 <sup>+0.00</sup> <sub>-0.40</sub>	49.50 <sup>+0.20</sup> <sub>-0.30</sub>
5.3	46.80 <sup>+0.25</sup> <sub>-0.45</sub>	49.20 <sup>+0.20</sup> <sub>-0.40</sub>	48.50 <sup>+0.10</sup> <sub>-0.20</sub>	46.70 <sup>+0.10</sup> <sub>-0.30</sub>	49.55 <sup>+0.10</sup> <sub>-0.20</sub>	48.10 <sup>+0.15</sup> <sub>-0.25</sub>	49.10 <sup>+0.00</sup> <sub>-0.40</sub>	48.30 <sup>+0.10</sup> <sub>-0.10</sub>	46.25 <sup>+0.10</sup> <sub>-0.30</sub>	49.35 <sup>+0.05</sup> <sub>-0.25</sub>
5.4	46.70 <sup>+0.40</sup> <sub>-0.30</sub>	49.10 <sup>+0.20</sup> <sub>-0.40</sub>	48.35 <sup>+0.00</sup> <sub>-0.40</sub>	46.50 <sup>+0.20</sup> <sub>-0.30</sub>	49.10 <sup>+0.05</sup> <sub>-0.35</sub>	47.70 <sup>+0.20</sup> <sub>-0.20</sub>	49.00 <sup>+0.20</sup> <sub>-0.40</sub>	48.60 <sup>+0.20</sup> <sub>-0.10</sub>	46.20 <sup>+0.25</sup> <sub>-0.15</sub>	49.25 <sup>+0.05</sup> <sub>-0.35</sub>
5.5	46.60 <sup>+0.30</sup> <sub>-0.40</sub>	48.90 <sup>+0.20</sup> <sub>-0.40</sub>	48.25 <sup>+0.50</sup> <sub>-0.10</sub>	46.35 <sup>+0.30</sup> <sub>-0.20</sub>	49.00 <sup>+0.20</sup> <sub>-0.30</sub>	47.65 <sup>+0.15</sup> <sub>-0.25</sub>	48.85 <sup>+0.20</sup> <sub>-0.40</sub>	48.40 <sup>+0.30</sup> <sub>-0.30</sub>	46.15 <sup>+0.35</sup> <sub>-0.25</sub>	49.15 <sup>+0.25</sup> <sub>-0.25</sub>
5.6	46.55 <sup>+0.40</sup> <sub>-0.20</sub>	48.70 <sup>+0.30</sup> <sub>-0.40</sub>	48.20 <sup>+0.40</sup> <sub>-0.20</sub>	46.40 <sup>+0.30</sup> <sub>-0.30</sub>	48.90 <sup>+0.20</sup> <sub>-0.40</sub>	47.75 <sup>+0.25</sup> <sub>-0.25</sub>	48.90 <sup>+0.40</sup> <sub>-0.40</sub>	47.95 <sup>+0.20</sup> <sub>-0.20</sub>	46.10 <sup>+0.30</sup> <sub>-0.30</sub>	48.90 <sup>+0.30</sup> <sub>-0.30</sub>
5.7	46.55 <sup>+0.30</sup> <sub>-0.30</sub>	48.80 <sup>+0.40</sup> <sub>-0.10</sub>	48.25 <sup>+0.20</sup> <sub>-0.30</sub>	46.50 <sup>+0.40</sup> <sub>-0.20</sub>	48.90 <sup>+0.20</sup> <sub>-0.30</sub>	47.90 <sup>+0.20</sup> <sub>-0.30</sub>	49.20 <sup>+0.40</sup> <sub>-0.20</sub>	48.00 <sup>+0.20</sup> <sub>-0.30</sub>	46.20 <sup>+0.30</sup> <sub>-0.20</sub>	48.80 <sup>+0.20</sup> <sub>-0.30</sub>
5.8	46.75 <sup>+0.20</sup> <sub>-0.20</sub>	49.10 <sup>+0.25</sup> <sub>-0.15</sub>	48.30 <sup>+0.20</sup> <sub>-0.20</sub>	46.70 <sup>+0.30</sup> <sub>-0.20</sub>	49.00 <sup>+0.30</sup> <sub>-0.30</sub>	48.00 <sup>+0.20</sup> <sub>-0.20</sub>	49.50:	48.20:	46.40 <sup>+0.30</sup> <sub>-0.20</sub>	48.95:
5.9	47.15 <sup>+0.20</sup> <sub>-0.30</sub>	49.35 <sup>+0.20</sup> <sub>-0.20</sub>	48.40 <sup>+0.20</sup> <sub>-0.30</sub>	47.00 <sup>+0.30</sup> <sub>-0.20</sub>	49.10 <sup>+0.30</sup> <sub>-0.30</sub>	48.20 <sup>+0.30</sup> <sub>-0.20</sub>	49.90:	48.50:	46.60 <sup>+0.30</sup> <sub>-0.20</sub>	49.20:
6.0	47.70 <sup>+0.40</sup> <sub>-0.20</sub>	49.70 <sup>+0.25</sup> <sub>-0.25</sub>	48.60 <sup>+0.10</sup> <sub>-0.40</sub>	47.30 <sup>+0.30</sup> <sub>-0.20</sub>	49.30 <sup>+0.30</sup> <sub>-0.30</sub>	48.70 <sup>+0.30</sup> <sub>-0.20</sub>	50.20:	48.90:	46.90 <sup>+0.30</sup> <sub>-0.30</sub>	49.55:
6.1	48.25 <sup>+0.30</sup> <sub>-0.20</sub>	50.10 <sup>+0.20</sup> <sub>-0.20</sub>	49.00 <sup>+0.10</sup> <sub>-0.40</sub>	47.70 <sup>+0.40</sup> <sub>-0.20</sub>	49.55 <sup>+0.25</sup> <sub>-0.25</sub>	49.50 <sup>+0.40</sup> <sub>-0.00</sub>	50.70:	49.50:	47.30 <sup>+0.30</sup> <sub>-0.20</sub>	49.90:
6.2	48.75 <sup>+0.20</sup> <sub>-0.10</sub>	50.40 <sup>+0.35</sup> <sub>-0.15</sub>	50.05 <sup>+0.20</sup> <sub>-0.10</sub>	48.00 <sup>+0.40</sup> <sub>-0.00</sub>	50.05 <sup>+0.15</sup> <sub>-0.35</sub>	49.40 <sup>+0.00</sup> <sub>-0.30</sub>	50.90:	49.80:	47.70 <sup>+0.00</sup> <sub>-0.40</sub>	50.65:
6.3	48.50 <sup>+0.20</sup> <sub>-0.20</sub>	50.70 <sup>+0.30</sup> <sub>-0.20</sub>	50.35 <sup>+0.10</sup> <sub>-0.10</sub>	48.15 <sup>+0.20</sup> <sub>-0.20</sub>	50.35 <sup>+0.00</sup> <sub>-0.40</sub>	48.80 <sup>+0.10</sup> <sub>-0.40</sub>	50.70:	49.60:	47.80 <sup>+0.20</sup> <sub>-0.30</sub>	50.85:
6.4	48.30 <sup>+0.20</sup> <sub>-0.30</sub>	50.40 <sup>+0.30</sup> <sub>-0.20</sub>	49.65 <sup>+0.20</sup> <sub>-0.20</sub>	47.90 <sup>+0.40</sup> <sub>-0.20</sub>	50.00 <sup>+0.20</sup> <sub>-0.30</sub>	48.65 <sup>+0.10</sup> <sub>-0.30</sub>	50.60:	49.30:	47.20 <sup>+0.20</sup> <sub>-0.20</sub>	50.60:
6.5	48.40 <sup>+0.20</sup> <sub>-0.30</sub>	50.75 <sup>+0.35</sup> <sub>-0.15</sub>	49.95 <sup>+0.40</sup> <sub>-0.20</sub>	48.20 <sup>+0.20</sup> <sub>-0.30</sub>	50.30 <sup>+0.40</sup> <sub>-0.20</sub>	48.60 <sup>+0.20</sup> <sub>-0.30</sub>	50.50:	49.40:	47.10 <sup>+0.20</sup> <sub>-0.20</sub>	50.80:
6.6	48.75 <sup>+0.20</sup> <sub>-0.30</sub>	51.00 <sup>+0.45</sup> <sub>-0.05</sub>	50.20 <sup>+0.40</sup> <sub>-0.10</sub>	48.40 <sup>+0.15</sup> <sub>-0.35</sub>	51.15 <sup>+0.15</sup> <sub>-0.15</sub>	48.70 <sup>+0.20</sup> <sub>-0.20</sub>	50.40:	49.50:	47.20 <sup>+0.30</sup> <sub>-0.30</sub>	51.31:
6.7	49.20 <sup>+0.30</sup> <sub>-0.10</sub>	51.30 <sup>+0.10</sup> <sub>-0.40</sub>	50.40 <sup>+0.35</sup> <sub>-0.15</sub>	48.50 <sup>+0.00</sup> <sub>-0.30</sub>	51.30 <sup>+0.05</sup> <sub>-0.15</sub>	48.90 <sup>+0.20</sup> <sub>-0.30</sub>	50.20:	49.70:	47.30 <sup>+0.20</sup> <sub>-0.20</sub>	40.20:
6.8	49.40 <sup>+0.20</sup> <sub>-0.10</sub>	51.50 <sup>+0.05</sup> <sub>-0.25</sub>	50.60 <sup>+0.10</sup> <sub>-0.20</sub>	48.60 <sup>+0.00</sup> <sub>-0.30</sub>	50.40 <sup>+0.30</sup> <sub>-0.20</sub>	49.10 <sup>+0.00</sup> <sub>-0.40</sub>	49.70:	49.80:	47.50 <sup>+0.20</sup> <sub>-0.20</sub>	40.20:
6.9	49.10 <sup>+0.20</sup> <sub>-0.30</sub>	51.80 <sup>+0.10</sup> <sub>-0.10</sub>	50.85 <sup>+0.05</sup> <sub>-0.25</sub>	48.50 <sup>+0.20</sup> <sub>-0.30</sub>	49.80 <sup>+0.30</sup> <sub>-0.30</sub>	49.50 <sup>+0.00</sup> <sub>-0.30</sub>	49.20:	49.90:	47.95 <sup>+0.30</sup> <sub>-0.30</sub>	51.23:
7.0	49.05 <sup>+0.30</sup> <sub>-0.20</sub>	51.60 <sup>+0.25</sup> <sub>-0.25</sub>	50.80 <sup>+0.10</sup> <sub>-0.20</sub>	48.70 <sup>+0.20</sup> <sub>-0.20</sub>	49.50 <sup>+0.30</sup> <sub>-0.20</sub>	50.00 <sup>+0.10</sup> <sub>-0.10</sub>	48.50:	49.80:	48.15 <sup>+0.00</sup> <sub>-0.20</sub>	40.20:
7.1	49.25 <sup>+0.30</sup> <sub>-0.05</sub>	51.80 <sup>+0.25</sup> <sub>-0.05</sub>	50.55 <sup>+0.15</sup> <sub>-0.25</sub>	48.80 <sup>+0.10</sup> <sub>-0.40</sub>	49.30 <sup>+0.30</sup> <sub>-0.30</sub>	49.80 <sup>+0.20</sup> <sub>-0.10</sub>	44.00:	49.50:	47.70 <sup>+0.20</sup> <sub>-0.30</sub>	40.20:
7.2	48.85 <sup>+0.20</sup> <sub>-0.20</sub>	51.20 <sup>+0.30</sup> <sub>-0.10</sub>	50.40 <sup>+0.10</sup> <sub>-0.30</sub>	48.50 <sup>+0.20</sup> <sub>-0.30</sub>	49.00 <sup>+0.20</sup> <sub>-0.30</sub>	49.30 <sup>+0.20</sup> <sub>-0.20</sub>	44.00:	49.00:	47.10 <sup>+0.20</sup> <sub>-0.30</sub>	40.20:
7.3	48.45 <sup>+0.30</sup> <sub>-0.20</sub>	50.70 <sup>+0.30</sup> <sub>-0.10</sub>	50.20 <sup>+0.30</sup> <sub>-0.20</sub>	48.10:	48.70:	48.80 <sup>+0.30</sup> <sub>-0.20</sub>	44.00:	48.00:	46.50 <sup>+0.30</sup> <sub>-0.30</sub>	40.20:
7.4	47.95:	50.20 <sup>+0.30</sup> <sub>-0.20</sub>	49.80 <sup>+0.30</sup> <sub>-0.20</sub>	47.30:	48.30:	48.10 <sup>+0.30</sup> <sub>-0.30</sub>	44.00:	47.40:	46.00 <sup>+0.20</sup> <sub>-0.30</sub>	40.20:
7.5	46.95:	49.80:	49.50:	46.80:	48.00:	47.60:	44.00:	46.00:	45.50:	40.20:

**Notes.** <sup>(a)</sup> Emission measure (EM= $\log \int N_e N_H dV$ ), where  $N_e$  and  $N_H$  are electron and hydrogen densities, in  $\text{cm}^{-3}$ . Errors provided are not independent between the different temperatures, as explained in Sanz-Forcada et al. (2003b). <sup>(b)</sup> The EM above  $\log T$  (K)=5.9 of these stars are listed to show consistency of UV coronal line (i.e. lines formed above that temperature) fluxes. The model used for the SED above that temperature is based on the X-ray low resolution spectra in these cases.

